DEPARTAMENTO DE INGENIERÍA DE SISTEMAS Y AUTOMÁTICA
ESCUELA SUPERIOR DE INGENIERÍA
UNIVERSIDAD DE SEVILLA

MODELLING AND CONTROL OF AERIAL MANIPULATORS CONSIDERING AERODYNAMIC EFFECTS

por

Pedro Jesús Sánchez Cuevas

Graduado en Ingeniería Aeroespacial / Master en Ingeniería Aeronáutica

PROPUESTA DE TESIS DOCTORAL
PARA LA OBTENCIÓN DEL TÍTULO DE

DOCTOR POR LA UNIVERSIDAD DE SEVILLA

SEVILLA, 2020

Directores

Dr.Ing. Guillermo Heredia Benot, Catedrático

Dr.Ing. Aníbal Ollero Baturone, Catedrático

UNIVERSIDAD DE SEVILLA

Memoria para optar al grado de Doctor por la Universidad de Sevilla

Autor: **Pedro Jesús Sánchez Cuevas**

Título: **MODELLING AND CONTROL OF AERIAL MANIPULATORS CONSIDERING AERODYNAMIC EFFECTS**

Departamento: **Departamento de Ingeniería de Sistemas y Automática**

V° B° Director:

Guillermo Heredia Benot

V° B° Director:

Aníbal Ollero Baturone

El autor:

Pedro Jesús Sánchez Cuevas

A mi familia,
A mis profesores,
A ella.

Agradecimientos

Agradezco al grupo de robótica, visión y control de la Universidad de Sevilla la confianza depositada en mi persona para la realización de esta tesis.

Me gustaría hacer especialmente responsable y agradecer esta oportunidad a Aníbal Ollero. Él fue el principio de la aventura. También quiero citar la ayuda y profesionalidad de Guillermo Heredia Benot, que ha sido la solución en los momentos más complicados, siempre manteniendo la calma y acertando en sus decisiones y consejos. Agradezco a mis directores, su confianza, su responsabilidad y las oportunidades que me han dado para crecer y dar los primeros pasos en este apasionante mundo de investigadores.

Me dirijo también a mis compañeros del laboratorio, nada hubiera sido posible sin la atención y ayuda que diariamente me han dedicado. Siempre me han prestado el consejo de la experiencia y gran parte de su talento resolutivo. Gracias especialmente a Víctor, Antonio, Fran, Arturo, Manu, Alejandro y Rafa. Lo que me habeis hecho vivir, es algo que siempre irá conmigo.

Por último, agradecer el apoyo de mi familia, que desde la distancia estaban cerca en los momentos mas duros de este camino, que me lo dieron todo sin preguntar y, por supuesto, sin esperar nada a cambio.

Gracias a Rebeca, mi compañera de viaje, mi apoyo en la batalla. Me has hecho crecer como persona y me has enseñado a confiar en mi mismo. Eres parte de esta victoria.

Muchas Gracias.

Pedro Jesús Sánchez Cuevas
Grupo de Robótica Visión y Control, Sevilla, 2020

Este trabajo ha sido financiado a través del programa de formación del profesorado universitario (FPU) y por el proyecto nacional ARTIC (RTI2018-102224-B-I00) financiados por el Ministerio de Economía, Industria y Competitiviad y por los proyectos europeos H2020 AERIAL-CORE (H2020-2019-871479), RESIST (H2020-MG-2017-769066) y HYFLIERS (H2020-ICT-25-2017-779411) financiados por la Comisión Europea.

This work has been supported by the FPU Program and by the national ARTIC (RTI2018-102224-B-I00) project funded by of the Spanish Ministerio de Educación, Cultura y Deporte and by the H2020 AERIAL-CORE (H2020-2019-871479), RESIST (H2020-MG-2017-769066) and HYFLIERS (H2020-ICT-25-2017-779411) projects funded by the European Commission.

Resumen

El interés de la comunidad investigadora en los vehículos aéreos no tripulados (UAV) ha crecido significativamente en la última década. De hecho, este tema se está volviendo especialmente atractivo desde el punto de vista empresarial debido a su variada gama de aplicaciones.

A pesar de que en las aplicaciones comerciales actuales, en las que los drones se utilizan para realizar tareas pasivas, como filmación, vigilancia, inspección visual, monitorización o teledetección, la comunidad científica está yendo más allá utilizando estos drones como robots aéreos que pueden interactuar físicamente con el entorno. En esa interacción, el robot aéreo está trabajando muy cerca de varios obstáculos u objetos, por lo que la caracterización aerodinámica de los fenómenos que surgen al volar cerca de esos obstáculos es muy importante para asegurar que la operacíon de manipulación aérea se pueda realizar de forma segura y eficaz. En esta tesis se aborda este problema específico, que surge cuando los robots aéreos que vuelan cerca de obstáculos, mediante el desarrollo de nuevos modelos e implementación de técnicas de control adaptadas para garantizar la seguridad y efectividad durante la operación en escenarios reales.

A lo largo de esta tesis, el autor propone el estudio de dichos efectos aerodinámicos a través de la generalización del método clásico basado en la aerodinámica potencial linealizada y estudios experimentales. También trata dos casos de uso diferentes en los que se ha tenido en cuenta el efecto aerodinámico desde el punto de vista del control. Por último, da un giro a la forma de modelar el efecto aerodinámico yendo más allá del método clásicos, estudiando cómo surgen diferentes efectos aerodinámicos cuando el robot se acerca a diferentes obstáculos desde un punto de vista bidimensional.

Abstract

The interest of the research community in Unmanned Aerial Vehicles (UAVs) has significantly grown in the last decade. Actually, this topic is becoming specially attractive for industrial companies due to its varied application range.

Beyond their current commercial applications, where drones are used to carry out passive tasks, such as filming, surveillance, visual inspection, monitoring or remote sensing, the research community is going further using these drones as aerial robots which can physically interact with the environment. In those interactions, the aerial robot works quite close to several obstacles or objects, and thus, the aerodynamic characterisation of the phenomena that arise when flying close to those obstacles becomes relevant to ensure that the aerial manipulation operation can be performed in a safe and effective way. This thesis takes part in this specific problem that arises in aerial manipulators flying close to obstacles, through the development of new models and adapted control techniques to ensure safety and effectiveness during operation in real scenarios.

Along this Thesis, the author proposes the study of the generalisation of the classical method based on linearised potential aerodynamics and also through experimental results. The Thesis also treats two different cases of use in which the aerodynamic effect has been taken into account from the control point of view. Last, it makes a twist to the modelled aerodynamic effect going beyond classical models, studying how different aerodynamic effects arise when the robot approaches different obstacles.

Contents

List of Figures

Chapter 1

Introduction

> Design is not how it looks like and feels like. Design is how it works
>
> Steve Jobs (Apple co-founder and former CEO)

The interest of the research community in Unmanned Aerial Vehicles (UAVs) [1] has significantly grown in the last decade. Actually, this topic is becoming specially attractive for industrial companies due to its varied application range.

There are a lot of companies,such as Amazon or DHL, which consider this technology as a clear business opportunity, and which, respectively propose [2] and [3] the use of drone with cargo capabilities as the future delivery system. They literally say that ""Unmanned aerial vehicles (UAVs) or drones can be used to deliver goods in the first and last mile as well for intralogistics and surveillance operations. "" Nowadays, most of the commercial applications are coming from the image and remotely data acquisition field, where UAVs are mainly presented as flying cameras that can be used for filming, surveillance, or photogrametric applications [4], [5] among others. In those ones, UAVs stand out for being significantly cheaper and safer than a manned helicopter.

On the one hand, in the field of visual monitoring and inspection, it is possible to find some specific samples in agricultural applications, where the WinterGreen

Research [6] estimates the current agricultural market at $494 million and expects it will increase in $3.69 billion by 2022.

On the other hand, these flying cameras are also taking place in visual inspection of big infrastructures, such as bridges, tunnels, power lines, cell towers [7] and even chemical plants or oil and gas industries [8]. In those ones, they can decrease the inspection cost by up to 10%.

Finally, UAVs are also present in applications that propose to use them as infrastructure, for example, to put a flying antenna to replace a cell tower which can be deployed in disaster scenes [9], and even it is possible to find solutions that use drones scanning and inventorying thousands of items in a warehouse [10].

It is clear that drones are here to stay. In fact, the investments in this technology are also joining the growing trend. The Goldmand Sachs agency, for instance, assimilated the change that drones are doing in the world like the one that produced technologies like the Internet and the GPS, which are, nowadays, present every day [11].

Despite the current commercial applications, drones are used to carry out passive tasks, such as filming, surveillance, visual inspection, monitoring or remote sensing, However,the research community is going further using these drones as aerial robots which can physically interact with the environment. This field is known in the research community as *Aerial Manipulation* [12], [13], and it is focused on involving UAVs in active tasks, like grasping objects, inspections by contact operations and human-robot interaction among others. This topic is producing a large -scale impact, placing UAVs in a varied amount of areas while transforming the industries in a disruptive way [14].

Aerial manipulation combines the use of UAVs with robotic arms, which are able to perform a wide variety of operations, such as work at a great height or dangerous ones for human environments, while they decrease the risks, cost and time of the operation. Some samples of these aerial manipulator have been proposed by the community, including single arm manipulators [15], [16], [17], [18], [19], [20], parallel manipulators [21], [22], linear actuators [23], [24], omnidirectional aerial platforms with manipulation capabilities [25], [26], [27], [28] and safer platforms to improve safety and extend the effective workspace of the manipulator, usually constrained by the

landing gear, using a long reach aerial manipulator in passive pendulum configuration [29], [27].

Thus, motivated by the aforementioned reasons (time consumption, operational cost and safer conditions for humans during the operation), the development of this new technology has been in the spotlight of the researcher community and it is a relevant topic for the European Robotic Strategic Research Agenda (eSRA)[30]. It is considered that aerial manipulators will be aerial robots that, in a near future, could be employed as robotic workers and co-workers in several applications. They will be specially helpful in those jobs that are considered dangerous for a human operator, whether to carry out these activities or, at least, to assist in hazardous and critical situations.

Some applications of this technology could be found in detection and repair of leaks in pipe structures in chemical plants, the insulation of cracks in the blades of wind turbines, the installation and retrieval of sensor devices in polluted areas, the inspection by contact of power lines or civilian infrastructures, like bridges or tunnels and the rescue of survivors in natural disasters. In fact, these aerial manipulators, also known as aerial robots, have demonstrated they are suitable and reliable for this kind of applications in the last years. For instance, the results of the last FP7 and H2020 European projects related to this topic, such as ARCAS [31], AEROARMS [32] and AEROBI [33] have shown several results that prove it even in real scenarios. Nowadays, the eSRA maintains the focus on developing this technology through the funding provided to the next generation of projects which approaches this technology, like HYFLIERS [34], RESIST [35], AERIAL-CORE [36] and PILOTING [37].

These projects aim to develop the next step in commercialisation and exploitation of aerial manipulation trying to close the gap between the research community and the end-users of this technology. In all of them, relevant end-users of this new technology are involved as important partners which establish and specify their requirements from the application point of view to guarantee that this project follows the value chain in the correct way. Some of these partners are big companies, like Total [38] which is the producer and supplier of oil, natural gas and low-carbon electricity in more than 130 countries and which has a workforce of more than 100,000 employees; Chevron [39],

which is one of the world's leading integrated energy companies producing safe, reliable energy now and for the future; EGNATIA ODOS [40], which is the company delegated by the Greek authority to design, construct, operate and maintain the 680km long Egnatia Motorway, a TEN-T core network stretching from Western Greece to the Greek / Turkish border; Ferrovial [41], which is one of the leading infrastructure and services operators; and ENEL [42] through E-Distribución which is Endesa's subsidiary in the electricity distribution business with 12.4 million clients in 27 Spanish provinces among others.

As it was aforementioned, the reasons that motivate the use of these robotic solutions in such applications lie in their capability and versatility to access workspaces at height faster and in a safer way than using traditional methods. This is intrinsically linked to their ability to fly, which, in turn, is due to aerodynamics. Thus, the aerodynamic characterisation of these aerial robots is very important to ensure that the aerial manipulation operation can be performed in a safe and effective way. In general, the aerodynamic problem can be divided in two different cases.

The first one is a generic case related to the propulsive system. This should be able to exert enough forces to lift off the robot and accomplish a controlled flight. This case has been deeply studied by the community for helicopters [43], [44], [45]. In this case,it is also necessary to study the interaction of the airflow with its own structure (arms, fairings, motor supports...), which does not change in most cases.

The second one is a specific problem that arises in aerial manipulators due to its use cases and morphology, which includes, firstly, flying close to obstacles and, secondly, the movement of several parts of the robot which can disturb the flow field around the propellers and change the behaviour of the rotors.

The thesis takes part in the problem that arises in the aerial manipulators flying close to obstacles. It will be reached through developing new models and implementing adapted control techniques to ensure the safety and effectiveness during the operation in real scenarios.

Section 1.1, summarizes these aerodynamic problems and, Section 1.1.2 specifically presents the motivation and the justification of this thesis inside the field of the aerial manipulation.

1.1 Aerodynamics: A key aspect in a flying robot

Aerodynamics, from Greek aero (air) + (dynamics), is the study of the motion of the air interacting with a solid object, such as an airplane wing or an helicopter propeller. It is a sub-field of the fluid dynamics and gas dynamics, and many aspects of the aerodynamics theory are common to these fields.

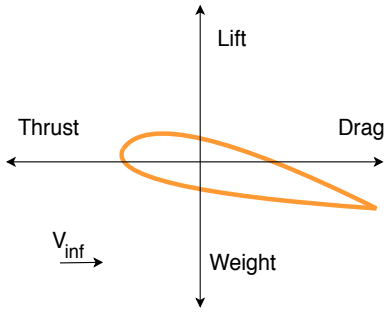

Figure 1.1: Aerodynamic forces

Understanding the motion of the air around an object (often called a flow field), enables the calculation of forces and moments acting on the object. In many aerodynamics problems, the forces of interest are the fundamental forces of the flight: lift, drag, thrust, and weight (see Figure 1.1). Of these, lift and drag are aerodynamic forces, i.e. forces due to the air flow over a solid body. The calculation of these quantities is often founded upon the assumption that the flow field behaves as a continuum. Continuum flow fields are characterised by properties, such as flow velocity, pressure, density, and temperature, which may be functions of position and time. These properties may be directly or indirectly measured in aerodynamics experiments or calculated starting with the equations for conservation of the mass, the momentum, and the energy in air flows. The density, the flow velocity, and an additional property, the viscosity, are used to classify flow fields.

The case of study of the thesis is focused on rotorcrafts. In those, the aerodynamic forces are generated moving an airfoil around an axis to produce the relative movement between the air and the solid.

1.1.1 Thrust and drag generation problem in rotorcraft

The thrust and drag generation problem has been typically studied using the blade element theory, (BET). It involves breaking a blade down into several small parts and then determining the forces on each of these small blade elements. These forces are then integrated along the entire blade and over one rotor revolution in order to obtain the forces and moments produced by the entire propeller or rotor. This is illustrated in Figure 1.2

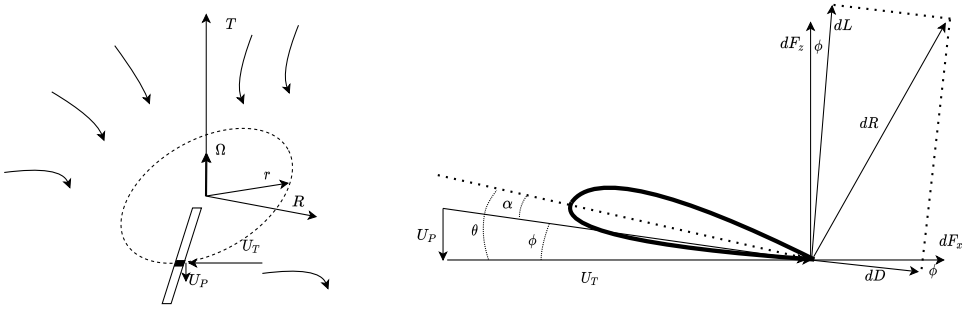

Figure 1.2: Blade element theory: Forces and velocities in a generic blade element

In this way, it is assumed that the relative velocity of each blade element can be written as:

$$U_T(r, \Psi) = \Omega r + V_\infty \cos \alpha_r \sin \psi \tag{1.1}$$

$$U_P(r, \Psi) = V_\infty \sin \alpha_r + v_i(r, \Psi) \tag{1.2}$$

$$U_R(\Psi) = V_\infty \cos \alpha_r \cos \Psi \tag{1.3}$$

Being V_∞ is the relative forward velocity, α_r the inclination of the propeller plane, the total velocity perceived by the airfoil is $U(r, \Psi) = \sqrt{U_P^2 + U_T^2}$ and the air flow inlet angle defined as $\phi(r, \Psi) = \arctan(U_P/U_T)$ is the induced angle of attack. It is concluded that the effective angle of attack is $\alpha(r, \Psi) = \theta(r) - \phi(r, \Psi)$, where $\theta(r)$ is the geometric pitch angle of the blade in r.

Assuming that the contribution of the radial velocity (U_R) to the drag is negligible.

The aerodynamic forces, lift (L) and drag D, per unit length are:

$$dL = \frac{1}{2}\rho U^2 c(r) dr C_l \tag{1.4}$$

$$dD = \frac{1}{2}\rho U^2 c(r) dr C_d \tag{1.5}$$

Projecting in the fundamental directions:

$$dF_z = dL\cos\phi - dD\sin\phi \tag{1.6}$$

$$dF_x = dL\sin\phi - DD\cos\phi \tag{1.7}$$

Where z and x represents the vertical and forward axis (Figure 1.2). Lastly, assuming that C_l and C_d are functions that only depends of the geometric of the propeller $f(r)$, it is possible to conclude that in hover conditions ($\phi = 0$), the previous integrals depends only on the geometric of the airfoil, then:

$$F_z = C_T\Omega^2 \tag{1.8}$$

$$M_d = C_D\Omega^2 \tag{1.9}$$

Where C_T and C_D are constants that again only depend on the propeller geometric. The expressions (1.8) and (1.9) are the most used and simplest formulation for the thrust, $T = F_z$, and drag, $M_d = D$ in helicopter theory.

Although 1.8 and 1.9 are the widest expressions for the aerodynamic forces generated by a rotorcraft in the robotic community, there are other approaches that aim to solve this problem in a more complete or specific way for multirotors. Those are the classical blade element momentum theory or the current lines that aim to explicitly study the aerodynamic model of multirotors [46] [47] using these classical theories or characterising experimentally the propulsion systems of those platforms [48].

1.1.2 Aerodynamic effects close to obstacles: A challenge in aerial manipulation

Aerial manipulation operations usually involve flying close to objects, structures and other obstacles. Tasks, such as, grasping or manipulating objects that are placed on the ground, over surfaces, close to walls, under surfaces or even passing very close to a surface to grasp and object while flying, require that the multirotor operates close to the obstacle while performing the manipulation operation. However, as it is well-known by the aerodynamic community, flying in an constrained environment disturbs the free development of the streamlines of a fluid producing changes that affect the complete fluid field. In the case of the aerial manipulation, since the aerial manipulators are commonly rotorcrafts, the wake produced by the movement of the propeller or propellers is distorted by the environment, leading changes in the aerodynamic problem upwards and downwards, and, consequently, it changes the performance of the rotors in terms of thrust and drag.

Then, aerodynamic effects changes the performance of the aircraft in the proximity of the obstacles, which is the nominal operation point of the aerial manipulator. In fact, in these situations, the needs of accuracy imposed to the manipulator and the aerial platform are the greatest ones because it is usually when the manipulation task is taking part. Thus, modelling and controlling this kind of aerodynamic effect is becoming essential to guarantee that the manipulation operation can be successfully performed at the same time that the aerial platform is working under safety conditions.

Traditionally, the most common of these aerodynamic effects is the one produced by flying close to the ground. This phenomenon, usually known in the literature as ground effect, is more pronounced in rotorcrafts operating in hover and low speed. For rotor-craft hovering close to the ground, the rotor wake must rapidly expand as it approaches the surface, transitioning from the almost vertical down-wash to radial out-wash parallel to the ground. This alters the velocity of the slipstream and the induced velocity, which then affects the rotor thrust and power. The ground effect in helicopters has been well researched in literature [49], [50], [51] and has been studied for the take-off, landing, and hovering close to the ground [52], [53], [54]. However, for

multirotors, it had not received much attention at the start of this work, although these platforms were being increasingly used in multiple applications.

The influence of ground effect in helicopters has been studied through the use of an underlying aerodynamic model or empirically. A classical analytical model for the ground effect is provided by [49], which uses the assumptions of the linearised potential aerodynamics placing a single source to model the rotor airflow and the method of images to account for the ground effect. Other authors have provided empirical expressions for the rotor thrust increment in ground effect for large [51] and small UAV helicopters [55]. However, the model of [49] has been, traditionally, the most used in robotics because it has a simple analytical form, which experimentally addresses the relationship between the rotor thrust in ground effect and the rotor height over the ground surface with enough accuracy

As it was beforementioned, the ground effect in multirotors has received much less attention. Several papers deal with the aerodynamic models of multirotors [56], which are used for navigation [57] or even for power control [58]. Disturbance observers have become popular in the last years for estimating external wrench in multirotors [59], [60]. In most cases, it is assumed that the external disturbance source is unique and mainly contact forces [61], [62] or wind. In [63], the simultaneous online estimation of aerodynamic and contact forces is studied to discriminate between them and compute the wind velocity by means of model inversion. However, disturbance observers have not been used for the ground effect estimation.

The influence of the ground effect has been considered in the development of controllers for low-altitude flight in [64] using an adaptive controller and a height estimator that works well in the experiments, although false measurement from the ultrasonic sensor can destabilise the system. A take-off and landing controller that uses an ant colony filter for estimation of the ground effect is presented in [65]. The algorithm is tested in simulation with PID and sliding modes controllers, and in both cases the consideration of the ground effect improves significantly the controller performance. In [66], a PID landing controller with a ground effect robust compensator has been presented. The experimental tests show that accounting for the ground effect improves the controller behaviour. Also, the ground effect estimation using a

vision sensor to estimate distance to obstacles and learning from previous flights has also been proposed [67]. A dynamic controller for rotorcrafts landing and hovering in ground effect using feedback control based on flow field estimation has also been developed and tested in simulation [68].

However, in almost all cases, the model of the ground effect in [49] is assumed or evaluated for a single rotor. The only experimental results that have been reported, making experiments with a small quadrotor flying in hover over the ground at different heights [69] and using a test bench [70], suggest that the ground effect in multirotors may be larger than predicted by [49], although the issue had not been further analysed at the beginning of this work.

Although, the ground effect has been the most studied aerodynamic effect, a similar effect is caused by flat surfaces placed above the rotors, known as the ceiling effect. This phenomenon induces an additional thrust on the robot, pushing it towards the ceiling. Thus, this fact can be dangerous for standard multirotors because propellers and engines may collide with the ceiling and break, or destabilise the platform.

Ceiling effect is relevant in applications in which the aerial manipulators fly close to an obstacle from the underside. For instance, in [71], authors proposed using an aerial manipulator with the arm attached on top of the multirotor body above the rotors for conducting the inspection by the contact of bridge elements without any human intervention, since the arm can be used to hold the ultrasound sensor that should be in contact with the bridge while the multirotor is hovering [72].

Although the ground and ceiling effects are the most significant aerodynamic ones, there are others that could arise in the current application scenery of the aerial manipulators. This is the case of flying, for example in narrow environments, such us tunnels, mines or cluttered and close environments, like tanks or vessels. In other cases, it is necessary to fly in complex environments, such us chemical plants or refineries to carry out inspection and maintenance operations. All these situations produce different aerodynamic disturbances that could be decisive to guarantee the reliability and suitability of using UAVs in real contact-based operations.

1.2 Scope of this work

This Ph.D falls within the framework of three research projects funded by the European Commission. The first project is entitled "AErial RObotic system integrating multiple ARMS and advanced manipulation capabilities for inspection and maintenance" (AEROARMS) [73] proposes the development of the first aerial robotic system with multiple arms and advanced manipulation capabilities to be applied in industrial inspection and maintenance (I&M). The second one "AErial RObotic System for In-Depth Bridge Inspection by Contact" (AEROBI) [33] intends to develop a robotic system to inspect the bridges and assess their status. The third project is the "AERIAL COgnitive integrated multi-task Robotic system with Extended operation range and safety" (AERIAL CORE) [36] project which is about infrastructure inspection of large infrastructure.

Thus, the thesis is focused on the modelling and characterisation of the aerodynamic effects that arise in aerial manipulators when flying in the proximity of obstacles and their applications in the context of the aforementioned projects, developing control and planning techniques which take the previous models and characterisations into account. Moreover, the work of this thesis has been done in order to take the greater range of possibilities that can arise in that aerial robotic manipulation applications into consideration.

The workflow of the research includes the following tasks:

- Study of aerodynamic effects of flying close to obstacles. This involves studying the effect on the performance of UAVs and the deficiencies of current control techniques when flying near obstacles. In particular, these aspects have been addressed when the UAV flies in:
  - The proximity to flat surfaces: floor, ceiling, etc.
  - Industrial environments similar to those of the AEROARMS project: flights of the UAV near pipes, studying the flow around pipes...
  - Environments close to bridges or infrastructures similar to those of the AEROBI project: UAV flight near the ceiling and pillars.

- Study of the thrust generation in conventional rotors of a multirotor: The study of the characteristics of the typical motorisation of this type of UAVs. In particular, it focuses on characterising and modelling its optimal regime, behaviour in different conditions and in the proximity to obstacles.

- Advanced study of the influence of flying in the proximity to surfaces: This task consists of modelling, the static study and the study in dynamic conditions of the different disturbances. Disturbances have been studied in different UAVs, with different sizes and configurations. The final objective of this part is the development of aerodynamic effects maps.

- Estimation of aerodynamic effects to be considered in the controller: This part of the thesis consists of the estimation of aerodynamic effects in order to take them into account in the UAV controller. It is the integration of aerodynamic effects maps of the previous section and the models effect in the environment in the controllers. The ultimate goal is to estimate external forces and moments only with navigation sensors.

- Multirotor control techniques with aerodynamic effects: In the study of multirotor control techniques, the classic linear and non-linear control techniques (backstepping, passivity, etc.) and their behaviour have been discussed before the aerodynamic disturbances.

- The applications of the models in planning techniques which take the aerodynamic behaviour when flying close to obstacles into account, in order to generate more efficient and safer trajectories.

- Experimental validation of aerodynamic controllers: The objective of this phase is the validation with real flights of the aerodynamic control techniques developed in the previous phases. These experiments have been carried out in the scenarios of the AEROARMS and AEROBI projects.

1.3 Contribution of the work

The main contribution of this work consists of generating a scientific background of the aerodynamic effects that can affect aerial manipulators, as well as the consideration of them in pursuit of safety and effectiveness while carrying out the manipulation task in the framework of the AEROARMS and AEROBI projects.

In the following, it is presented a timeline (Figure 1.3) with the different contributions and works developed. Although the study of the behaviour of the flow has been widely studied, particularly, in ground effect from different points of view, the scheme only shows previous studies that have been widely extended along the robotic community [49] [51].

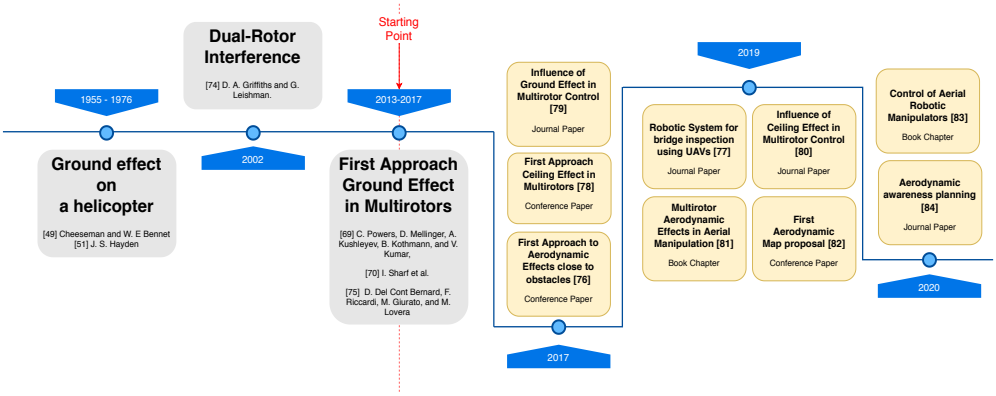

Figure 1.3: Timeline of the contributions of the thesis

As it was aforementioned, at the beginning of this research in 2015, there was not a deep background in the characterisation of aerodynamic effects in multirotors. In fact, there were only first approaches to them that were inherited from the classical helicopter aerodynamic ground effect and a few results applied to tandem rotors [74] and multirotor [69] [70] [75]. Moreover, the knowledge about other aerodynamic effects different from the ground effect was restricted to the ceiling effect [69]. In fact, the approach of studying these aerodynamic effects in aerial manipulators was practically non-existent.

This work has contributed to this research community being one of the first that analysed the aerodynamic effects when a rotor works close to different kinds of obstacles in a general approach, studying not only the ground and ceiling effect but also the effect of flying close to a wall or a corner and the combined effect of two rotors working together [76], putting an special interest in the ceiling effect in the following publications [77], [78]. It was also the first research that considered the interaction of the flow-field with the quadrotor body through a combined experimental and the CFD analysis to adapt the previous theoretical results of helicopters to multirotors including also the use of model-based controllers to predict the behaviour of the multirotor in presence of these obstacles [79], [80]. The author also proposed a study of the generalisation of the classical method based on the linearised potential aerodynamics and published a chapter about the aerodynamic effects that are suitable to appear in aerial manipulators in [81]. Lastly, the contribution of [82] and [83] open a whole world of possibilities with the proposal of developing an aerodynamic effect map which could be applied to more complex control strategies or in an aerodynamic awareness planning algorithm [84] and specific aerodynamic awareness controllers.

Extra contributions

In addition to the work briefly described above, the author of this thesis has contributed to different publications about aerial manipulation [29], [23], to a new concept of spherical drone with autonomous indoor localisation [85], to propose a cybersecurity solution in the UAV architecture to be deployed in post-disaster situations [86] and to design a new concept of robot for inspection in oil and gas industries and aerial physical interaction with in grabbing conditions with a compliant dual-arm aerial manipulator. Details of those papers are included on the list of publication in Section 1.4.

Moreover, the author is decision pending of one journal paper about multirotor autopilot system for fast prototyping solutions, two journal publications about the results obtained in the MBZIRC competition and a IEEE Transaction on Industrial Electronics which presents a fully autonomous operation of an aerial robot.

1.4 List of publications

1.4.1 Published papers

Journal Papers

- Pedro J. Sanchez-Cuevas, G. Heredia, and A. Ollero, Characterization of the Aerodynamic Ground Effect and Its Influence in Multirotor Control. International Journal of Aerospace Engineering, vol. 2017, 2017.

- Pedro J Sanchez-Cuevas, Pablo Ramon-Soria, Begoña Arrue, Anibal Ollero, and Guillermo Heredia. Robotic system for inspection by contact of bridge beams using uavs. Sensors, 19(2):305, 2019.

- Antonio E Jimenez-Cano, Pedro J Sanchez-Cuevas, Pedro Grau, Anibal Ollero, and Guillermo Heredia. Contact-based bridge inspection multirotors: Design, modeling, and control considering the ceiling effect. IEEE Robotics and Automation Letters, 4(4):3561-3568, 2019.

- Salua Hamaza, Ioannis Georgilas, Manuel J Fernandez, Pedro J Sanchez-Cuevas, Thomas Richardson, Guillermo Heredia, and Anibal Ollero. Sensor installation and retrieval operations using an unmanned aerial manipulator. IEEE Robotics and Automation Letters, 2019.

- Pedro J. Sanchez-Cuevas, Antonio Gonzalez-Morgado, Nicolás Corteś, Diego Benjumea-Gayango, Antonio E. Jimenez-Cano, Anibal Ollero and Guillermo Heredia. Fully-Actuated Aerial Manipulator for Infrastructure Contact Inspection: Design, Modeling, Localization, and Control. Sensors, 20(17), 4708, 2020

- Alvaro Caballero, Pedro J. Sanchez-Cuevas, Manuel Bejar, Guillermo Heredia and Anibal Ollero. An aerodynamic extension for motion planning with dynamics awareness in aerial long-reach manipulators. International Journal of Aerospace Engineering, vol. 2020, 2020.

- Alejandro Suarez, Alvaro Caballero, Ambar Garofano, Pedro J. Sanchez-Cuevas, Guillermo Heredia and Anibal Ollero, Aerial Manipulator With Rolling Base for Inspection of Pipe Arrays. IEEE Access, vol. 8, pp. 162516-162532, 2020.

Conference Papers

- Pedro J. Sanchez-Cuevas, G Heredia, and A Ollero. Multirotor uas for bridge inspection by contact using the ceiling effect. In 2017 International Conference on Unmanned Aircraft Systems (ICUAS), pages 767-774. IEEE, 2017.

- Pedro J. Sanchez-Cuevas, Guillermo Heredia, and Anibal Ollero. Experimental approach to the aerodynamic effects produced in multirotors flying close to obstacles. In Iberian Robotics Conference, pages 742-752. Springer, 2017.

- Pedro J. Sanchez-Cuevas, Victor Martín, Guillermo Heredia and Aníbal Ollero Aerodynamic effects in multirotors flying close to obstacles: Modelling and mapping. In Iberian Robotics conference, pages 63-74. Springer, 2019.

- Alejandro. Suárez, Pedro J. Sanchez-Cuevas, Manuel Fernandez, Manuel Perez, Guillermo Heredia, and Anibal Ollero (2018, October). Lightweight and compliant long reach aerial manipulator for inspection operations. In 2018 IEEE/RSJ International Conference on Intelligent Robots and Systems (IROS), pp. 6746-6752, IEEE, 2018.

- Agustin Ramos, Pedro J. Sanchez-Cuevas, Guillermo Heredia and Anibal Ollero. Spherical fully covered uav with autonomous indoor localization. In Iberian Robotics conference, pages 355-367. Springer, 2019.

- Manuel Fernandez, Pedro J. Sanchez-Cuevas, Guillermo Heredia and Anibal Ollero. Securing UAV communications using ROS with custom ECIES-based method. International Workshop on Research, Education and Development on Unmanned Aerial Systems. RED-UAS 2019, Cranfield.

- Abraham López, Pedro J. Sanchez-Cuevas, Alejandro Suarez, Ambar Soldado, Anibal Ollero, and Guillermo Heredia. MHYRO: Modular HYbrid RObot for

contact inspection and maintenance in oil&gas plants. In 2020 IEEE/RSJ International Conference on Intelligent Robots and Systems (IROS), IEEE, 2020.

Book Chapters

- Pedro Sanchez-Cuevas, Guillermo Heredia, and Anibal Ollero. Multirotor aerodynamic effects in aerial manipulation. In Aerial Robotic Manipulation, pages 67-82. Springer, 2019.
- Guillermo Heredia, Pedro J. Sanchez-Cuevas, Control of Aerial Robotic Manipulators. In Encyclopedia of Robotics. Springer, 2020.

1.4.2 Submitted Papers

Journals

- Carlos R. de Cos, Manuel J. Fernandez, Pedro J. Sanchez-Cuevas, Jose A. Acosta and Anibal Ollero. MAS+: A High-Level Modular Autopilot Solution for Fast Prototyping of Unmanned Aerial Systems. IEEE Access.
- Fran Real, Angel Castaño, Jesus Capitan, Pedro J. Sanchez-Cuevas, Manuel Fernandez, Manuel Villar, and Anibal Ollero. Autonomous Fire-fighting with Heterogeneous Team of Unmanned Aerial Vehicles. Field Robotics
- Fran Real, Angel Castaño, Jesus Capitan, Pedro J. Sanchez-Cuevas, Manuel Fernandez, Honorio Romero, and Anibal Ollero. A Team of Multiple Unmanned Aerial Vehicles for Cooperative Construction. IEEE Access
- Pedro J. Sanchez-Cuevas, Alejandro Suarez, Pablo Ramon-Soria, Manuel Fernandez, Rafael Salmoral, Guillermo Heredia, Begoña C. Arrue, and Anibal Ollero. Compliant Dual Arm Aerial Manipulator to Grasping and Installation of Inspection Tool in Industrial Environments. IEEE Transactions on Industrial Electronics

- A. Suarez, Pedro J. Sanchez-Cuevas, Guillermo Heredia, Anibal Ollero. Aerial Physical Interaction in Grabbing Conditions with Lightweight and Compliant Dual Arms. Applied Science

- Pedro J. Sanchez-Cuevas, Pablo Ramon, Manuel Perez-Jimenez, Manuel J. Fernandez, Victor Vega, Anibal Ollero, and Guillermo Heredia. Aerial robotic system for in-depth autonomous bridge inspection by contact. Automation in Construction

1.5 Organization of the thesis

The content of the thesis is organised as follows: Chapter 2 introduces and models the aerodynamic effects in multirotor and identifies where these are taking part. Following this, it is presented and analysed the methods used to approach these aerodynamic effects in this work, and lastly, the different cases of use in which the aerodynamic effect has been taken into account are introduced. This chapter is specifically focused on studying aerodynamic effects assuming that obstacles are uniform and much larger than the propeller. In this case, the obstacle is assumed to be an infinity surface and then, the effect only depends on the distance between the propeller plane and the obstacle.

Chapter 3 and 4 are about two different cases of use in which the aerodynamic effect has been taken into account from the control point of view. The first case of use (Chapter 3) specifically treats the problem of flying very close to an obstacle from the upper-side while accomplishing, for example, a manipulation operation. The second one (4) is about dealing with the ceiling effect while the aerial platform inspects a bridge.

Chapter 5 makes a twist to the modelled aerodynamic effect in Chapter 2. In this case, the author goes beyond trying to model not only the aerodynamic effect over or under an infinite obstacle, but also how this effect starts to be significant as a rotor approaches them (finite obstacles). Those mean that, in this case, the aerodynamic effects depends not only on the distance between the propeller plane and the obstacle,

but it also depends on the relative positions between them. As a result of these models, aerodynamic effect maps have been generated, which could be used by a path planner or a new control strategy to take the aerodynamic effect in a general way into account. In this way, the results of a collaboration work in which this aerodynamic map has been included in an aerodynamic awareness planner are presented.

Chapter 6 concludes and presents future works to follow the research line about aerodynamic effects in aerial manipulators.

To sum up, Figure 1.4 illustrates the different chapters of the document and their relations.

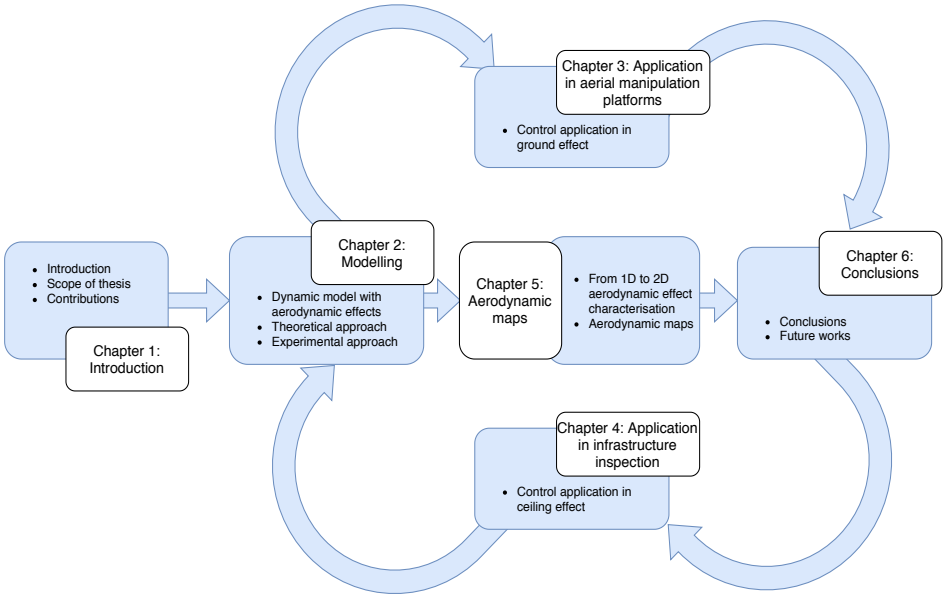

Figure 1.4: Scheme of the thesis

Chapter 2

Modelling

> If the doors of perception were cleansed every thing would appear to man as it is, Infinite. For man has closed himself up, till he sees all things thro' narrow chinks of his cavern.
>
> William Blake

2.1 Introduction

As it was mentioned in Chapter 1, aerial manipulators are usually involved in applications which require flying close to different structures, objects and obstacles. These situations arise, for example, when grasping objects or carrying out inspection by contact tasks [71][87][78] and they lead to situations in which the wake developed by the rotor is constrained by the environment producing changes in the thrust and torque exerted by the rotors.

The case of flying close to a ground surface has been widely studied in helicopters theory [49][51]. The model presented in [49], is the most known and used theoretical

result for the ground effect of a rotary wing, and it is based on the potential aerodynamic assumptions, which impose that the velocity field is solenoidal and irrotational. Therefore, the velocity field is the gradient of a potential function, $\vec{v} = \vec{\nabla}\phi$

However, despite of the impact that multirotors have had in the last years, the effect of flying close to the ground with them has received much less attention. The same happens if the multirotor flies close to other obstacles, like ceilings, walls, pipes and the combination of these kinds of effects. These problems had not been deeply studied at the beginning of this work. Nevertheless, the few experimental results that had been reported making experiments with a small quadrotor flying hover over the ground at different heights [69] [70] [78] and [76] suggested that the ground effect in multirotors is larger than the predicted in the classic theories [49] [51].

The first goal of this thesis aims to fill this gap in literature presenting a first functional approach to these aerodynamic effects which could be taken into account in several aerial manipulation tasks. Thus, the structure of this chapter is summarised as follows: Section 2.2 iintroduces a new formulation of the dynamic model of an aerial manipulator, in which these aerodynamic effects have been considered to understand how they affect the global performances of the aerial platform. Section 2.3.2 presents the classical theory used to solve this problem in helicopters and a generalisation of this method is applied to a quadrotor in Section 2.3.2. Section 2.4.1 describes the experimental environment developed in this thesis to experimentally assess these aerodynamic effects. Lastly, Section 2.5 collects the experimental results followed by brief conclusions of how these kinds of aerodynamic effects affect the aerial robot performance in Section 2.6.

The content of this chapter is based on the following publications:

- Pedro J. Sanchez-Cuevas, Guillermo Heredia, and Anibal Ollero. Experimental approach to the aerodynamic effects produced in multirotors flying close to obstacles. In Iberian Robotics Conference, pages 742-752. Springer, 2017.

- Pedro Sanchez-Cuevas, Guillermo Heredia, and Anibal Ollero. Multirotor aerodynamic effects in aerial manipulation. In Aerial Robotic Manipulation, pages 67-82. Springer, 2019.

- Pedro J. Sanchez-Cuevas, G. Heredia, and A. Ollero, Characterization of the Aerodynamic Ground Effect and Its Influence in Multirotor Control. International Journal of Aerospace Engineering, vol. 2017, 2017.

- Pedro J. Sanchez-Cuevas, G Heredia, and A Ollero. Multirotor uas for bridge inspection by contact using the ceiling effect. In 2017 International Conference on Unmanned Aircraft Systems (ICUAS), pages 767-774. IEEE, 2017.

2.2 Dynamic model of a multirotor with aerodynamic effects

This section aims to present the inclusion of taking the aerodynamic effects into account, starting from the classical dynamic model of a multirotor to the emphasis of the significance of the aerodynamic effects in this chapter. The derivation of the classical dynamics of aerial manipulators which is used is well-known in the research community, [88][89]. The two classical formulations are compiled in Appendix A. Furthermore, this formulation has been adapted and reformulated in Chapter 3 and Chapter 4 to be included in the controllers in a proper and efficient way.

Then, according to the reference [89] and the Appendix A,the dynamic model for a multirotor and a k-link manipulator arm used in this work has been obtained using the Euler-Lagrange formulation. If the generalised coordinates of the multirotor have been defined as $\boldsymbol{\xi} = [\mathbf{p} \quad \boldsymbol{\eta} \quad \boldsymbol{\gamma}]^T \in \Re^n$, with $n = 6 + k$; and $\mathbf{p} = [x \quad y \quad z]^T$ represents the translation coordinates of the multirotor center of gravity relative to the inertial frame, $\boldsymbol{\eta} = [\phi \quad \theta \quad \psi]^T$ describes the vehicle attitude by the classical roll, pitch, yaw Euler angles commonly used in aerospace applications, and $\boldsymbol{\gamma} = [\gamma_1 \quad \gamma_2 \quad ... \quad \gamma_k]^T$ are the joint angles of the arm. The dynamic equations of the multirotor could be written as:

$$\boldsymbol{M}(\boldsymbol{\xi})\ddot{\boldsymbol{\xi}} + \boldsymbol{C}(\boldsymbol{\xi}, \dot{\boldsymbol{\xi}})\dot{\boldsymbol{\xi}} + \boldsymbol{G}(\boldsymbol{\xi}) = \boldsymbol{\mathfrak{F}} + \boldsymbol{\mathfrak{F}}_{\mathfrak{E}} \tag{2.1}$$

where $\boldsymbol{M}$ is the inertia matrix, the Coriolis and centrifugal terms are represented by $\boldsymbol{C}$ and the gravitational force terms are described by $\boldsymbol{G}$, $\mathfrak{F}$ is the vector of forces and torques generated by the actuators. It can be decomposed into the thrust forces $\boldsymbol{F_Q}$ and moments, $\boldsymbol{\tau_Q}$ generated by the rotors, and the torque of each link of the manipulator, $\boldsymbol{\tau_M}$. External forces and moments are represented by $\boldsymbol{F_E}$, which include the contact forces and moments of the end effector.

However, in case of a flight under the influence of an aerodynamic effect, the generalised vector force changes because the forces change due to the relative position between the multirotor and the different obstacles of the environment, so the generalised vector is a function of the state of the multirotor: $\mathfrak{F} = \mathfrak{F}(\dot{\boldsymbol{\xi}})$. Thus, the dynamic model is rewritten as:

$$\boldsymbol{M}(\boldsymbol{\xi})\ddot{\boldsymbol{\xi}} + \boldsymbol{C}(\boldsymbol{\xi}, \dot{\boldsymbol{\xi}})\dot{\boldsymbol{\xi}} + \boldsymbol{G}(\boldsymbol{\xi}) = \mathfrak{F}(\boldsymbol{\xi}) + \mathfrak{F}_{\mathfrak{E}} \tag{2.2}$$

Then, it is clear that considering this aerodynamic effect affects the dynamics of the full system, and it is necessary to take it into account in such applications that require operating close to obstacles, like a ground or ceiling in a accurate way.

2.3 Analytical Modelling based on potential flow

2.3.1 Classical method

The classic method used to approach the aerodynamic effect presented in this chapter was introduced by [90] and [49] using the assumptions of the linearised potential aerodynamics (Appendix B).

In the first theoretical study, Zbrozek [90] proposed to model the rotor as a sink of constant strength, $s = Av_i/4\pi$, where R is the rotor radius and v_i is the velocity induced by this rotor. However, this expression was reinterpreted by Cheeseman in [49] proposing changing the sink by a source due to the flow pattern beneath a lifting rotor resembles a source rater than a sink. Then, the expression of the potential flow is:

$$\phi = \frac{-s}{\sqrt{(x-x_0)^2 + (y-y_0)^2 + (z-z_0)^2}} \tag{2.3}$$

In order to model the effect of a surface like a ground, this classical approach used the method of the images placing a "virtual rotor" on the opposite side of the surface and at the same distance and with the same strength. This method uses the symmetry conditions to create a "virtual surface" (like the ground) in which the normal velocity is zero and the impenetrability condition is ensured, which is $\boldsymbol{n} \cdot \nabla\phi = 0$, where $\boldsymbol{n}$ vector normal to the ground surface, $\cdot$ is the scalar product and $\nabla\phi$ represents the velocity vector derived from the potential equation (2.3) according to the assumptions of the linearised potential aerodynamic.

In this way, using equatoin (2.3) and images method, the potential equation of the problem illustrated in Figure 2.3.1, this can be written as (2.4). This expression models a single rotor, placing one rotor in $x = 0$, $y = 0$ and $z = h$ and the image rotor in $x = 0$, $y = 0$ and $z = -h$, in this way, the distance to the ground is assumed as h.

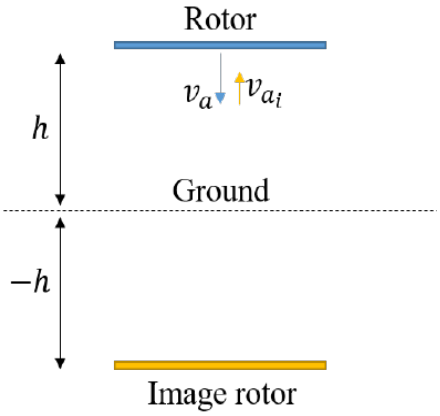

Figure 2.1: Scheme of the aerodynamic problem modeled with the images method for one rotor: v_a represents the induced velocity by the rotor and v_{a_i} is the induced velocity in the rotor by the image rotor.

$$\phi = \frac{-s}{\sqrt{x^2 + y^2 + (z-h)^2}} + \frac{-s}{\sqrt{x^2 + y^2 + (z+h)^2}} \tag{2.4}$$

Assuming that the power rotor at zero air speed could be written as $P = Tv_i$, where T is the thrust and v_i is the induced velocity by the rotor.

Therefore, at constant power, $T_{OGE}v_{i_{OGE}} = T_{IGE}v_{i_{IGE}}$, we can write:

$$\frac{T_{IGE}}{T_{OGE}} = \frac{v_{i_{OGE}}}{v_{i_{IGE}}} \tag{2.5}$$

where the subindex IGE and OGE refer to conditions inside and outside the ground effect. If $v_{i_{OGE}}(x = 0, y = 0, z = h) = v_a$ and $v_{i_{OGE}}(x = 0, y = 0, z = h) = v_a - \delta v_{a_i}$, where δv_{a_i} is the velocity induced by the image rotor (located in $z = -h$) in the position of the rotor $(x = 0, y = 0, z = h)$, according to the Figure 2.3.1.

Then, expression (2.5) can be written now as follows:

$$\frac{T_{IGE}}{T_{OGE}} = \frac{1}{1 - \frac{\delta v_{a_i}}{v_i}} \tag{2.6}$$

Then, δv_{a_i} can be obtained following the aerodynamics assumptions which say that the axial velocity field can be obtained partially deriving (2.4) with respect to the axial direction, $v_a(x, y, z) = \frac{\partial \phi}{\partial y}$ and substituting the values of $x = 0, y = 0, z = h$.

Deriving, it is possible to obtain the expression (2.7) which shows the axial velocity induced by the mirror-image rotor called as $v_{a_i}(x, y, z)$.

$$v_{a_i}(x, y, z) = \frac{\partial \phi}{\partial z} = \frac{s(z + h)}{\sqrt{(x^2 + y^2 + (z + h)^2)^3}} \tag{2.7}$$

substituting in 2.7, the values of $x = 0, y = 0, z = h$ and taking into account that $s = Av_i/4\pi$, it is concluded that:

$$\delta v_{a_i} = \frac{R^2 v_i}{16h^2} \tag{2.8}$$

Therefore, generalizing for any $h = z$,

$$\frac{T_{IGE}}{T_{OGE}} = \frac{1}{1 - \frac{1}{16}(\frac{R}{z})^2} \tag{2.9}$$

Although other authors have presented empirical expressions for the increment of rotor thrust in ground effect which show similar results [51] [55], the "Potential Flow

with the method of Images" (PFI) model presented in [49] and summarised in this chapter have been widely used because it has the simplest analytical form and has been experimentally shown to accurately capture the relationship between the rotor thrust in ground effect and the rotor height over the ground surface.

To obtain a visual description of the flow field represented by the potential flow, the expressions of the velocities:

$$v_x(x,y,z) = \frac{\partial \phi}{\partial x} = \frac{sx}{\sqrt{(x^2+y^2+(z+h)^2)^3}} + \frac{sx}{\sqrt{(x^2+y^2+(z-h)^2)^3}} \tag{2.10}$$

$$v_y(x,y,z) = \frac{\partial \phi}{\partial y} = \frac{sy}{\sqrt{(x^2+y^2+(z+h)^2)^3}} + \frac{sy}{\sqrt{(x^2+y^2+(z-h)^2)^3}} \tag{2.11}$$

$$v_z(x,y,z) = \frac{\partial \phi}{\partial y} = \frac{s(z+h)}{\sqrt{(x^2+y^2+(z+h)^2)^3}} + \frac{s(z-h)}{\sqrt{(x^2+y^2+(z-h)^2)^3}} \tag{2.12}$$

has been obtained and represented in the Figure 2.3.1, in such a way that $\boldsymbol{v} = [v_x(x,y,z) \quad v_y(x,y,z) \quad v_z(x,y,z)]'$

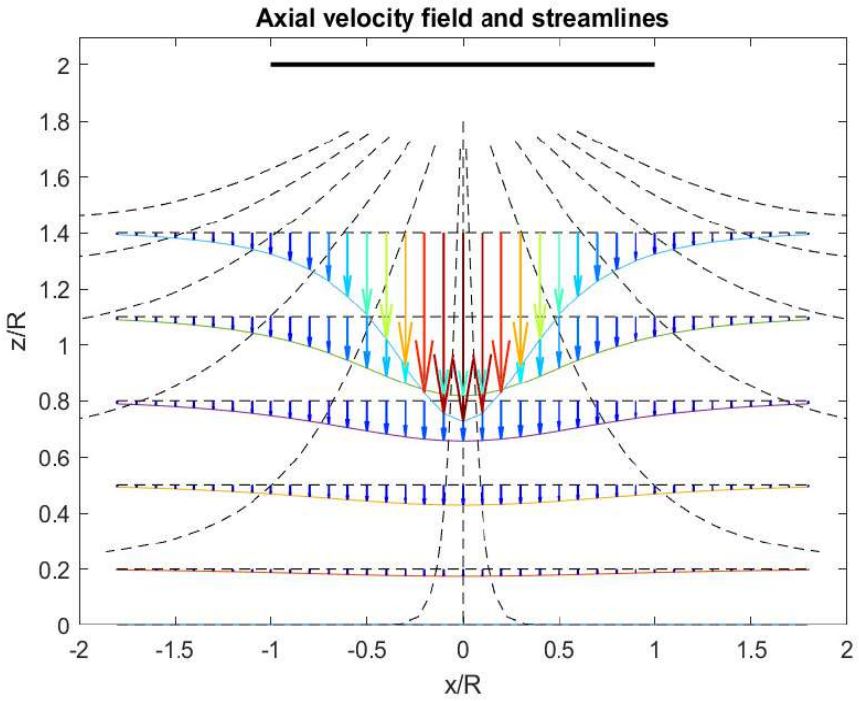

Figure 2.2: Axial Velocity and streamlines of PFI model.

2.3.2 PFI generalization to Multirotors

The formulation applied to the case of a single rotor in ground effect presented before can be extended to the case of a complete multirotor with n rotors. In this case, each rotor is replaced by a source like the presented in Figure 2.3 of the Section 2.3 and the ground by an image source of equal strength placed below this rotor at a distance equal to twice the height of the rotor. However, it is important to remark that all image sources induce changes in all rotors so it is necessary to rewrite the expression of the v_{IGE} to take the axial velocity induced by the other rotors into account.

For example, in the case of a quadrotor with all rotors equally spaced (see Figure 2.3), the expression for v_{IGE} can be rewritten as (2.13):

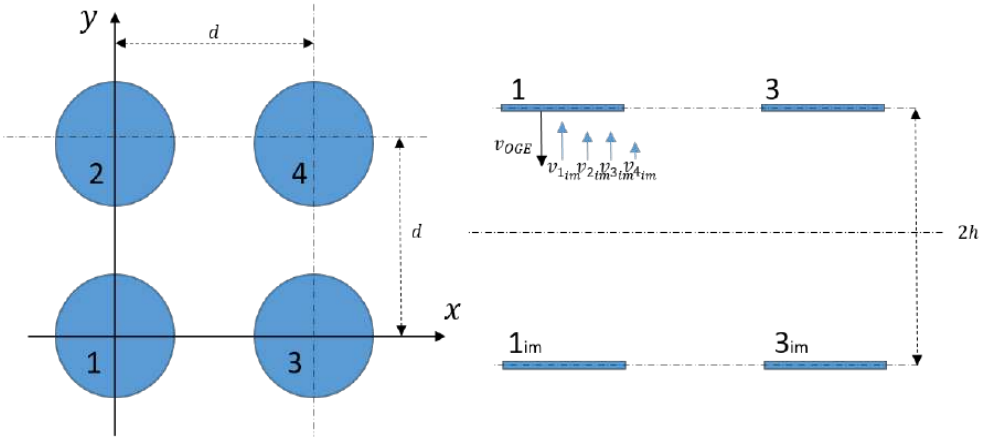

Figure 2.3: Illustration of the induced velocities applying the method of images in a general quadrotor. $v_{i_{im}}$ is the influence of the image rotor placed in i on the rotor 1

$$v_{IGE} = v_{OGE} - \delta v_{11im} v_{OGE} - \delta v_{21im} v_{OGE} - \delta v_{31im} v_{OGE} - \delta v_{41im} v_{OGE} \tag{2.13}$$

where $v_{ij_{im}}$ is the influence of the image rotor placed in i on the rotor j. All the rotors are influenced equally and in the case of the assumption that the power remains constant $T_{IGE} v_{IGE} = T_{OGE} v_{OGE}$ for the complete multirotor, the following expression can be obtained:

$$\frac{T_{IGE}}{T_{OGE}} = \frac{1}{1 - (\frac{R}{4z})^2 - R^2 \frac{h}{\sqrt{(d^2+4h^2)^3}} - \frac{R^2}{2} \frac{h}{\sqrt{(2d^2+4h^2)^3}}} \tag{2.14}$$

Then, in a general way in which we have a multirotor composed of N rotors which are not at the same distance (Figure 2.4). It is possible to express the theoretical ground effect using the expression (2.15):

$$\frac{T_{IGE}}{T_{OGE}} = \frac{1}{1 - (\frac{R}{4z})^2 - \frac{R^2}{2} \sum_{i=2}^{N} \frac{h}{\sqrt{(d_i^2+4h^2)^3}}} \tag{2.15}$$

where d_i is the relative distance between the i rotor and the reference rotor with $i = 1$. In this way, it is possible to obtain the value of $\frac{T_{IGE}}{T_{OGE}}$ for the rotor $i = 1$, which can be generalised to the full multirotor because it is dimensionless.

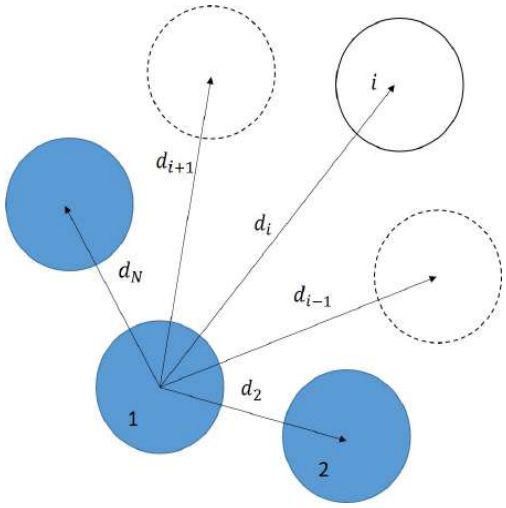

Figure 2.4: Generic multirotor schematics.

This result follows the basis used and widely tested to approach the aerodynamic ground effect in a single rotor, however, it is not enough to demonstrate if it is valid or not. Then, this thesis follows a detailed experimental part in which this theoretical model is compared with those previous results, especially with the result of the expression (2.14) to validate the generalisation of the theoretical approach.

2.4 Experimental modelling of aerodynamic effects - Methods and Materials

As it was aforementioned, it has been considered necessary to be able to assess the aerodynamic ground effect of a multirotor in a realistic setup which allows carrying out experiments with multirotors in multiple configurations. In order to aim this goal, a test stand was built for an experimental motor/rotor aerodynamic characterisation close to surfaces. This is presented in Section 2.4.1. Moreover, an experimental procedure has also been defined to properly compare the results obtained through the experimental characterisation (Section 2.4.1) ensuring that all the experiments are accomplished in a controlled which permits the comparison of the experimental results in a correct way.

2.4.1 Test stand

This section describes the test stand developed in this thesis, which will be used later to validate the theoretical results and model different aerodynamic effects in multirotors.

To sum up, the test stand is intended to measure the thrust of the propellers in the presence of different types of surfaces, such as ground, ceiling, wall or circular surfaces.

Then, the test stand should address two kind of requirements.

On the one hand, the physical requirements are:

- Asses aerodynamic effects on multiple types of surfaces and obstacles
- Accomplish each experiment with the possibility of moving the distance between the rotors and the obstacle
- Be able to change the relative angle between the rotor and the obstacle
- The possibility of assessing the aerodynamic effect in different kinds of surfaces, flat, rough, grid...

- Capacity to assess more than one rotor at the same time (tandem rotor or coaxial configuration)
- Be able to assess a complete small size multirotor

On the other hand, the functional requirements are:

- It is necessary to obtain the data of the thrust developed by the rotor, rotors or the complete multirotor.
- It is necessary to log the rpm of the rotor
- It is necessary to be able to measure and control the pwm commanded to the rotors

The result that addresses those requirements is the test stand presented in Figure 2.5.

The test-bench consists of an isostatic L-shaped structure that integrates a load cell in its lower endpoint and the rotor, whose aerodynamics will be characterised in the distal end of the vertical part (see Figure 2.5.E). Additionally, a cylindrical joint, γ, allowing free rotation of the structure, has been used to avoid any resultant force in the holder between the ground basis and the corner intersection of the L-shaped structure. An analysis of the force balance in this structure allows to calculate the rotor thrust F_3 through the measurement of the reaction force F_{lc} applied to the load cell. The resultant equation of equilibrium is the following:

$$F_3 = F_{lc}\frac{d_h}{d_v} \tag{2.16}$$

Where d_h and d_v are the dimensions depicted in Fig 7.b. Regarding the electronics embedded in the structure, the test-bench integrates an Arduino Mega 2560 as a data acquisition unit and it includes sensors to measure the rotor speed as well as a load cell to collect the measurements of the reaction force, Flc. Moreover, the PWM signal commanded to the rotor is monitored at the output using an interruption-based algorithm which runs in the board. The Arduino Mega 2560 is connected through

the serial port to a PC with MATLAB that offers a graphical interface to process, displays and saves the data collected by the sensors. Moreover, the test stand has a bearing system that allows tests with different distances and inclination angles of the rotor plane with respect to the obstacle surface as it is shown in Figure 2.5.A/B/C/D. Moreover, changing the obstacle or surface behind, it is clear that the test stand can be used to test several obstacle conditions but, in this case, we are interested in the ceiling effect results.

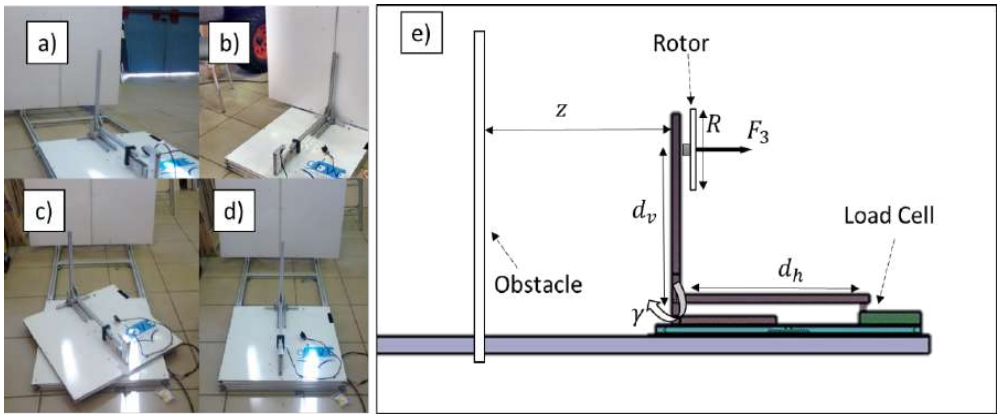

Figure 2.5: Test stand used for the characterization of the aerodynamic effects. a), b), c) and d) shows different setups of the test-bench. e) illustrates the variables involved in the measurement process

Figure 2.6 shows how this device is also able to mount different rotor configurations and even a complete multirotor.

Experimental procedure

The experimental procedure is based on the measurements of the rotor thrust provided by the test-bench. These measurements will be collected in situations where an element is located close to the rotor (from above, below or laterally, depending on the particular phenomenon under study, that is, ground effect, ceiling effect or wall effect as it is stated in Figure 2.7). The PWM input signal that governs the rotor speed will be the same in all tests, which, in turn, implies that the desired rotor thrust will

Figure 2.6: Test stand and multiple configurations.

also be the same. However, the measured rotor thrust will change according to the aerodynamic conditions. At the beginning of each experiment, the rotor will receive the constant PWM input during a period of time that guarantees a steady-state for the system. From this point on, the measurements registered by the load cell will be filtered conveniently to get the mean value of the measured rotor thrust. The final test result will be the mean value of the thrust and the distance to the element used to disturb the rotor airflow. Several tests are carried out for each distance under study. This makes it possible to obtain statistical characterisations like the standard deviations using an errorbar format.

In order to automatise the experimentation, the graphic user of Figure 2.8 interface was implemented in MATLAB. This interface collects details of the experiments, such as the number of repetitions, the distance to the obstacle, the % of thrust and time in steady state of each repetition, among other data related to the experimental setup to automate and classified each experiment. Additionally, it has been added an analysis mode to assess the measurements of the experiments once it is finished and to extract the information of interest. Thus, this is how the results are ensured to be done and analysed in an homogeneous way closing the experimental environment.

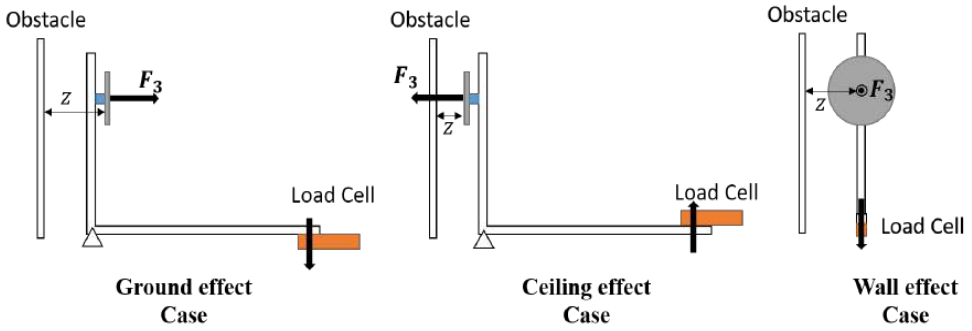

Figure 2.7: Cases of use of the test stand.

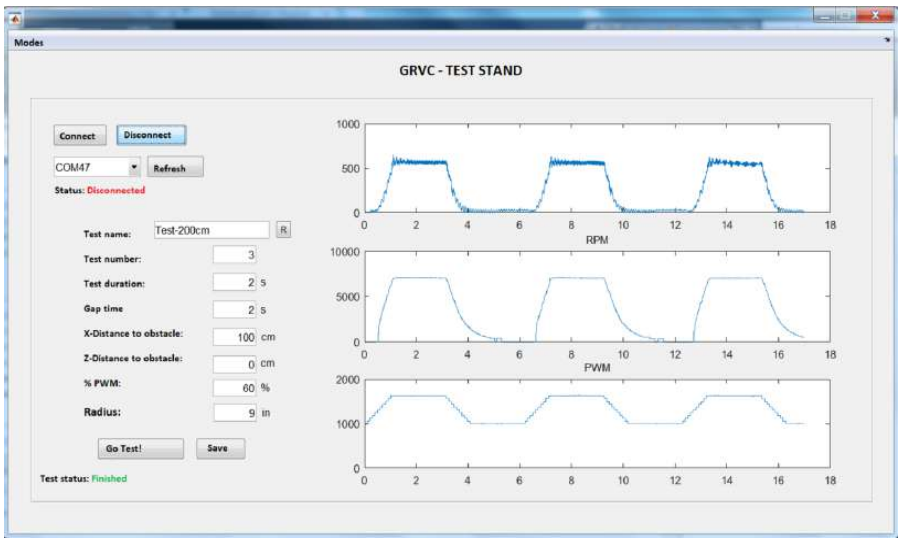

Figure 2.8: GUI implemented to the test stand.

2.5 Experimental modelling of aerodynamic effects - Results

There are many interesting experiments from the aerial manipulation point of view. The ground effect can appear when the manipulator grasps one object placed on the ground or over a step; the ceiling effect arises if the manipulator has to inspect or carry out based contact-tasks in structures like bridges; the wall effect flying close to pillars or even the effect of flying close to pipes could arise when flying in a chemical plan environment. This section collects different experiments and results related to the aerodynamic effect in aerial manipulator. In the case of the ground effect, it is also compared with the previously presented theoretical approach, the rest of the aerodynamic effects do not have a huge background in the literature, so they are analysed directly interpreting the experimental results.

2.5.1 Ground Effect in Multirotors

The ground effect appears in several conditions in which the aerial manipulation operation requires that the robot operate very close to a flat surface from the upperside, like the ground. For instance, ground effect arise during the take-off or the landing maneuvers or during the grasping operation either in hover or flying forward. Thus, although this effect is widely studied in helicopters and single rotors in general, the ground effect in multirotors can be significantly different due to the interaction of the airflow of the different rotors. Moreover, in aerial manipulator non-symmetrical situations can appear leading to the so-called "partial ground effect", introduced by the authors in [79]. This section tries to give an answer to how the performance of the aerial manipulator changes in these kinds of situations.

Ground effect for single rotor results

This section analyses the ground effect placing a single rotor in the test stand and moving the ground surface vertically along the z coordinate, as it is schemed in Figure 2.7. Figure 2.9 presents the experimental results obtained in these experiments of a

single rotor which has 16 inches of diameter size operating close to a ground surface and Table 2.1 presents the mean value and the standard deviation during the experiments which have been represented to assess the errors associated to the experiment with the test stand.

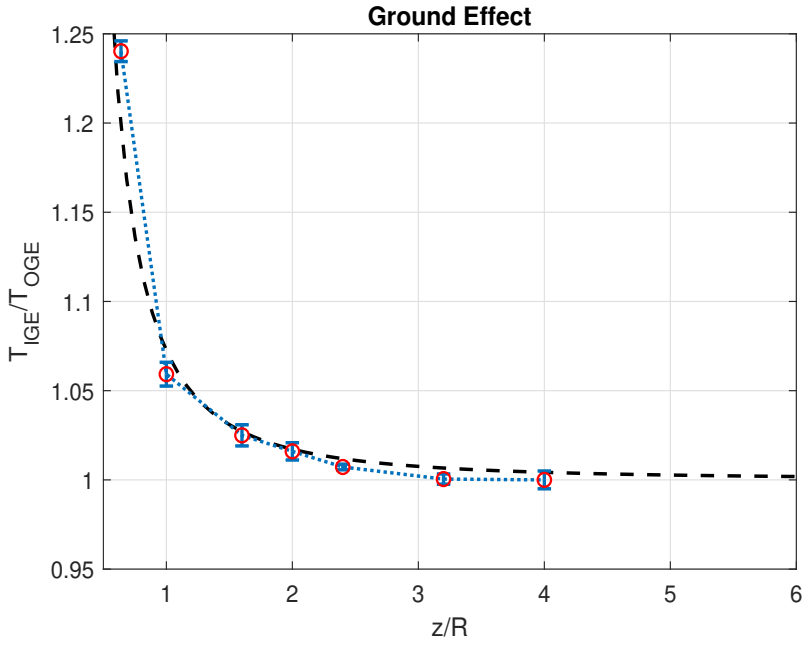

Figure 2.9: Ground effect in a single rotor. Thrust increment as a function of the normalized distance to the ground. Mean values and standard deviation (errorbar) in color, curve approximation in black.

Table 2.1: Standard deviation for single rotor in ground effect experiments

z/R	0.64	1	1.6	2	2.4	3.2	4
σ	0.0058	0.0067	0.0059	0.0048	0.0016	0.0029	0.0050

The results in Figure 2.9 show that the PFI model (the black line) that is used in helicopters for modeling the ground effect also well predicts the influence of the ground on the rotors of the multirotor, which are much smaller. This first results are very useful to validate the experimental procedure using the test stand, because in this

case, despite the size of the propeller, both problems are similar and then, the results are expected to address the theoretical curve because this is also non-dimensional.

A functional interpretation of the ground effect presented in the Figure 2.9 is that the ground "pushes the rotorcraft up" as the rotor approaches the surface. For the same transmitted power to the motor, the rotor develops more thrust caused only by the presence of the ground, which deviates the airflow radially and parallel to the ground generating new fields of velocity and pressure around the rotor. This also implies that flying close to the ground could be more efficient in terms of the energy which is consumed.

Ground Effect for the Full Multirotor

In this section, the state of the art was pushed forward carrying out an experiment with a complete multirotor in the test stand. The results are presented in Figure 2.10 which shows that the ground effect is significantly different from the predicted for a single rotor (the black dashed line). This is because in multirotors the presence of multiple coplanar rotors induces different behaviors with respect to the single rotor case, since the airflow from the different rotors may interfere with each other. In fact, the result significantly differs from the results of the PFI model generalised for a quadrotor presented in Section 2.3.2, pointed out that this model can not be generalised

The answer to these discrepancies can be found carrying out a conceptual CFD simulation. The interference of the different air flows developed by the rotors can be observed in the velocity field presented in Figure 2.11. This simulation of two rotors working close to the ground shows that the airflow in the middle of the space between the rotors is reverted after reaching the ground because the different flows collide in the middle point between them. This airflow could additionally hits the multirotor frame of the multirotor producing an extra force (see Figure 2.11).

Then, it is clear that the PFI model cannot approach the full multirotor ground effect because the assumptions of this theory do not take the reverted flow and its consequences into account. Thus, it is necessary to add an extra term associated to

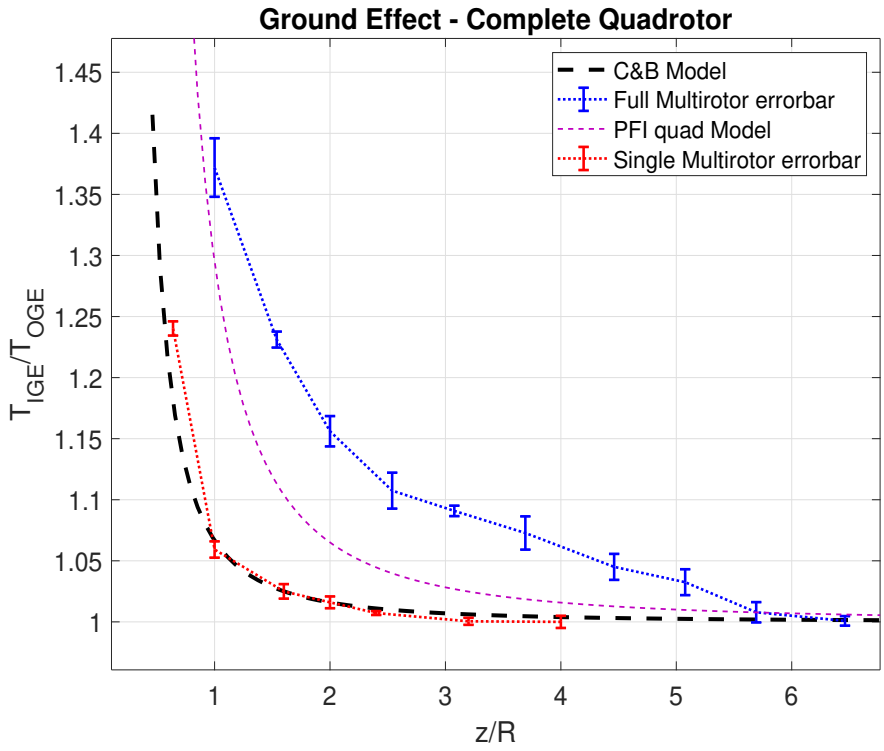

Figure 2.10: Ground effect in a full multirotor. Experimental and PFI comparison.

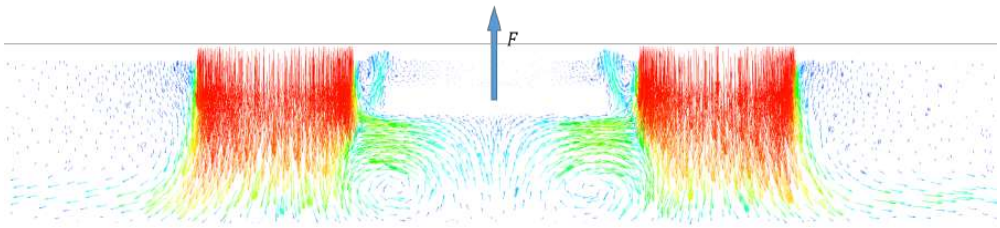

Figure 2.11: Conceptual CFD simulation of the velocity field approach for a multirotor flying close to the ground. Blue error bar represents the experimental results, magenta dashed line is the theoretical results using the generalisation of the PFI model, red error bar shows the experimental results obtained for a single rotor and black dashed line is the PFI theory for a single rotor

the force which arises due to the presence of the multirotor frame (see F in Figure 2.11).

The force, F has been modeled including an additional term in the equation provided by the PFI model. This additional term uses the velocity of the air at the central point of the body and adjusts its influence with an empirical coefficient Kb, which takes a value close to 2 in the experiments which are performed and it is strictly dependent on the geometry of the multirotor. Finally, superimposing this effect, due to the collision of the flow with the PFI model, for a complete multirotor the following expression can be obtained:

$$\frac{T_{IGE}}{T_{OGE}} = \frac{1}{1-(R/4z)^2-R^2(z/\sqrt{(d^2+4z^2)^3})-(R^2/2)(z/\sqrt{(2d^2+4z^2)^3})-2R^2(z/\sqrt{(b^2+4z^2)^3})K_b} \tag{2.17}$$

This last expression is presented in blue dashed line in Figure 2.12.

2.5.2 Ceiling Effect in Multirotors

In some emerging applications, aerial vehicles need to physically interact with the environment from the underside, as in bridge deck or beams inspections by contact operations. In those cases, the so-called "aerodynamic ceiling effect", introduced by the author in [78], will arise affecting the multirotor just like the ground effect does when multirotors work close to a surface from the upper side. This made it essential to study this problem in detail, which, furthermore, had not received much attention in literature.

Then, this section follows the same approach as the previous one, in which the effect of an isolated rotor is analysed and then, the same test is carried out with a complete multirotor to assess its behaviour.

Ceiling effect - Single rotor experiments

First of all, it is necessary to analyse the ceiling effect for a single rotor in order to get a first approach to the problem using the test stand presented in Section 2.4.1

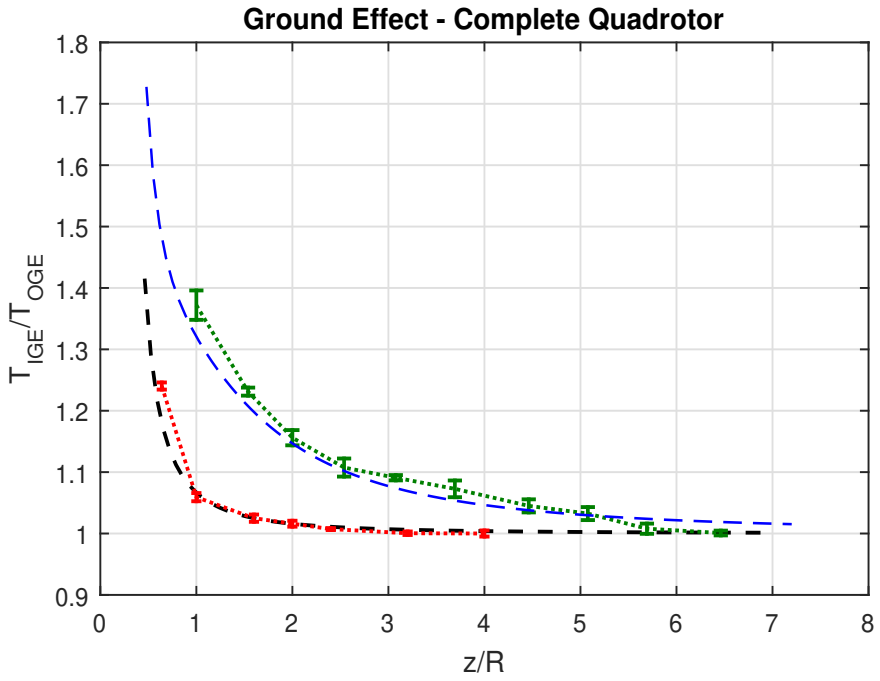

Figure 2.12: Ground effect in a full multirotor. Green errorbar is the experimental results for a full multirotor, blue dashed line shows the proposed PFI+Geometrical term model, red errorbar and black dashed line, represent, respectively, the experimental and theoretical results for a single rotor.

following the setup presented in Figure 2.7 for the ceiling effect. Next, the results obtained in these experiments are analyzed.

In this way, Figure 2.13 shows the results obtained in these ceiling effect experiments for the rotor thrust. T is the thrust generated by the rotor, z is the distance to the surface and R the radius of the rotor (in this case 9.4 inches with DJI 2312 rotor). The acronym "ICE" means "In Ceiling Effect" and "OCE" means "Out Ceiling Effect". The mean value and the standard deviation of the thrust for each normalised distance z/R are shown in Figure 2.13 and again represented in Table 2.2. The results clearly show that the thrust increases significantly when the rotor approaches the ceiling, i. e., when a multirotor is flying close to the ceiling, the thrust of the rotors will also increase and it will push the multirotor even closer to the ceiling. It is important to consider this effect in order to avoid a crash between the multirotor and the ceiling surface. Moreover, the effect is stronger than the ground effect.

In order to find an explanation of the abrupt increase in the thrust, the author looked into other data collected during the experiment. In this case, these data also show that the aerodynamic ceiling effect affects the rotational speed of the rotor significantly. Figure 2.14 shows the changes in the RPM as the rotor approaches the surface meanwhile the PWM signal commanded to the rotors remains constant. This is consistent with the large increase in thrust of the Figure 2.13 because the RPM appears squared in the classical thrust expression. Then, this increase of the RPM is produced by a vacuum effect which decreases the propeller drag when it is very close to the obstacle. Therefore, then the rotor can rotate faster generating this thrust increase joined to the one created due to the change of pressures around the propeller.

Table 2.2: Standard deviation for single rotor in ceiling effect experiments

z/R	0.20	0.40	0.80	1.20	1.60	2.00	2.40
σ	0.0031	0.0033	0.0037	0.0038	0.0037	0.0022	0.0020

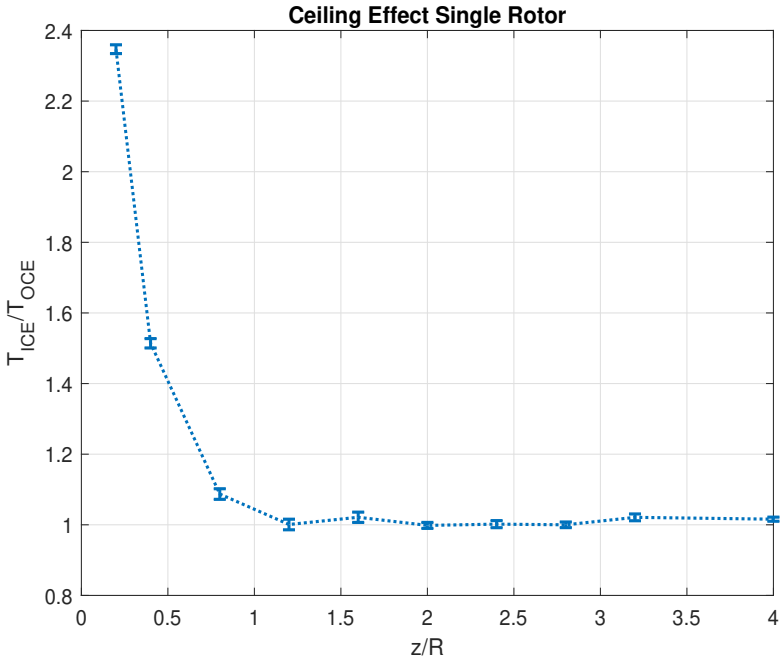

Figure 2.13: Experimental results of the ceiling effect in a single rotor. It shows that the thrust is increased when it works close to the ceiling.

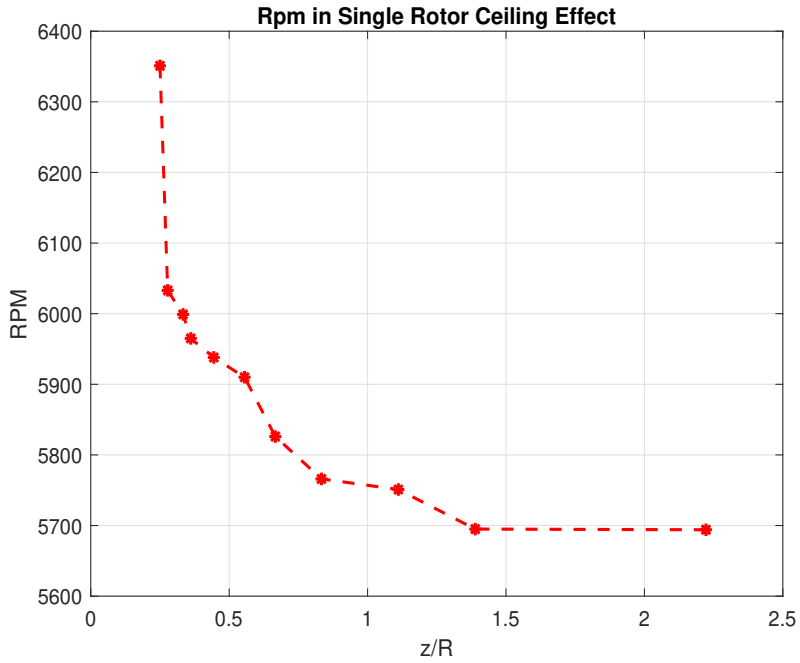

Figure 2.14: Changes in RPM for a single rotor working in ceiling effect conditions with the same PWM signal commanded. It shows how the ceiling effect produces a significant increment in the rotational speed.

Since this effect cannot be modeled using the PFI so a least squares minimum method has been used to fit the experimental curve as follows:

$$\frac{T_{ICE}}{T_{OCE}} = \frac{1}{1 - \frac{1}{K_1}(\frac{R}{z+K_2})^2} \tag{2.18}$$

Where the least squares minimum values obtained are $K_1 = 6.924$ and $K_2 = 0.03782(m)$. This is the black braked line represented in Figure 2.15.

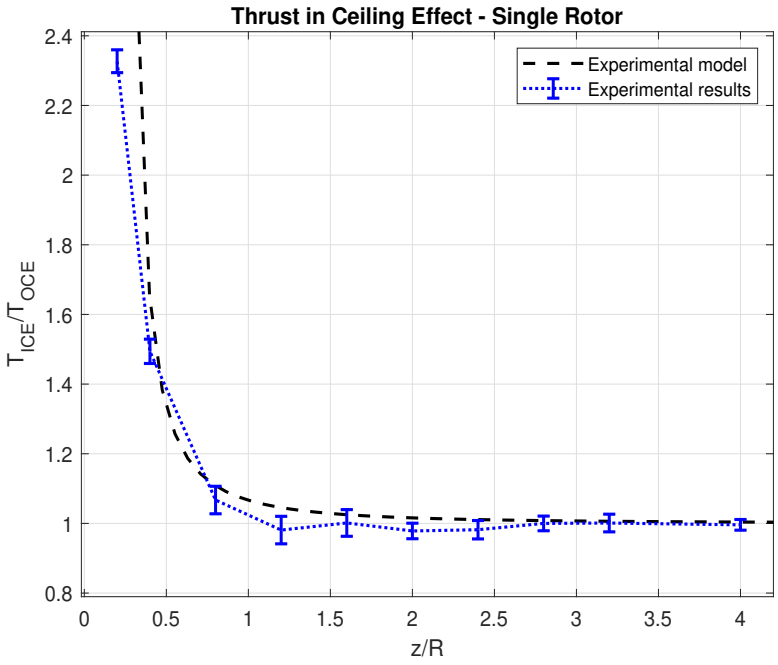

Figure 2.15: Ceiling effect in a single rotor. Experimental results and fitted model obtained using the least squares minimum

Ceiling effect - Full multirotor experiments

The same phenomenon which appears for a multirotor operating in ground effect appears when a multirotor is flying close to the ceiling. The flow field generated around each rotor is also affected by the other rotors and the multirotor frame. Thus,

the ceiling effect for a full multirotor produces a different effect than adding the effects of each individual rotor due to the coupling between the flow of the propellers.

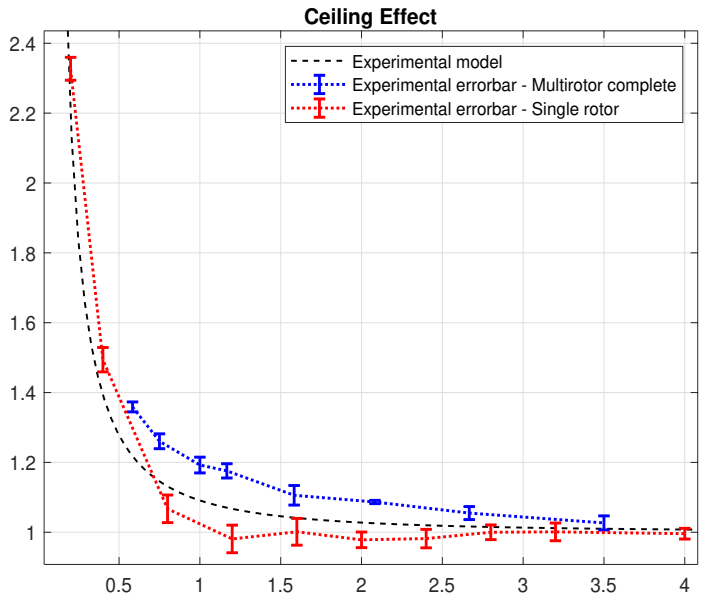

Figure 2.16: Comparison between the ceiling effect in a quadrotor (in blue errorbar) and a single rotor (in red errobar). Black dashed line is the experimental fitted model of 2.18

These results can be interpreted from different points of view. On the one hand, it is possible to develop more thrust for the same power if the multirotor is subjected to the aerodynamic ceiling effect. On the other hand, the multirotor can increase its maximum flight time because the rotor decreases its energy consumption. It is a great benefit which can be used in several UAV applications.

Moreover, researches like [78] which is also presented in the Chapter 4 of this thesis, shows how to take advantage of the ceiling effect designing a platform which can maintain a contact with the ceiling. This solution helps to minimise the two typical problems which appear in the applications of multirotors. Firstly, as it was mentioned above, the ceiling effect increases the maximum flight time and secondly, the ceiling

effect solves almost completely the problem of the stability during the operation and the motion-blur because the platform is stick to the ceiling during the application task and has constrained all the displacements. The last problem arises especially in high precision applications, such as aerial manipulation close to a surface, which generates aerodynamic effects or inspection by contact applications.

2.5.3 Wall effect

Since some of the typical applications require that the multirotor flies close to obstacles, like walls, for example, during the installation of a sensor in a vertical surface, this situation has also been studied. However, the classical assumptions in helicopter theory suggest that the airflow is almost perpendicular to the rotor plane. So, according to this hypothesis, the expected results in the wall effect experiment is that the wall has no influence on the rotor thrust.

After accomplishing those experiments, the results of Figure 2.17 were obtained. These clearly show that the wall effect is negligible because there is not a clear effect in rotor thrust when the rotor operates close to the wall. The changes obtained in Figure 2.17 are very light compared to the ground effect which increases the thrust almost 25% and the ceiling effect which increasez approximately 50-100% the rotor thrust. So, we can conclude that the wall effect is negligible.

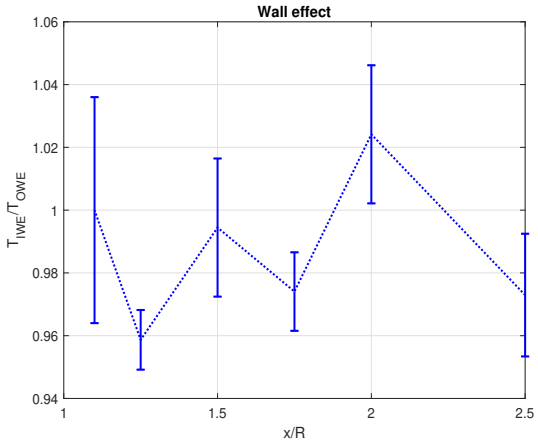

Figure 2.17: Wall effect results. The presence of the wall does not clearly disturb the rotor performance

2.5.4 Other effects

Following the structure of this section, a first approach to different aerodynamic effects which can appear in typical application scenarios are shown. However, in this case, the study is not as detailed as the previous one because, they are out of the scope of the main cases of use of the project in which this thesis was developed. Then, these cases of use are studied as a first approach and are treated as a future work in this research field. For example, in the case of the HYFLIERS project [34], which aim to carry out inspection and maintenance tasks in an industrial environment, like refineries or oil & gas industries, the multirotor should fly between tubes and pipes. So, in order to grant a good accuracy during the operation, it is necessary to model the effect of flying close to this kind of obstacles. Another interesting case to be studied is how this aerodynamic effect can affect the new fully-actuated platforms with tilted propellers. Finally, combined effects, like flying in corners or in fully closed environments are considered interesting for future applications.

Pipe effect

In this case, which will be better analysed in chapter 5, the aerodynamic effect does not only depend on the distance to the obstacle, but it also depends on the relation between the size of the rotor and the tube, and the transverse coordinate in which the rotor is placed. Figure 2.18 shows preliminary results of this effects.

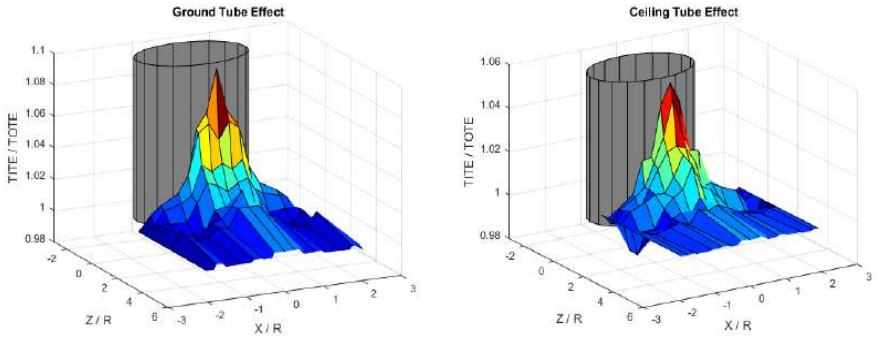

Figure 2.18: Ground tube effect (left) and ceiling tube effect (right) experimental results.It clearly shows that in this case, the model does not only depend on the vertical distance but also on the horizontal one. This will be explained in the 2D approach presented in the Chapter 5

Furthermore, it can be observed that this problem does not have revolution symmetry, so the thrust will depend on the position of the propeller with respect to the pipe and it will be as a function of time in Figure 2.19. However, this effect is very fast and it is produced at a high frequency being negligible for robotic manipulation tasks.

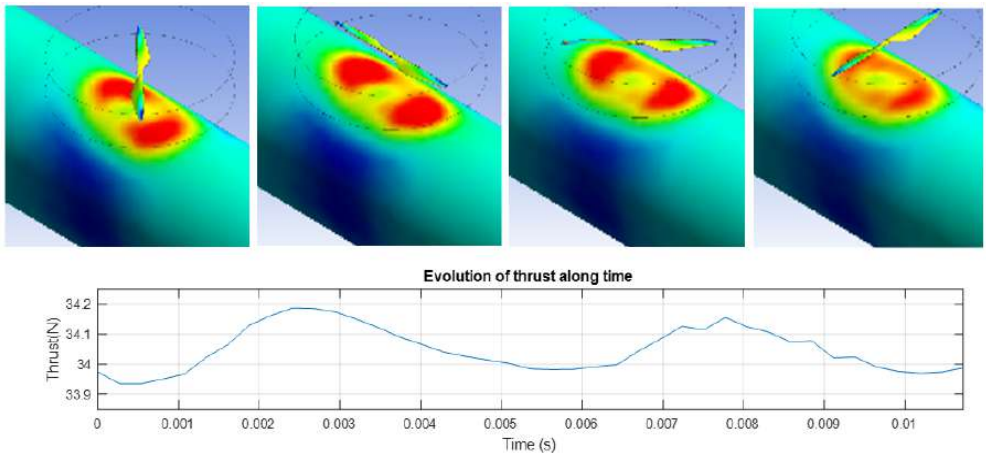

Figure 2.19: Evolution of the tube effect with respect to time when the rotor moves above a pipe. The effect of the pipe is not constant due to the problem does not have symmetry of revolution.

Tilted rotor

The effect that can arise in tilted rotors working close to a planar surface is relevant because, nowadays, the use of this kind of multirotors is growing exponentially. This kind of platforms is very interesting because they increase the performance of the aerial manipulator. As expected, the aerodynamic effect is also different because the rotor inclination produces a lower disturbance in the wake development, so the changes in the thrust are lower (see Figure 2.20).

Figure 2.20 shows the experimental results of how this effect changes in the case of the ground effect for a typical inclination of 10°.

An extra effect that could arise is that since this multirotor is not usually symmetrical [27], the ground effect could lead to generate forces also in the horizontal plane.

Ground + Wall effect

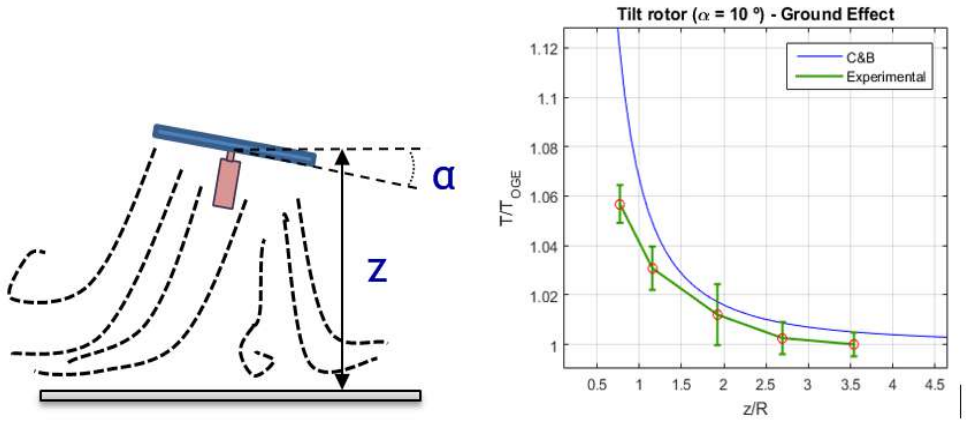

Figure 2.20: Simple scheme of a tilt rotor in ground effect (left) and experimental results (right). A tilting rotor is less disturbed by the ground because the rotor wake has more space to be developed.

The next question consists of evaluating the combined effect of ground and vertical wall effect. It is expected that the result can approximate the ground effect in tandem rotors because the wall acts as symmetry conditions except for the tangential velocity which is zero on the wall and not necessarily in a symmetry plane. The experimental results are shown in Figure 2.21 where the results "In Ground and Wall effect" have been called "IGWE" and the ones "Out Ground and Wall effect" have been named "OGWE". The value of d represents the distance between the center of the rotors and the wall.

The result shows how the thrust has a different trend in this case; for values of z/R 2 the thrust decreases with respect to the thrust out of effect, and the trend is reversed in values of z/R 1.2 where the thrust is greater than the thrust out of effect. This result can be explained with the fountain effect presented in [74]. In this distance, the fountain effect is greater than the ground effect. The fountain effect produces significant changes. The flow in the wall has the reverse direction to the main rotors. This flow disturbs the normal rotor operation. Then, the rotor efficiency decreases and produces a lower thrust. The reverse flow can be observed in the Figure 2.22. This CFD simulation intends to show how the flow flies. The impacts of the

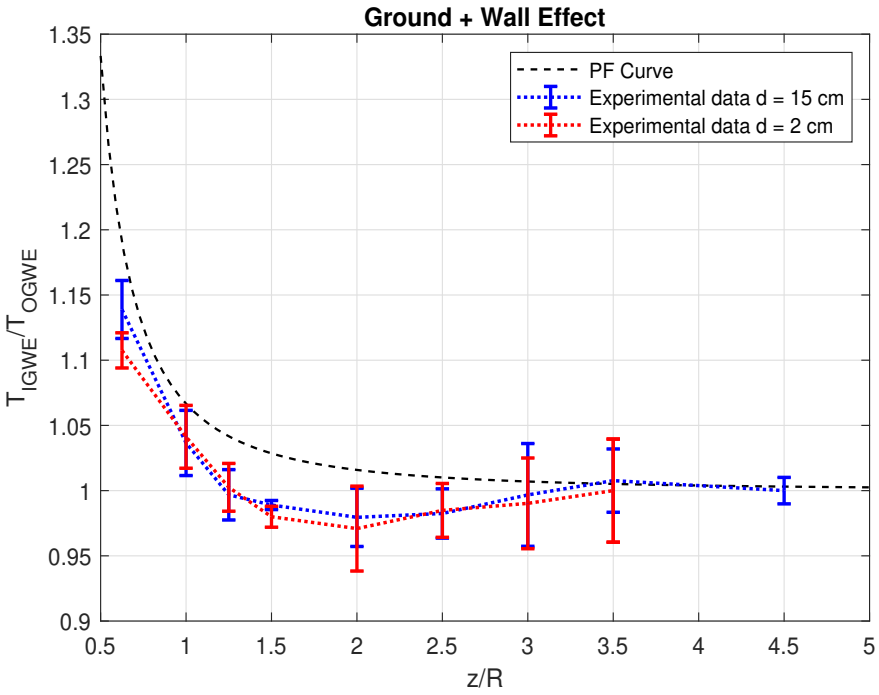

Figure 2.21: Ground and Vertical Wall Effect. Fountain effect arises due because the reverted flow that goes up along the wall affect to the rotor efficiency.

rotational flow and the flow disturbance in the rotor for reversed flow have not been considered. The approximation of the classical ground effect model is not valid in this case. We suggest studying this situation in detail by other methods, such as CFD.

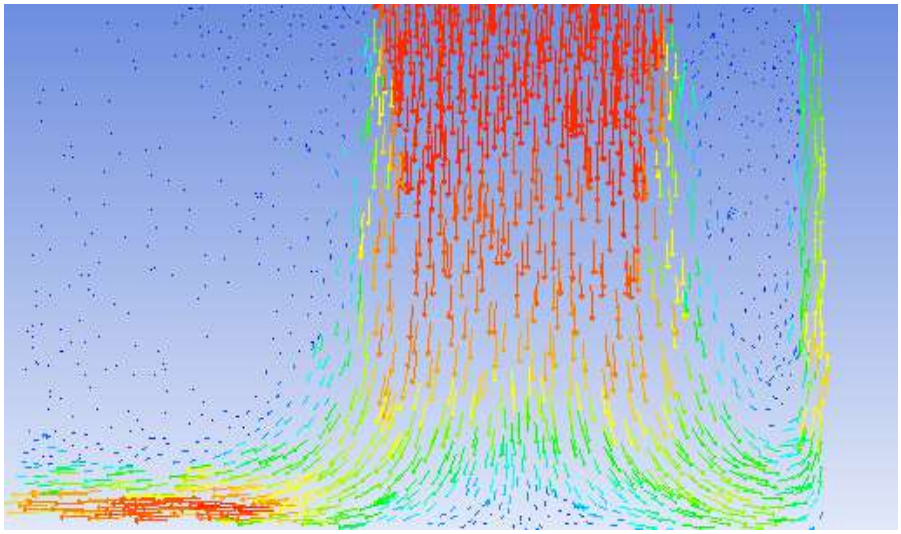

Figure 2.22: Ground + Vertical Wall Effect. CFD Approach to velocity field. This result clearly shows how the flow is reverted when reach the ground.

Ground Effect Tandem Rotor

These experiments have been done to assess the ground effect in a tandem rotor aircraft like the Boeing CH-47 Chinook or to asses the ground effect in multirotors that need to operate close to the ground but only with two rotors affected by the ground effect. It is expected that the results obtained are like those obtained for the "Ground + Wall Effect" effect for the reasons discussed in the section above. The experimental results are shown in figure 10. The trend and behaviour of the results are qualitatively the same as in the "Ground + Wall Effect".

Figure 2.23 represents the results of the classical model of the ground effect in black and the error bars are the experimental result of the ground effect of the tandem rotor in the test stand; the red error bar is with a distance between propeller tips of $2cm$

and in blue errorbar the distance is $15cm$. The experiments were done with a different distance between blade tips. Firstly, the thrust decreases reaching a minimum value in z/R 1.5, then it increases gradually overcoming the value out of effect.

The fountain effect is more significant in this case with respect to the "Ground + Wall Effect", and it is important in a wider range of z/R. This can be explained because the fountain effect is a harder constraint for two reasons. Firstly, in the middle of the tandem rotor, two flows are mixing and, secondly, there is not a wall, so the tangential velocity in the symmetry plane is not zero. Then, the influence in the efficiency is higher. Again the approximation of the classical ground effect model is not valid in this case and we suggest studying this situation in detail by other methods, such as CFD.

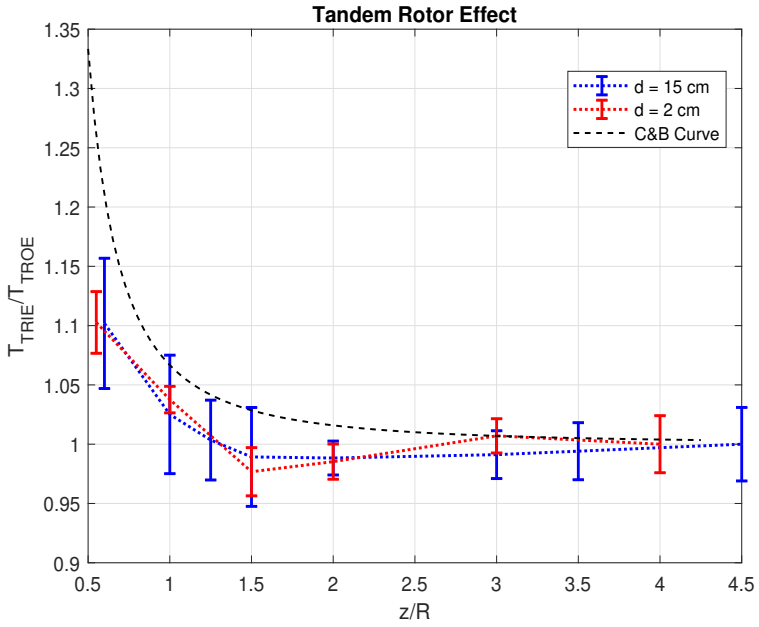

Figure 2.23: Tandem rotor in ground effect

2.6 Conclusions

At this point of the thesis, the reader should have a first approach of the aerodynamic effects that can arise in current aerial manipulation applications.

One of the most important conclusions is that the most significant aerodynamic effects presented along this chapter are also the most common ones in current applications. They are the ground and ceiling effects. In fact, the projects that involve the research of this thesis (AEROARMS [73] and AEROBI [33] projects) and their continuations (AERIAL-CORE [36] and RESIST [35] projects) present clear cases of the use of aerial robots which will be affected by this aerodynamic phenomenon.

On the one hand, in AEROARMS [73] and AERIAL-CORE [36] projects, it is possible to find the case of grasping objects and carrying out classical aerial manipulation operations in which the ground effect is suitable to arise. On the other hand, AEROBI [33] and RESIST [35] projects are about inspecting by contact operation in bridges, where the ceiling effect will be an strong constraint to guarantee safe conditions during the operation.

Then, the following chapters (Chapter 3 and 4) will study those effects in detail from a practical point of view. The idea is to solve these two different cases of use taking the basis presented in this one into consideration.

Chapter 3

Applications for aerial manipulation platforms

> A journey of a thousand miles
> begins with a single step.
>
> Lao Tzu

3.1 Introduction

This chapter analyses the influence of flying close to surfaces on multirotor control. It also presents the partial ground effect which is a special phenomenon that only appears in multirotors when flying close to surfaces and it can be defined as situations in which only some of the rotors (but not all) are under the ground effect. Along this chapter, the control of the partial ground effect is studied in detail because it is the most related one to the practice of aerial manipulation. The chapter uses the previous results of the ground effect in Section 2.5.1 and it includes a comparative study of the results obtained in simulation tests of different control strategies of a quadrotor model under the ground effect in two different scenarios.

The content of this chapter is based on the following publication:

- Pedro J. Sanchez-Cuevas, G. Heredia, and A. Ollero, Characterization of the Aerodynamic Ground Effect and Its Influence in Multirotor Control. International Journal of Aerospace Engineering, vol. 2017, 2017.

- Pedro J. Sanchez-Cuevas, Guillermo Heredia, and Anibal Ollero. Experimental approach to the aerodynamic effects produced in multirotors flying close to obstacles. In Iberian Robotics Conference, pages 742-752. Springer, 2017.

3.2 Problem Statement

Aerial manipulation applications usually require that the multirotor approaches different obstacles to grasp or manipulate something. However, this approaching maneuvers could place the multirotor in asymmetrical conditions with respect to the ground, giving place to a new phenomenon called partial ground effect, which is unique to multirotors, and which comes from the way the rotor thrust forces vary with the distance to the ground.

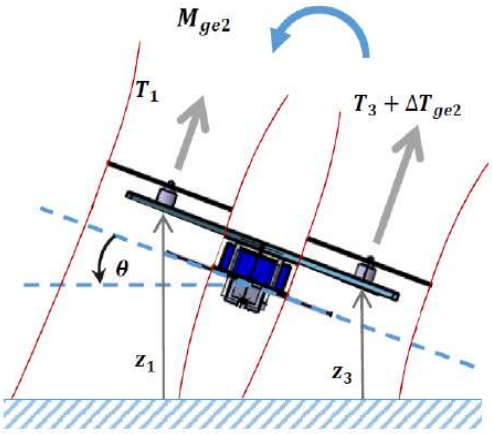

Figure 3.1: Partial ground effect close to the ground.

Since the increment in rotor thrust depends on the distance of each rotor to the ground and each rotor has a different distance (z_1 and z_3) a disturbance moment

M_{ge2} will be generated that tries to rotate the multirotor opposing the disturbance, and thus, it is a stabilizing moment. In practice, however, it has been found that for typical attitude disturbances of about $5 - 10°$ this effect, although stabilising, is negligible unless the multirotor is very close to the ground, and then it is considered not significant for a controller development.

This effect is illustrated in Figure 3.1 and Figure 3.2. The first one shows a multirotor hovering in ground effect that experiments an attitude perturbation. Since the increment in the rotor thrust depends on the distance of each rotor to the ground and these distances are different, a disturbance moment M_{ge2} will arise trying to rotate the multirotor opposing the disturbance, and, thus, this is a stabilising moment. In the second one, the aerial manipulation application, (grasping an object placed over a rectangular obstacle) the multirotor is flying in hover or at low speed in a situation in which only one or several of its rotors (but not all) are under the influence of the ground effect. It can be observed that rotor 3 experiments an increase in the thrust ΔT_{ge1} that will generate a disturbing moment M_{ge1}, which tries to rotate the multirotor counter clockwise, and then moves apart from the object because of the tilting.

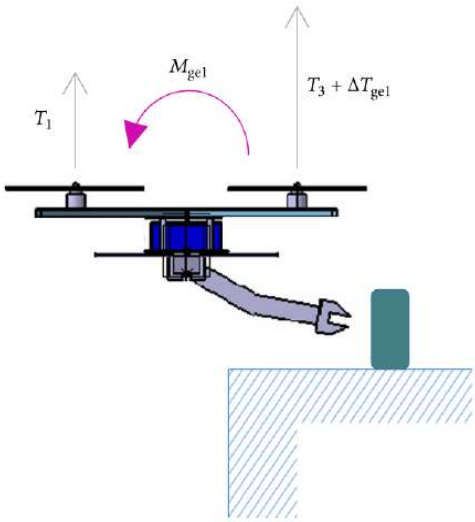

Figure 3.2: Partial ground effect in a typical aerial manipulation application.

In this case, it is clear to derive that if one of the rotors is under the ground effect, its characterisation can be modeled as described in Section 2.5.1 and using the previously presented PFI model in Section 2.3. However, the cases where three of the rotors or complete multirotors are close to a horizontal surface under the ground effect will be different due to the coupling between the airflow of the rotors and the geometry of the multirotor. In this case, the used multirotor is the same as that which was previously studied in Chapter 2. Then, previous results will be used to take the results of this aerodynamic disturbance in the multirotor controller into consideration.

3.3 Multirotor dynamic model

In this case, the dynamic model of the multirotor has been obtained using the Euler-Lagrange formulation [91] [88]. This model is basically obtained by considering the multirotor as a rigid body evolving in a 3D space and subject to one force (the total thrust generated by the rotors) and three moments generated by the differences in speed and thrust of the pairs of rotors. The dynamics of the electric motors are relatively fast and, therefore, they will be neglected as well as the flexibility of the blades. The generalised coordinates of the multirotor can be defined as:

$$\boldsymbol{q} = [\boldsymbol{p} \quad \boldsymbol{\eta} \quad \boldsymbol{\gamma}]^T \tag{3.1}$$

Assuming that the multirotor does not have articulated joints, $\boldsymbol{\gamma} = \mathbf{0}$, we define $\boldsymbol{p} = [x \quad y \quad z]^T$ to denote the position of the center of mass of the multirotor relative to the inertial frame and $\boldsymbol{\eta} = [\phi \quad \theta \quad \psi]^T$ to represent the three Euler angles (roll, pitch, and yaw) which are the orientation of a reference system attached to the multirotor body with respect to the inertial frame. If m is the total mass of the multirotor and $\boldsymbol{J}$ is the matrix of moments of inertia of the aerial vehicle in the inertial frame, the resultant Euler-Lagrange equations for the translations and rotational degrees of freedom are, respectively,

$$m\ddot{\boldsymbol{p}} + \begin{bmatrix} 0 \\ 0 \\ mg \end{bmatrix} = \boldsymbol{R}\boldsymbol{F_p} \tag{3.2}$$

$$\boldsymbol{J}\ddot{\boldsymbol{\eta}} + \boldsymbol{C_1}(\boldsymbol{\eta}, \dot{\boldsymbol{\eta}})\dot{\boldsymbol{\eta}} = \boldsymbol{\tau_\eta} \tag{3.3}$$

In 3.3, $C_1(\eta, \dot{\eta})$ is known as the Coriolis terms and it contains the gyroscopic and centrifugal effects; R is the rotation matrix between the body and inertial systems, and $\boldsymbol{F_p} = [0 \quad 0 \quad T]^T$ and $\boldsymbol{\tau_\eta} = (\tau_\phi, \tau_\theta, \tau_\psi)$ are the forces and torques generated by the rotors. Both translation and rotational dynamic equations can be expressed in a matrix form as:

$$\boldsymbol{M}(\boldsymbol{\xi})\ddot{\boldsymbol{\xi}} + \boldsymbol{C}(\boldsymbol{\xi}, \dot{\boldsymbol{\xi}})\dot{\boldsymbol{\xi}} + \boldsymbol{G}(\boldsymbol{\xi}) = \mathfrak{F}(\xi) + \mathfrak{F}_{\mathfrak{E}} \tag{3.4}$$

where $\mathfrak{F}(\xi)$ are the generalised torques and forces, $\mathfrak{F}_{\mathfrak{E}}$ are the unknown forces (wind, turbulence...) and $\boldsymbol{M}$, $\boldsymbol{C}$ and $\boldsymbol{G}$ are the mass, Coriolis and gravity matrices respectively. Traditionally, the thrust generated by each rotor and the reaction torque due to rotor drag are generally accepted to be proportional to the square of the angular velocity of the rotor ω_i when flying on free air (Section 1.1.1):

$$T_i = C_T \Omega_i^2 \tag{3.5}$$

$$Q_i = C_d \Omega_i^2 \tag{3.6}$$

The thrust and drag coefficients C_T and C_T can be determined by static thrust tests. Then, for a quadrotor in which the distance of the geometric center to the axis of each rotor is d, there is a direct correspondence between the four generalised moments and the angular velocities of the rotors:

$$\begin{bmatrix} T \\ \tau_\phi \\ \tau_\theta \\ \tau_\psi \end{bmatrix} = \begin{bmatrix} C_T & C_T & C_T & C_T \\ 0 & C_T d & 0 & -C_T d \\ -C_T d & 0 & C_T d & 0 \\ -C_T & C_T & -C_T & C_T \end{bmatrix} = \begin{bmatrix} \Omega_1^2 \\ \Omega_2^2 \\ \Omega_3^2 \\ \Omega_4^2 \end{bmatrix} \tag{3.7}$$

However, when the multirotor is flying close to the ground or other horizontal surfaces the rotor thrust (3.5) and drag model (3.6) are no longer valid. To account for the ground effect and partial ground effects in the simulator the thrust model is modified as:

$$T_i = C_T \Omega_i^2 f_{GE}(z_{r,i}) \tag{3.8}$$

where $f_{GE}(z_r)$ is the ground effect factor that accounts for the increment in thrust due to the ground effect and partial ground effect, which are obtained from the data in Section 2.5.1. This ground effect factor $f_{GE}(z_r)$ depends on the relative distance of each rotor to the ground, z_r. Furthermore, in the simulator it was also considered that the rotor thrust increment varies approximately linearly with the rotor area that is under the ground effect, as it has been reported with experiments with a helicopter rotor [92].

3.4 Simulation results

3.4.1 Cases of study

Two different cases have been tested in order to analyse the influence of the ground effect in multirotor control and to compare the different control approaches:

- The multirotor flies over an obstacle (see Figure 3.3.a), beginning in point A and ending in point B. In the reference trajectory the y-coordinate remains constant, and the x-coordinate varies from x=0 (point A) to x=7 (point B). The obstacle is between x=3 and x=5.
- multirotor is commanded to go from point A to point B and hover on B, where it has to perform a manipulation operation (see Figure 3.3.b). In point B only one rotor is over the obstacle, and then, under the influence of the partial ground effect. In the reference trajectory, the y-coordinate remains constant, and the x-coordinate varies from x=0 (point A) to x=2.8 (point B). The obstacle is between x=3 and x=5.

Three different control alternatives have been analysed in both scenarios: conventional control with cascaded linear controllers, estimated torque controller and control with rotor height estimation (feed-forward). The results obtained using the different control alternatives are shown below. A comparison between these alternatives will be shown at the end of this section.

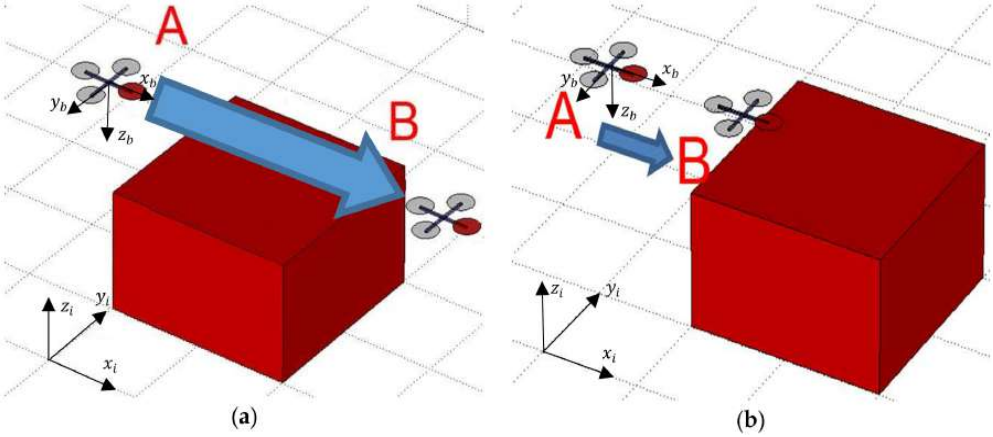

Figure 3.3: (a) Case 1: flying over an obstacle under the influence of the ground effect. (b) Case 2: hovering at a point with only one rotor under the influence of ground effect.

3.4.2 Conventional Control

A standard control scheme with cascaded PID linear controllers in each channel has been considered to analyse the response of the system to a conventional controller which does not take the ground effect into account. This control scheme is widely used as a baseline in commercial autopilots, and it is a good reference for the comparison with other methods. The multirotor is moving forward along the x global axis and the yaw angle is maintained constant in the simulations, and so the relevant variables which are presented in the plots as a function of the time are the pitch angle, θ, and the global coordinate in the direction of motion, x.

The results obtained in the simulation using the PID controller in the two experiments are shown in Figure 3.4 (Case 1-Flying over obstacle) and Figure 3.5 (Case

2-Hovering in partial ground effect). In the figures, a dashed line has been included to mark the x-coordinate of the final destination of the multirotor (point B in both cases). Furthermore, the values of the x coordinates that are over the obstacle are highlighted with a green background. Several simulations are presented in each plot for comparison: "OGE",which is the simulation of the multirotor flying high above the obstacle, so that no ground effect is present; and two simulations flying close to the obstacle ("IGE") at two different heights normalised with the rotor radius R.

Figure 3.4 shows the evolution of the x-coordinate and the pitch angle for the first case flying over an obstacle. It can be observed that the ground effect disturbance produces a torque which affects the system in attitude and position. This torque is more significant when the vehicle is closer to the obstacle. In fact, the results for $z/R = 2$ show how this torque pushed the vehicle away from the obstacle repeatedly and it cannot fly over it with this controller.

In the second case (Figure 3.5), the multirotor tries to hover with only one rotor over the obstacle, but it is unable to do it in the x-reference, and it stays flying in a maintained oscillation going in and out of the ground effect.

The simulations presented in Figure 3.4 and Figure 3.5 were performed with the quadrotor flying at a velocity of 0.2 m/s. In order to assess the behavior at different translation velocities, the simulations have been done at a maximum speed of 1 m/s. Figure 3.6.b shows the results of the hovering in a partial ground effect test case, and it can be seen that the behavior is similar to the one presented in Figure 3.4. Figure 3.6.a simulation of case 2, flying over an obstacle. In this case, although there is a strong perturbation in the pitch angle, the inertia of the multirotor moving at 1m/s allows it to surpass the obstacle unlike when flying at $0.2m/s$. Since moving at a slow speed is more restrictive and it is also more appropriate for aerial manipulation tasks, the rest of the simulations will be done with the multirotor flying at $0.2m/s$.

Other simulations have been done considering sensor noise. Figure 3.7 shows the simulation of the quadrotor in case 1, hovering in partial ground effect at a velocity of $1m/s$ and $z/R = 2$. A normal distribution with a standard deviation of 0.015 rad/s has been supposed for the noise in the gyroscopes. It can be seen in Figure 3.7 that the presence of noise in the sensors amplifies the oscillations, although the qualitative

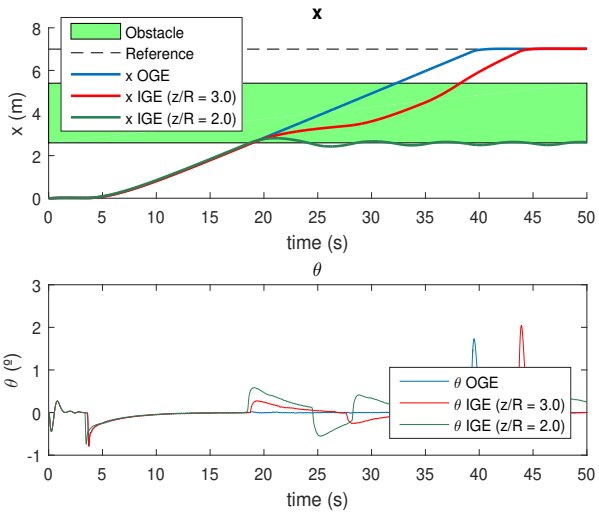

Figure 3.4: PID controller: Flying over obstacle. Red line shows how the ground effect decreases the speed of the multirotor when it approaches to the obstacle. Green line shows how with a linear controller the multirotor is not able to overcome the obstacle if it is flying very close to it

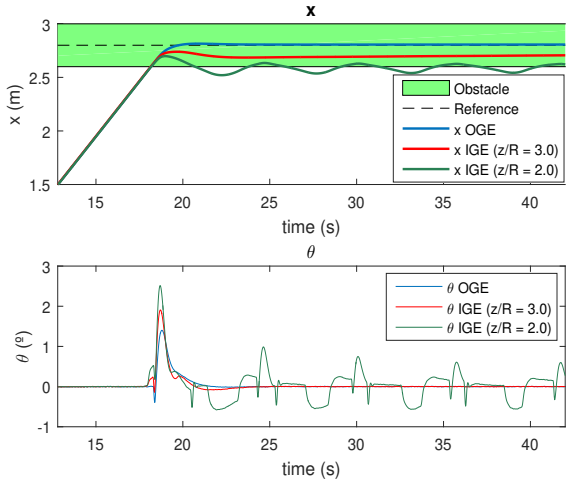

Figure 3.5: PID controller: Hovering in partial ground effect. In red and green, the controller is not able to achieve the references due to the ground effect. Actually, green line shows how the multirotor maintains oscillating trying to overcome the obstacle without success

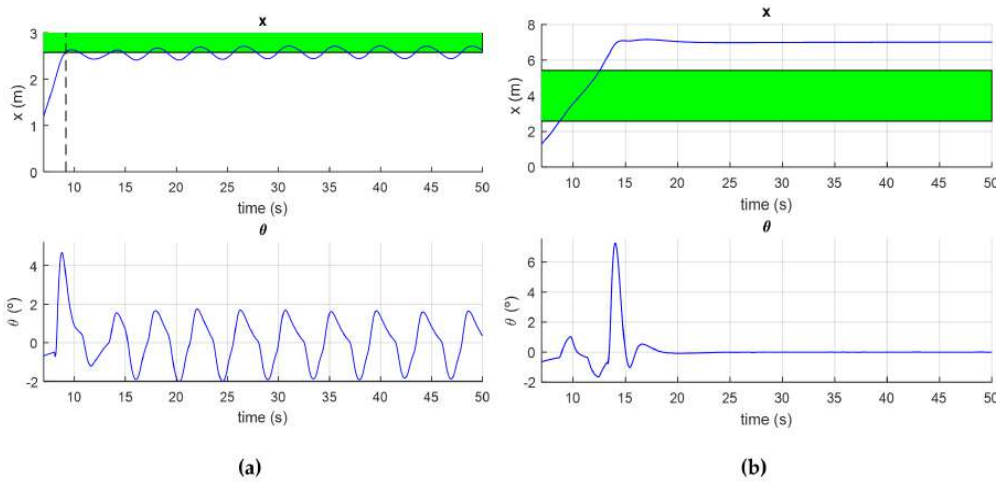

Figure 3.6: PID controller, velocity of 1 m/s and z/R = 2. Hovering in partial ground effect. In this simulation, the robot is commanded to fly faster to avoid the ground effect thanks to the inertia. Although in b) the result is better, in a) the robot oscillates without reaching the reference.

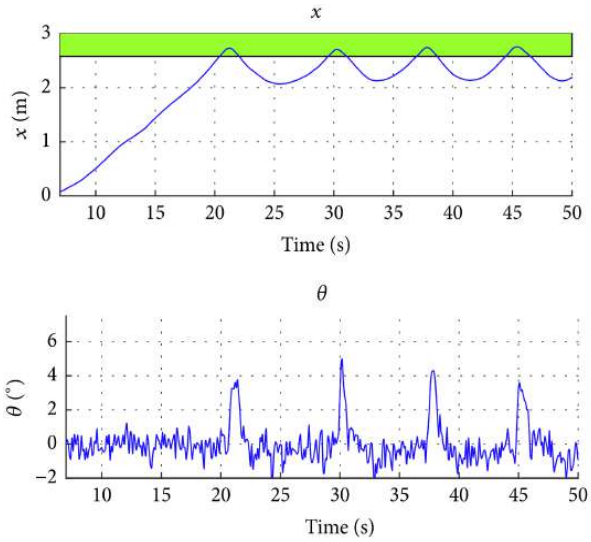

Figure 3.7: PID controller - Hovering in partial ground effect. Simulation with sensor noise shows that oscillations are worse in a realistic scenario.

behavior is similar. In the rest of simulations only the noise-free simulations will be presented.

3.4.3 Estimated Torque Controller

This control alternative includes a torque disturbance observer that is used to estimate the torque induced by the partial ground effect, caused by the different aerodynamic thrust generated by the rotors when the multirotor is in partial ground effect. Several approaches have been used to estimate external force and torque disturbances in multirotors [60] [61][93]. In this Section, a nonlinear torque disturbance observer has been implemented [62]. If the multirotor dynamic equations are expressed in compact form (9), the nonlinear observer is able to estimate the forces and torques due to the ground effect, $\mathfrak{F}_{\mathfrak{GE}}$:

$$\dot{\hat{F}}_{GE} = L(\xi,\dot{\xi})(F_{GE} - \hat{F}_{GE}) = -L(\xi,\dot{\xi})(M(\xi)\ddot{\xi} + C(\xi,\dot{\xi})\dot{\xi} + G(\xi) - F) \tag{3.9}$$

where $\hat{F}_{GE}$ is the vector of estimated force and torque disturbances due to the ground effect and $L(\xi, \dot{\xi})$ is the observer matrix that has to be designed in order to assure convergence of the observer. Figure 3.8 shows the control scheme of this strategy.

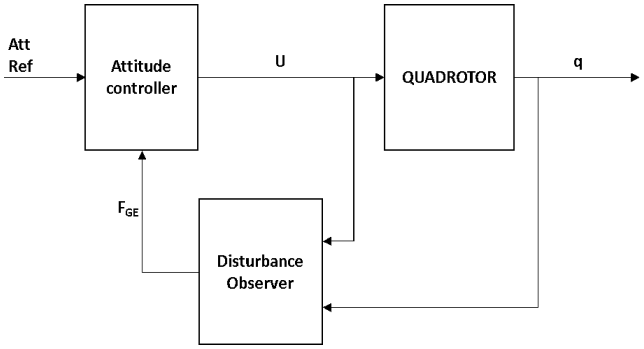

Figure 3.8: Estimated torque controller.

The results obtained with this control approach are shown in Figure 3.9 (Flying over an obstacle) and Figure 3.10 (Hovering on partial ground effect). In these figures, it can be observed that the obtained results are better than using a conventional PID-based controller, as it was expected.

In the first test case (as defined in Figure 3.3), the response of the system is faster than that with the baseline controller. Moreover, the multirotor is able to avoid being pushed away from the obstacle when $z/R = 3.0$, and it is able to arrive at its destination, at point B ($x = 7$) when it is flying closer to the obstacle at $z/R = 2.0$.

The results of simulations in the second case (Figure 3.10) show that this control alternative can eliminate the aggressive oscillations in pitch angle. The estimated torque controller can improve the response of the system because the disturbances are partially cancelled at the same time they are being produced.

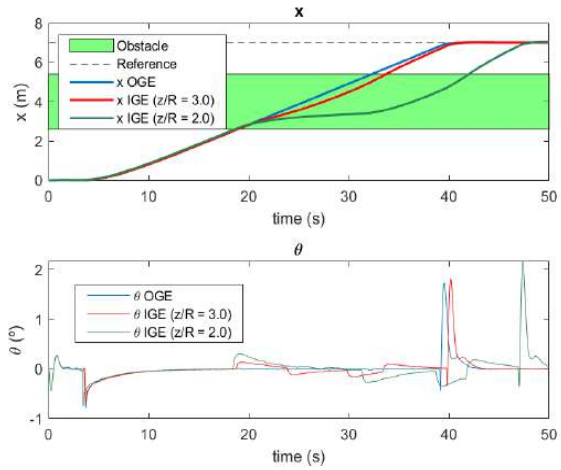

Figure 3.9: Estimated torque controller: Flying over obstacle. The estimated torque controller improves the results compared with the linear controller, however, when the robot is very close to the obstacle (green line) the disturbance is again significant.

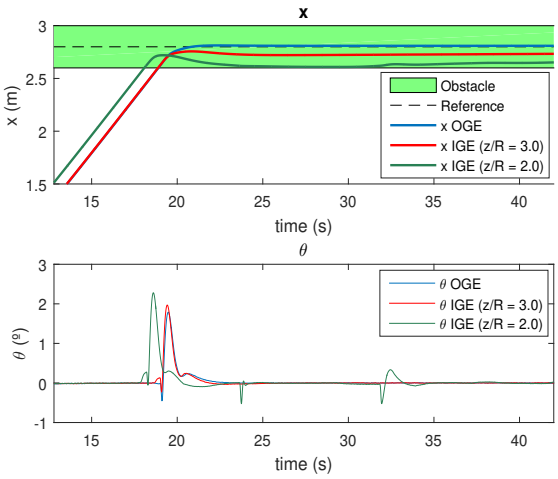

Figure 3.10: Estimated torque controller: Hovering in partial ground effect. The estimated torque controller improves the results compared with the linear controller, however, when the robot is very close to the obstacle (green line) the steady state error is important.

3.4.4 Control with Rotor Height Estimation (Feed-forward)

The last alternative that was studied is based on a feed-forward concept. As it has been seen in the previous sections, the ground effect torque disturbance is directly related to the relative distance from the rotor to the ground or to the obstacle. Then, if we can have an estimation of this relative distance, it is possible to implement a feed-forward control approach that allows canceling the torque disturbance partially. The block diagram of this approach is represented in Figure 3.11.

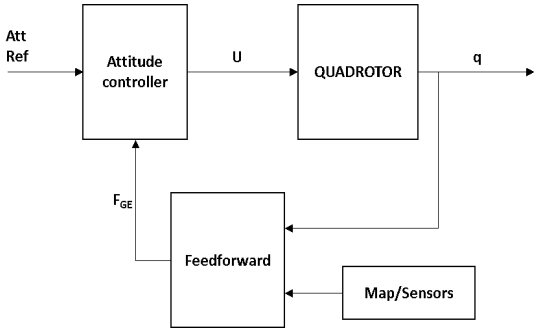

Figure 3.11: Control scheme of feed-forward controller.

The results obtained in the simulation with the feed-forward controller in the two experiments are shown in Figure 3.12 and Figure 3.13. As can be seen in both Figures, the results are better than the obtained ones with the other control alternatives. This is because the torque disturbances can be anticipated, and the multirotor controller can compensate them largely.

It is important to mention that this strategy depends largely on the availability of an accurate environment map and precise relative positioning with respect to the map. These errors can come from the estimation of the multirotor relative height with respect to the terrain (z-error), although, available sensors (i.e. laser altimeter or ultrasound range sensor) allow a relatively accurate height estimation and their effect will be a deviation of the predicted thrust increase from the real one. Offset errors in the horizontal plane are more common since precise UAV positioning outdoors is still a difficult task (small UAVs usually do not have cm-level DGPS RTK receivers), and the effect of these errors is the prediction of a thrust increase when it does not exist.

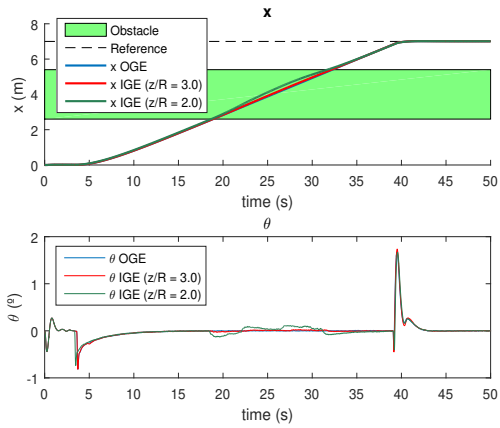

Figure 3.12: Feed-forward controller: Flying over obstacle. Feed-forward controller is able to reach the reference and compensate the aerodynamic disturbance even in the closest case (green line)

Different cases have been tested in simulation. Figure 3.14 shows the results when the map has an x-offset error, which can be compared to the results of Figure 3.13 (map without an offset error). This offset error produces that the multirotor controller anticipates a thrust increase which does not exist yet, generating oscillations and instability. If the map has small errors, the controller will present an overshoot but, it still will be able to guide the UAV, as it is shown in the simulation in the left result of Figure 3.14 (with an x-offset error of 5 cm added to the map). If the errors are larger, the oscillations can grow to instability, as shown in the right plot of Figure 3.14, where the offset error added to the map is 15 cm long. In this case, the performance is even worse than using the standard PID control scheme (see Figure 3.5).

In practice, a sensor-based approach could be convenient to implement this type of controller, estimating the relative distance of the rotors to the surfaces of the environment in real time. One possibility is to use a sensor below each rotor that is able to measure the relative height, such as ultrasonic or laser range sensors. Another option is to use exteroceptive sensors (laser, cameras) to build a map of the environment in real time, and to use this map to anticipate torque disturbances.

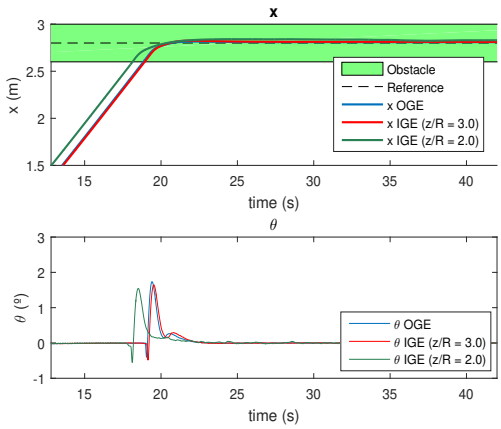

Figure 3.13: Feed-forward controller: Hovering in partial ground effect. Feed-forward controller is able to reach the reference and compensate the aerodynamic disturbance even in the closest case (green line)

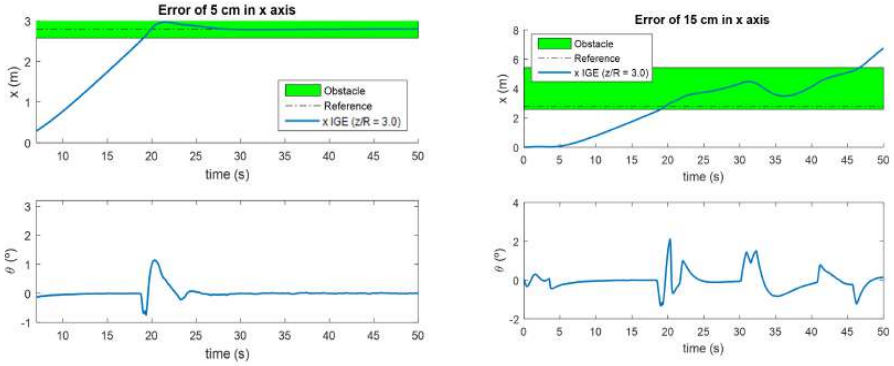

Figure 3.14: Simulation of feed-forward controller using maps with offset errors: left - 5 cm error. right - 15 cm error. It shows how an error in the estimation of the aerodynamic disturbance can lead to the instability.

3.4.5 Comparison between different control alternatives

Figure 3.15 (Flying over obstacle) and Figure 3.16 (Hovering in partial ground effect) presents a comparison of the simulations between the different multirotor controllers, flying at a relative distance of $z/R = 2.0$ from the obstacle.

From the results in Figure 3.15 and Figure 3.16, it can be seen that the conventional PID-based controller that is implemented in many multirotors does not give acceptable results when flying close to obstacles or the ground, causing oscillations that may lead to dangerous situations, or even preventing the multirotor from reaching its destination because it gets trapped in a cycle at the beginning of the obstacle.

With a detailed environment map the feed-forward controller will give better results, provided that the practical implementation issues are correctly addressed.

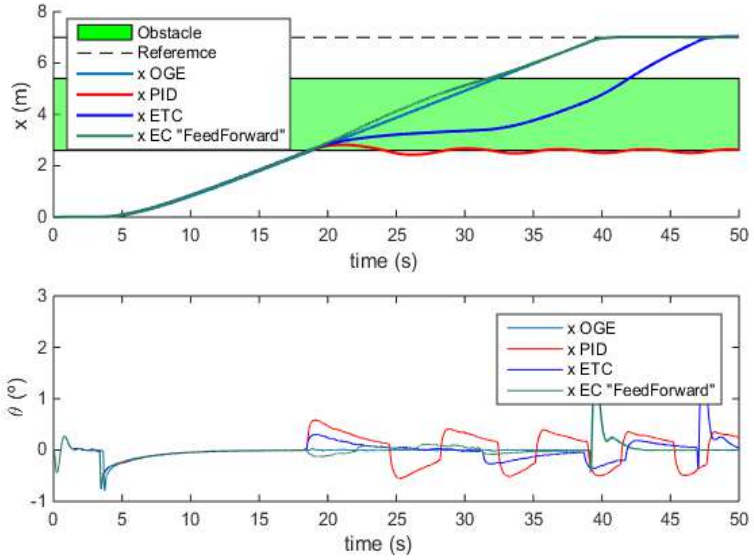

Figure 3.15: Flying over obstacle -Comparison of controllers.

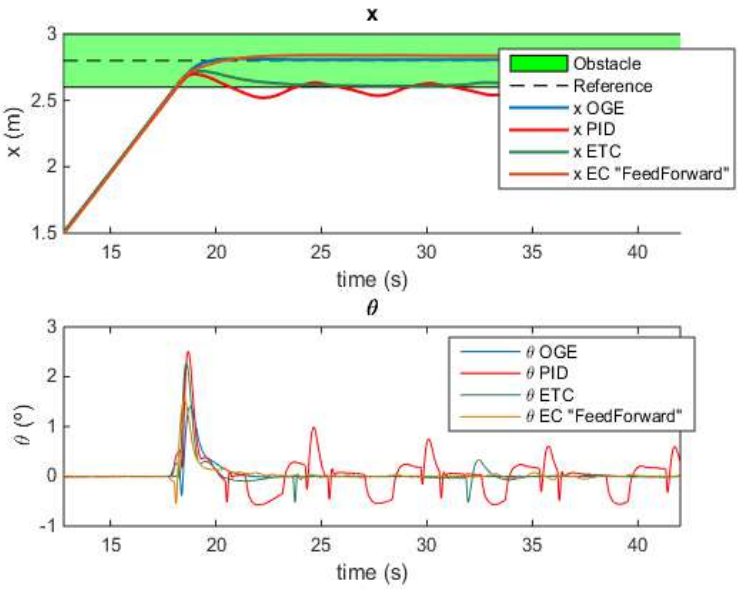

Figure 3.16: Hovering in partial ground effect -Comparison of controllers.

3.5 Experimental Results

Several experiments have been conducted to experimentally assess the performance when the multirotor flies over an obstacle. A first set of experiments were conducted in a test-bench in which the multirotor is allowed to rotate freely around one of the axes (pitch angle) (Figure 3.17.a). The ground effect is introduced placing a large plate under one of the rotors at different distances (Figure 3.17.b), while the multirotor pitch angle is controlled by the cascaded PID controller.

Figure 3.18 shows the results of the experiment, placing the ground plate at $z/R = 2$ with both the PQUAD multirotor and the AMUSE aerial manipulator. The evolution of the pitch angle for both cases is presented in Figure 3.18 marking with green background when the ground plate is placed below one of the rotors. It can be seen that when the (partial) ground effect is present, the torque disturbance induces an increase in the pitch angle that is difficult to correct by the PID controller.

Figure 3.17: Experimental tests with multirotors in the testbench: a) the PQUAD, b) the PQUAD with a ground plane

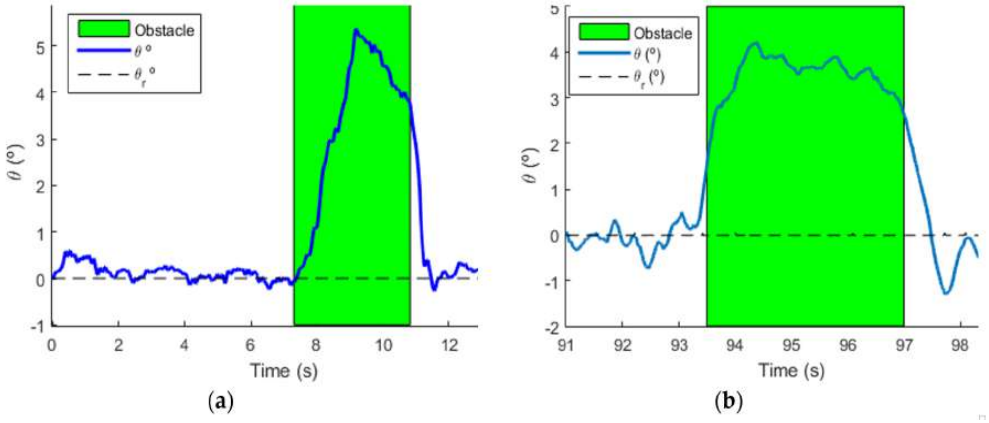

Figure 3.18: Experiments in the testbench, influence on the pitch angle of placing a ground plane under one of the rotors (green background). a) Effect in the PQUAD multirotor. b) Effect in the AMUSE multirotor

The next experiments were intended to demonstrate the viability of the control approaches presented in previous sections. A first test was performed implementing the feed-forward control scheme, in which the feed-forward term was activated by a switch in the radio of the safety pilot. It can be seen in Figure 3.19 when the feed-forward controller was not activated (Figure 3.19.a), the induced pitch perturbation is similar to the results in Figure 3.18. However, in Figure 3.19.b the feed-forward controller was tested using the switch in the radio and the controller could maintain the pitch angle stably with much smaller variations.

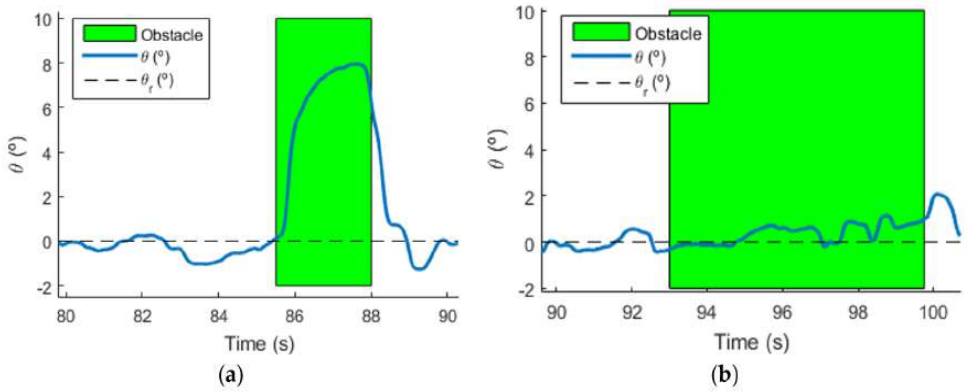

Figure 3.19: Experiments in the testbench, variations of the quadrotor pitch angle when placing a ground plane under one of the rotors (green background): a) with the standard PID controller (not compensating), b) when the compensation is implemented (feed-forward controller)

A second test was performed implementing the disturbance observer presented in Figure 3.8. Figure 3.20 shows the time evolution of the pitch angle during the experiment. As in previous experiments, the green background corresponds to the ground plate placed under one rotor. As can be seen in Figure 3.20, after placing the ground plate, the pitch angle begins to increase, behaving similarly to the first experiments in Figure 3.18, but, right after that, the disturbance observer is able to estimate the external wrench and the controller can effectively compensate it.

The last step in the experimental tests was to reproduce how the ground effect affects during a normal flight. Figure 3.21 shows two images of the experiment; the

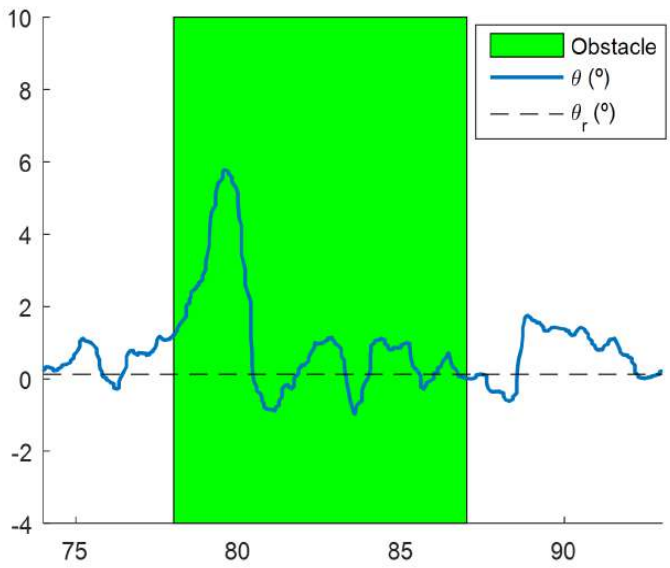

Figure 3.20: Experiments in the testbench, variations of the quadrotor pitch angle when placing a ground plane under one of the rotors (green background)

first one in free flight, and the second one when a ground plane is placed under one of the rotors.

Figure 3.22 shows the evolution of the multirotor pitch angle and the reference during the experiment, in which the multirotor is being controlled with the standard PID cascaded controller, marking with green background when one of the rotors is under the ground effect (partial ground effect). It can be seen that initially the response is similar to the testbench experiments: the pitch angle suffers a perturbation caused by the torque generated by the partial ground effect (different thrust forces of the same rotors for the same input signal). In this case, there is a perturbation in the opposite direction when the partial ground effect disappears and that it was present in some of the testbench experiments but with smaller amplitude (see Figure 3.18.b and Figure 3.19.a). This can be due to several factors of flying outdoors, for example, wind gusts or turbulence. It can also be explained because the quadrotor is attached to the testbench at two points in opposite arms of the quadrotor, allowing it to rotate around the axis (see Figure 3.17), and the friction may dampen the oscillation.

(a) (b)

Figure 3.21: Partial ground effect tests with multirotor flying outdoors: a) multirotor in free flight; b) multirotor flying under partial ground effect (the rotor at the right with a ground plane close to it)

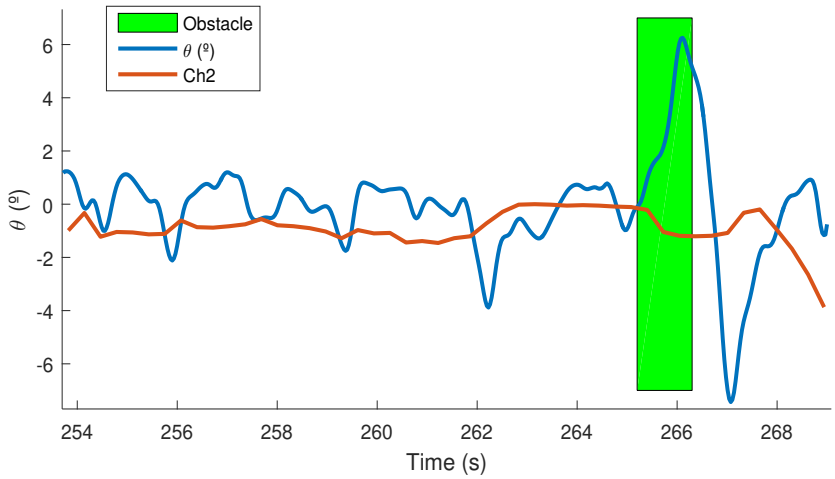

Figure 3.22: Figure 30 Partial ground effect test with the multirotor in flight

3.6 Conclusions

In this chapter, the impact of the aerodynamic ground effects on multirotor systems has been shown. The quantification of this effect is very relevant in applications involving flight very close to surfaces as required in aerial manipulation. This chapter has provided a precise characterisation of the ground effect in multirotors in different situations, which has been modelled similar to single rotor helicopters in many cases in literature. The ground effect has been shown to generate a stabilising moment in multirotors due to the differences in height over the ground of the different rotors. Moreover, the so-called partial ground effect, when only one rotor is over the surface, has been studied. The chapter has also shown which control strategies can be used to compensate this effect by simulations and experiments.

Chapter 4

Applications in infrastructure inspection

> Efficiency is doing things right; effectiveness is doing the right things.
>
> Peter Drucker

4.1 Introduction

This chapter analyses the influence of flying close to a ceiling surface from the underside during an inspection by contact operation. After presenting the problem, a specific aerodynamic study of the ceiling effect is presented. Then, based on these new results, it is presented and analysed a new concept of aerial platform that can take advantage of this aerodynamic effect while it is inspecting. The modelling and controller sections (Sections 4.5 and 4.6) reformulated the problem and present a nonlinear Lyapunov-based controller to deal with this aerodynamic disturbance. Finally, several experiments which are followed by the conclusions of this chapter are presented in a real scenario.

The content of this chapter is based on the following publications:

- Pedro J Sanchez-Cuevas, Pablo Ramon-Soria, Begoña Arrue, Anibal Ollero, and Guillermo Heredia. Robotic system for inspection by contact of bridge beams using uavs. Sensors, 19(2):305, 2019.

- Antonio E Jimenez-Cano, Pedro J Sanchez-Cuevas, Pedro Grau, Anibal Ollero, and Guillermo Heredia. Contact-based bridge inspection multirotors: Design, modeling, and control considering the ceiling effect. IEEE Robotics and Automation Letters, 4(4):3561-3568, 2019.

- Pedro J. Sanchez-Cuevas, G Heredia, and A Ollero. Multirotor uas for bridge inspection by contact using the ceiling effect. In 2017 International Conference on Unmanned Aircraft Systems (ICUAS), pages 767-774. IEEE, 2017.

4.2 Problem statement

Nowadays, the structural assessment of bridges involves the use of a lot of equipment, including heavy machinery, like lifters, scaffolders and cranes, among others. Moreover, although one part of this assessment is a visual inspection to detect cracks, corrosion, leaching and other defects, other tasks require direct contact of a sensor with the structure of the bridge. The contact tasks are usually carried out by an operator that manually places sensors on the bridge to obtain different measurements, such as crack depth or beam deflection. For bridge beam deflection, the most used solution is to place a reflector prism in contact with the bridge and its position is measured with a laser total station on the ground. This task is not just hard and slow due to the use of specified machinery when the bridge environment is very complex, it is also dangerous for the operators.

However, despite of the fact that the use of aerial robots for bridge inspection is not widely extended, the interest in this technology is growing significantly in the last years [94]. For instance, in [95] UAVs have been used to carry out visual inspection and throughout this PhD the author proposed the use of aerial vehicles,which are able to touch and even maintain the contact with the bridge, increasing the use of aerial robots in different applications [77] [80] [78].

These tasks require physical interaction between the aerial robot and the environment and produce significant changes in the dynamic behavior of the aerial platform. For aerial manipulators, these changes are usually due to the movement of the manipulator which could produce variations in both, the aerial vehicle mass center and the inertial characteristics [96] [97].But, in the case of aerial robots that fly very close to structures and obstacles, the behavior of the aircraft changes as a consequence of aerodynamic disturbances [69]. Both problems have been preliminarily studied in literature, for instance, [98] and [71] present a control scheme which takes the movement of the arm of aerial manipulators into account while [79] it is focused on the controller of multirotors working close to ground surfaces. External wrench observers [99] have been used to estimate unknown forces and torques acting on the multirotor, and design controllers for the aerial robot [100]. These observers could be used to estimate these aerodynamic effects, although when the multirotor approaches the surfaces, there are large gradients in the generated forces, and wrench observers are not well suited for estimating fast varying forces.

The problem of UAVs flying close to obstacles that act as a ceiling surface had not been studied in detail. It is clear that, according to the preliminary study in Chapter 2, the ceiling effect appears when the aerial platform is flying close enough to a horizontal surface from below. This situation, which happens during the inspection of the beams of a bridge, produces changes in the flow field that significantly increases the thrust generated by the rotor. An important point is that, while in the ground effect the increment in the rotor thrust moves the UAV away from the surface, producing a "safe" situation moving the platform away [79], in the ceiling effect, the increment in rotor thrust brings the UAV closer the surface, leading to a dangerous situation that can cause a crash with the ceiling. For this reason, it is important to consider it in the design of the aerial robot and the control scheme.

This chapter describes the system developed to accomplish the bridge inspection by contact using UAVs in safety conditions. Thanks to the design proposed, the aerodynamic effects, which arise flying close to the bridge, can be exploited to improve the main performances of the aircraft, such as, the power consumption and the accuracy during the inspection task.

4.3 Preliminary aerodynamic assessment

There is little research related to the aerodynamic effect flying close to the ceiling [69] [101]. This effect, known as ceiling effect, appears when the propeller is very close to a ceiling surface. Therefore, the propeller causes a suction up-wash generating a greater pressure difference on the propeller disk. Moreover, this decreases the drag and increases the thrust because the rotors can rotate faster. The ceiling effect appears because this effect can help to solve typical problems that arise in some applications of aerial vehicles that need to physically interact with the environment, as it is the case of the inspection of bridges and other infrastructure by contact.

Moreover, it is well-known that standard multirotor configurations are not well suited for flying very close to the ceiling because, in general, rotors are not protected from impacts in the upper part, and, in many cases, sensors and antennae are placed in the central part of the body above the plane of the rotors. This is significant also for the aerodynamic point of view, because, at this point, it is clear that the design of the platform will affect the aerodynamic effect. Then, a previous prototype was developed with the purpose of assessing how the fairing can affect the aerodynamic effect (see Figure 4.1).

This design is based on a quadrotor in cross configuration, with all the elements (autopilot, batteries, sensors...) placed at or below the plane of the rotors, and special fairings that surround each rotor. It also allows it to maintain the contact firmly to the lower part of the bridge, placing the fairings in contact with the bridge beam surface with the rotors spinning at few centimeters of the surface without colliding with it. The motorisation used is the DJI E305 motorisation kit and a 4s LiPo as power supply. The weight of the platform is approximately 1.5 kg with a maximum flight time of 14 min. The distance between the rotors axis is 480 mm.

The fairings are located surrounding the rotors with a circular form to easily guarantee the safety of the propellers and the multirotor. The diameter of this fairing is 280 mm. The top of the fairing must be covered with a rubber material to avoid wearing it and facilitate contact with the surface. The fairing must have air intakes to

Figure 4.1: First prototype of the bridge inspection platform

ensure the generation of thrust by the rotors when the multirotor will be in contact with the ceiling.

Once the robot was built, its aerodynamic behaviour was experimentally assessed in the test stand presented in the Chapter 2 (see Figure 4.2).

Experimental results (Figure 4.3, show that the aerodynamic behavior of the designed multirotor is different to the one presented in Section 2.5.2, due to the presence of the fairings around the rotors. In this case, the fairing that surrounds each rotor allows to isolate the aerodynamic effects, and it is expected that there will be no much difference between the single rotor and the complete quadrotor cases.

Then, it is necessary to assess the ceiling effect with the fairing before the experiment validation. This implies the execution of new experiments in the test stand with the designed fairing. Figure 4.3 shows both experimental configurations in the test stand: the single rotor and the complete quadrotor ones. The experiments were done with the PWM of overfly (52%).

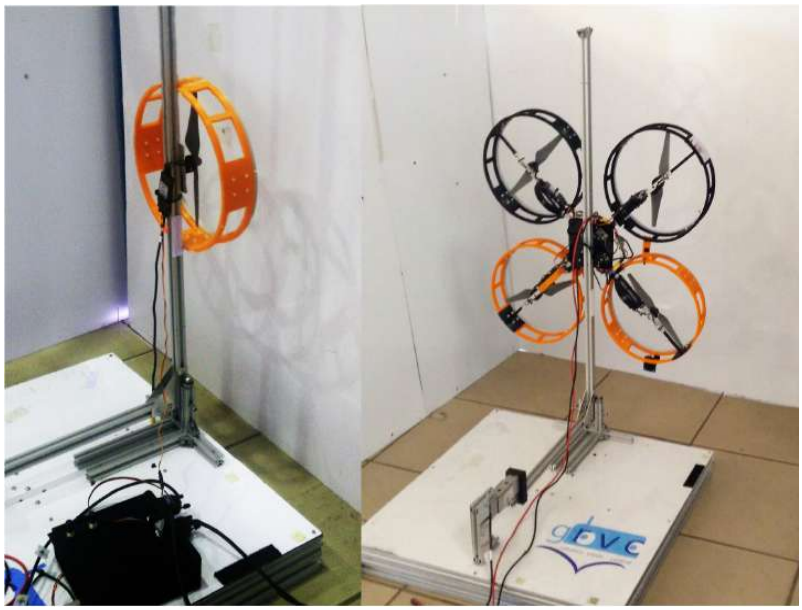

Figure 4.2: First prototype of the bridge inspection platform during the experiments in the test stand

Figure 4.3 shows the results of these experiments. The ceiling effect in both cases is very similar. As above mentioned, this is an expected result. The fairing surrounding each rotor allows to isolate the aerodynamic effects when the rotors are close to the ceiling. Then the interference between the airflow entering each rotor is reduced.

However, this preliminary robot did not address the rest of the requirements imposed by the AEROBI project applications. Then, an improvement version of the robot was designed and analysed in depth to meet those requirements.

4.4 Aerodynamics based design

Although in previous results the aerodynamics of the ceiling effect has been analysed by the author from an experimental point of view, the application range of these works is limited to the studied multirotor because the aerodynamic effect heavily depends on the aerial platform geometry. Therefore, this paper assesses and models

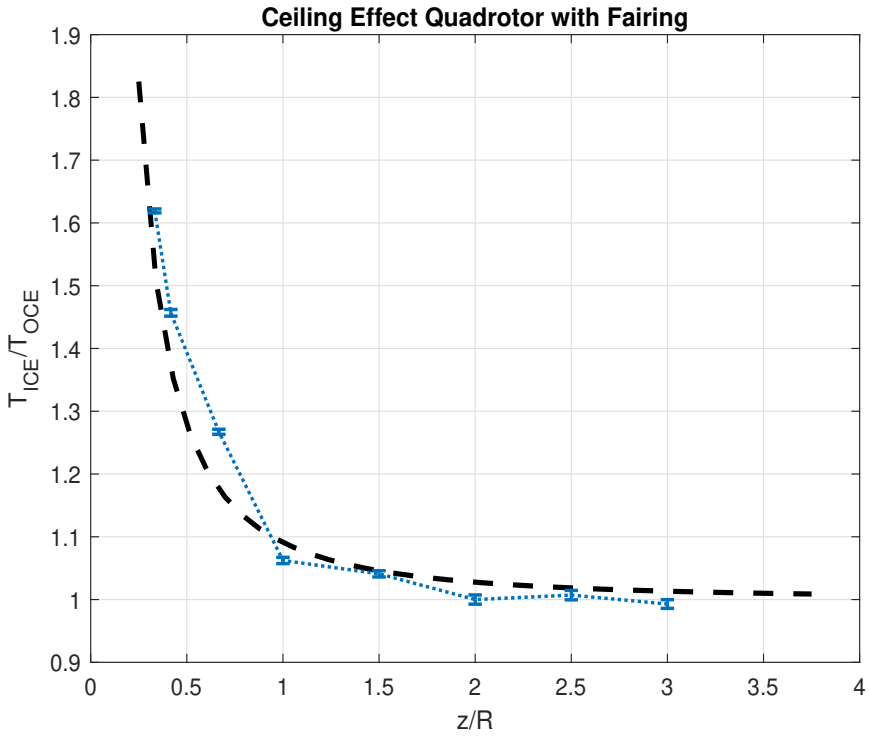

Figure 4.3: Ceiling effect in a multirotor with fairings compared with the experimental curve for an isolated rotor

the aerodynamic ceiling effect on the quadrotor using Computational Fluid Dynamics (CFD) to optimise the performance of the aircraft during the inspection. These simulations have been carried out using the ANSYS environment.

4.4.1 Meshing

Figure 4.4 shows the complete geometry of the proposed aircraft and the simulated mesh. The two symmetry planes are defined in ANSYS Fluent as symmetry boundary conditions. Therefore, the modeled domain is reduced to a portion of 1/4th, improving calculation times without any loss in Maccuracy.

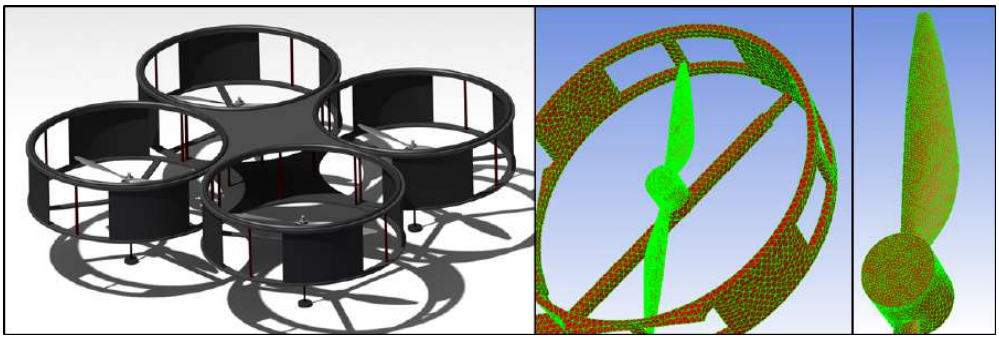

Figure 4.4: Geometry of the refined prototype for bridge inspection and mesh for CFD detail

Different meshes have been done at different distances between the propeller and the ceiling surface, ranging from 4cm (at this distance, the quadrotor frame touches the ceiling) to 50cm.

4.4.2 Solver settings

Firstly, the turbulence model used in this case was the "$k-\varepsilon$ Realizable" which is the most common model used in CFD to simulate mean flow characteristics for turbulent flow conditions. Secondly, the equations employed to solve the problem are the mass, momentum and energy conservation. Thirdly, the fluid is modelled as an ideal gas. Lastly, boundary conditions are defined as follows: the propeller is a wall with no-slip

condition which rotates around its axis. The frame and the top surface of the domain (ceiling) are considered as stationary walls with no-slip condition. The lateral and bottom limits of the area are both defined at constant pressure and temperature of 1 atm and 300K to emulate far-away flow field conditions. Both symmetry planes are established as symmetry boundary conditions.

A transient simulation is solved to take the movement of the propeller into consideration. The time step is chosen to be equivalent to a 1/10th of a propeller complete revolution, so it varies between simulations where the angular speed of the propellers changes. For each time step, the software iterates until convergence is reached. This process continues for 10 propeller complete revolutions to ensure stable results.

4.4.3 Methodology

Previous results in Section 2.5.2 have shown that the ceiling effect does not only increase the thrust but it also changes the velocity of the rotors (RPM). This is due to the suction that arises when the rotors work very close to the ceiling, which decreases the air pressure around the propellers and the power consumed by the rotors. Most electronic speed controllers work sending PWM signals to the rotors and do not have closed-loop speed control. Therefore, they cannot compensate this effect. As a result, this problem is analysed as follows to properly model the ceiling effect:

For a quadrotor in free flight conditions, the relations between thrust T, angular speed Ω, and power consumed P on each rotor have been assumed in the literature as:

$$T(\Omega) = C_T \Omega^2 \tag{4.1}$$

$$P(T) = K_P T^{1.5} \tag{4.2}$$

In these expressions, C_T and K_P are constants whose value only depend on the geometry of the propeller (diameter, pitch, airfoil distribution) and the ambient conditions (air density, relative humidity). However, if the platform flies close to an obstacle, these expressions are no longer valid. In the case of use of this work, these

variables also change with the distance to the ceiling when the aircraft flies close to the bridge.

To model this ceiling effect, two assumptions can be made:

Assumption 1: C_T and K_P do not remain constant but are functions of the distance from the propeller to the ceiling z. 2) C_T and K_P remain independent of the angular speed Ω.

Assumption 2: The relations between T,P and Ω remain unchanged.

Both assumption 1 and assumption 2 will be validated using CFD in the next section. Then, the classical approach of T and P can be reformulated as follows:

$$T_{ICE}(z,\Omega) = C_{T_{ICE}}(z)\Omega^2 \tag{4.3}$$

$$P_ICE(z,T) = K_{P_{ICE}}(z)T^{1.5} \tag{4.4}$$

Therefore, the ceiling effect is modelled through the functions $C_T(z_i)$ and $K_P(z_i)$ and then, it is assumed that the thrust can be modeled as:

$$T_{ICE}(z,\Omega) = K_c(z)C_{T_{OCE}}\Omega^2 \tag{4.5}$$

4.4.4 CFD Results

Several CFD simulations were performed to validate the assumptions of the previous sections. These simulations consisted of assessing the behavior of a quadrotor in terms of thrust, T, and power, P. More than 30 different simulations for different distances and RPM were performed. The qualitative behavior of the flow field can be explained with the two simulations presented in Figure 4.5

In Figure 4.5.a the quadrotor is touching the ceiling and in Figure 4.5.b it is placed at 10cm of the ceiling. Then, when rotating, the propellers (in black in Figure 4.5) take the upstream air and accelerate it downwards. In the presence of the ceiling, the air movement is restricted, and a low-pressure bubble also appears between the rotor

and the ceiling. Thus, the air particles close to the ceiling and in the proximity of the propeller are attracted to the rotor area and accelerated down-wash. Far away from the propeller, the fluid remains unaltered (deep blue).

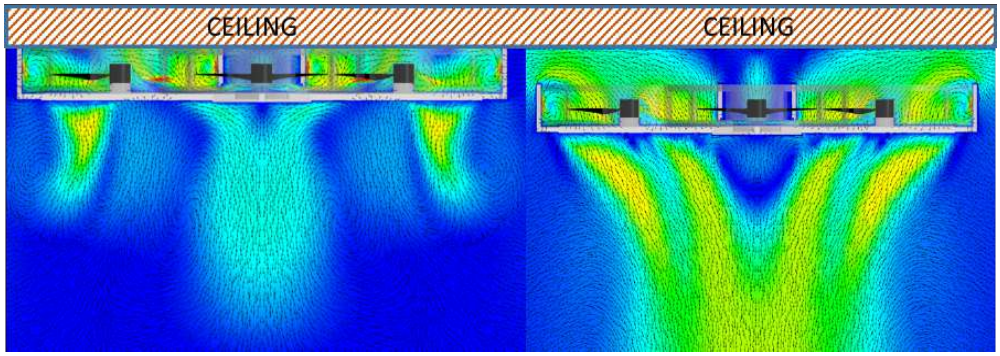

Figure 4.5: Velocity field when the multirotor is: a) in contact with the ceiling; b) flying 10 cm below the ceiling.

Assuming the distance to the ceiling as $z = z_j$ and the angular speeds as $\Omega = \Omega_k$, the equations of the assumptions 1 and 2 become linear when taking logarithms:

$$\log T_{jk} = \log C_{T_{ICE,jk}} + 2 \log \Omega_k \tag{4.6}$$

$$\log P_{jk} = \log K_{T_{ICE,jk}} + 1.5 \log T_{jk} \tag{4.7}$$

Thus, since the CFD simulations provide a complete solution to the flow field of the problem, it is possible to validate these expressions as a consequence the assumption 2. This has been done calculating the values of the exponents in the expressions of assumption 2 by means of the values of T,C_T,P and K_P provided by the CFD. The results are presented in the table below and validate the relations between T, P and Ω. Assumption 1 is validated through the results presented in Figure 4.6 and Figure 4.7 for different rotation velocities, where it can be clearly seen that the ceiling effect does not depend on the RPM.

Last, Figure 4.7 shows the results of $K_c(z)$ that appear when the rotors approach the ceiling assuming that the power is constant. This model, which is represented by the yellow dashed line in Figure 4.7, has been compared with previous results with

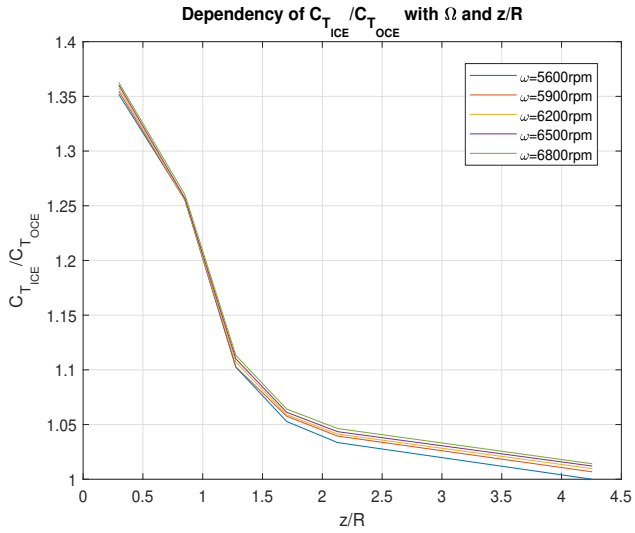

Figure 4.6: C_T vs z/R for different RPMs

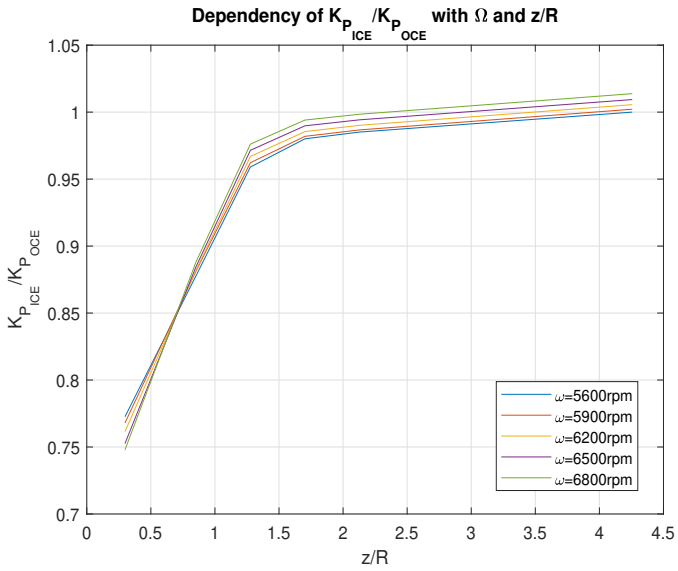

Figure 4.7: K_p vs z/R for different RPMs

Model	Exp. Mean value	Exp. Standard deviation
$T_{ICE}(z,\Omega) = C_{T_{ICE}}(z)\Omega^2 - Exp2$	2.0487	0.0178
$P_{ICE}(z,T) = K_{P_{ICE}}(z)T^2 - Exp1.5$	1.4796	0.0482

other platforms [78], showing that the designed platform exploits the ceiling effect in a more effective way than in previous designs.

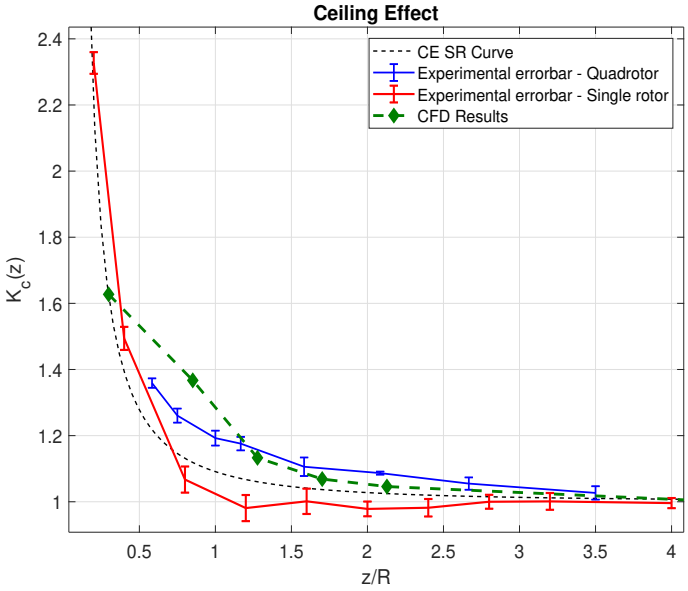

Figure 4.8: CFD Experimental Results Comparison. Blue error bar and red errorbar are experimental results for quadrotor and multirotor respectively. Black braked line is the model proposed in 2.5.2 for the single rotor in ceiling effect. Yellow braked line is the model used in this work for the aerial platform designed (4.8)

For this platform, K_C is modeled as:

$$K_C(z) = \frac{1}{1 - \frac{1}{a_1}(\frac{R}{a_2+z})^2} \tag{4.8}$$

Both, $a_1 = 0.081$ and $a_2 = 1.026$ are values obtained through least squares minimising the error with the CFD results.

4.5 Dynamic model of the multirotor close to the ceiling

The dynamic model of a quadrotor is widely known in bibliography [102]. Thus, defining a set of generalized coordinates as $\xi = [x \quad y \quad z \quad \phi \quad \theta \quad \psi]^T$, and considering the ceiling effect, the dynamic model of a quadrotor is described by the following equations.

$$\ddot{\xi} = \begin{bmatrix} 0 \\ 0 \\ -g \\ \dot{\theta}\dot{\psi}(\frac{I_y - I_z}{I_x}) - \frac{J_r}{I_x}\dot{\theta}\Omega \\ \dot{\theta}\dot{\psi}(\frac{I_x - I_z}{I_y}) - \frac{J_r}{I_y}\dot{\theta}\Omega \\ \dot{\phi}\dot{\theta}(\frac{I_x - I_y}{I_z}) \end{bmatrix} + \begin{bmatrix} \frac{1}{m}I_3 & 0 \\ 0 & \alpha\mathbb{I}^{-1} \end{bmatrix} F(\xi) + F_e \tag{4.9}$$

with

$$\alpha = \begin{bmatrix} d & 0 & 0 \\ 0 & d & 0 \\ 0 & 0 & 1 \end{bmatrix}, \mathbb{I} = \begin{bmatrix} I_x & 0 & 0 \\ 0 & I_y & 0 \\ 0 & 0 & I_z \end{bmatrix}, I_3 = \begin{bmatrix} 1 & 0 & 0 \\ 0 & 1 & 0 \\ 0 & 0 & 1 \end{bmatrix} \tag{4.10}$$

$$\Omega = \Omega_1 - \Omega_2 + \Omega_3 - \Omega_4 \tag{4.11}$$

Here, g is the gravity, d is the distance between the geometric center of the quadrotor and the center of a rotor; $I_i (i = x, y, z)$ are diagonal terms of the inertia matrix; m is the aerial vehicle total mass and J_r is the rotor moment of inertia. Vector $F(\xi)$ encompasses actuator forces and torques exerted by the rotors. These forces and torques depend on the state of the multirotor due to the aerodynamic effects. Lastly, F_{ext} includes external forces and torques which are not known or modelled, such as contact forces or wind disturbances. The mass matrix and the gravity vector are the same that have been widely presented in literature, but, in this case, and due to the flight conditions, the force vector acting on the vehicle is:

$$F(\xi) = \begin{bmatrix} (c_\phi s_\theta c_\psi + s_\phi s_\psi)T(\xi) \\ (c_\phi s_\theta s_\psi + s_\phi c_\psi)T(\xi) \\ c_\phi c_\theta T(\xi) \\ \tau_\phi(\xi)) \\ \tau_\theta(\xi) \\ \tau_\psi(\xi) \end{bmatrix} \tag{4.12}$$

where $c_\alpha = \cos\alpha$,$s_\alpha = \sin(\alpha)$ and (ϕ, θ, ψ) are the Euler angles. Defining the total thrust $T(\xi)$, as $T(\xi) = \sum_{i=1}^{4} T_i(\xi)$, and taking it into account that the platform is a quadrotor in cross configuration, there is a direct correspondence between the four generalised moments and the angular velocities of the rotors in which the vector $F(\xi)$ follows 4.12, where the aerodynamic ceiling effect has been included.

$$F(\xi) = \begin{bmatrix} T \\ \tau_\phi \\ \tau_\theta \\ \tau_\psi \end{bmatrix} = \begin{bmatrix} K_c(z_{c_1})c_T & K_c(z_{c_2})c_T & K_c(z_{c_3})c_T & K_c(z_{c_4})c_T \\ -K_c(z_{c_1})dc_T & K_c(z_{c_2})dc_T & K_c(z_{c_3})dc_T & -K_c(z_{c_4})dc_T \\ K_c(z_{c_1})dc_T & -K_c(z_{c_2})dc_T & K_c(z_{c_3})dc_T & -K_c(z_{c_4})dc_T \\ c_D & c_D & -c_D & -c_D \end{bmatrix} \begin{bmatrix} \Omega_1^2 \\ \Omega_2^2 \\ \Omega_3^2 \\ \Omega_4^2 \end{bmatrix} \tag{4.13}$$

where $z_(c_i)$ is the distance from the i-rotor to the ceiling, defined as follows:

$$\begin{aligned} z_{c_1} &= z_c - \tfrac{\sqrt{2}}{2} d(\sin(\theta) - \cos(\theta)\sin(\phi)) \\ z_{c_2} &= z_c - \tfrac{\sqrt{2}}{2} d(-\sin(\theta) + \cos(\theta)\sin(\phi)) \\ z_{c_3} &= z_c - \tfrac{\sqrt{2}}{2} d(\sin(\theta) - \cos(\theta)\sin(\phi)) \\ z_{c_2} &= z_c - \tfrac{\sqrt{2}}{2} d(-\sin(\theta) + \cos(\theta)\sin(\phi)) \end{aligned} \tag{4.14}$$

where z_c is the distance from the center of gravity of the multirotor to the ceiling.

4.6 Control

In this section, we present a nonlinear Lyapunov-based attitude, altitude and position controllers for bridge inspection flights. The main goal of the designed controller

is that the quadrotor can fly very close to the beams and carry out contact tasks with safety and accuracy. The ceiling effect is the most critical aerodynamic effect occurring during these inspection tasks. In the previous section, the ceiling effect has been modelled and introduced in the equations of the motion system. The relationship between the control inputs and the angular velocities of the rotors have been shown in equation 4.13. In this expression, the z_{c_i} of each rotor has been calculated to obtain the ceiling effect for each one. Depending on the multirotor attitude, the ceiling effect is different in each rotor. As Figure 4.9 shows, if the aircraft has a pitch angle about $\pm$ 10 degrees (flight forward), the aerodynamic ceiling effect is approximately a 22% higher in one rotor than in the other when $z_c = 0.1m$. However, it decreases to 5% when the attitude angles are about $\pm$ 3 degrees. Furthermore, it decreases to 2% when $z_c = 0.25m$. This result implies that it is possible to make the following assumptions to increase the safety during the operation:

3.1: A forward flight will be done to a minimum distance of 0.25 m. to the ceiling surface.

3.2 The only operation allowed for distances less than 0.25 m will be the hover until reaching the contact with the surface.

Taking into account the assumptions 3.1 and 3.2, expression (4.8) is linearised in intervals in which the difference between the aerodynamic effects is less than 5% and, therefore $z_c \sim z_{c_1} \sim z_{c_2} \sim z_{c_3} \sim z_{c_4}$.

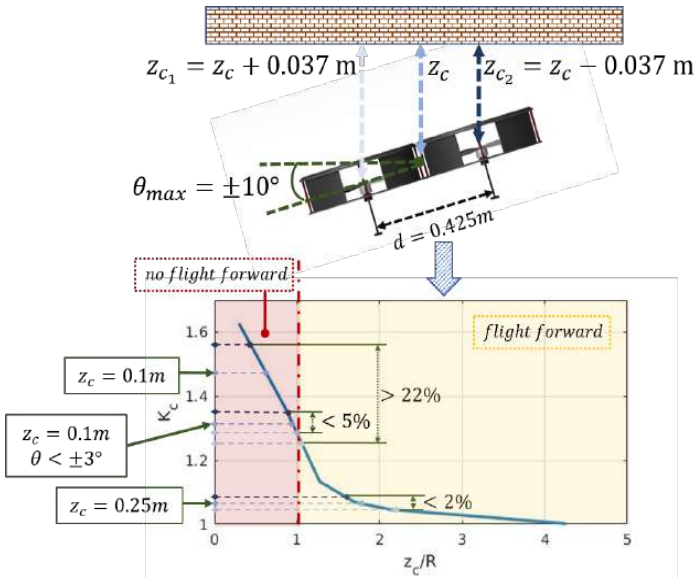

Figure 4.9: Response of a multirotor in ceiling effect and safety flight envelope. Red area represents the very close to the bridge area in which flight forwards commands are not allowed. In yellow area, the ceiling effect gradient will be lower than a 5% between the rotors to ensure the stability of the platform.

Thus, the expression for the control inputs (4.13) can be simplified as follows:

$$U = \begin{bmatrix} K_C(z_c) & 0 & 0 & 0 \\ 0 & K_C(z_c) & 0 & 0 \\ 0 & 0 & K_C(z_c) & 0 \\ 0 & 0 & 0 & 1 \end{bmatrix} \begin{bmatrix} c_T & c_T & c_T & c_T \\ -dc_T & dc_T & dc_T & -dc_T \\ dc_T & -dc_T & dc_T & -dc_T \\ c_D & c_D & c_D & c_D \end{bmatrix} \begin{bmatrix} \Omega_1^2 \\ \Omega_2^2 \\ \Omega_3^2 \\ \Omega_4^2 \end{bmatrix} \tag{4.15}$$

Then,

$$\begin{bmatrix} T \\ \tau_\phi \\ \tau_\theta \\ \tau_\psi \end{bmatrix} = \begin{bmatrix} K_C(z_c) & 0 & 0 & 0 \\ 0 & K_C(z_c) & 0 & 0 \\ 0 & 0 & K_C(z_c) & 0 \\ 0 & 0 & 0 & 1 \end{bmatrix} \begin{bmatrix} U_z \\ U_\phi \\ U_\theta \\ U_\psi \end{bmatrix} \tag{4.16}$$

4.6.1 Nonlinear Attitude Controller

The attitude control keeps the stabilisation of the aerial platform and the desired 3D orientation needed to track a desired path. As the derivation is similar to the roll, pitch and yaw angles controller, only the roll controller formulation will be presented. Firstly, let us define the tracking error and the speed tracking one as:

$$e_\phi = \phi - \phi_d \tag{4.17}$$

$$e_{\dot{\phi}} = \dot{\phi} - \dot{\phi}_d + k_\phi e_\phi \tag{4.18}$$

The stability of the roll controller is checked defining a Lyapunov function. Then, we propose the candidate Lyapunov function, V_ϕ, defined as:

$$V_\phi = \frac{1}{2}(e_\phi^2 + e_{\dot{\phi}}^2) \tag{4.19}$$

Both angular tracking and speed tracking errors have been included in the candidate Lyapunov function. Thus, deriving (4.19) and using (4.9) gives,

$$\dot{V}_\phi = e_\phi \dot{e}_\phi + e_{\dot{\psi}} \dot{e}_{\dot{\psi}} = e_\phi (e_{\dot{\phi}} - k_\phi e_\phi) + e_{\dot{\phi}} (\ddot{\phi} - \ddot{\phi}_d + k_\phi (e_{\dot{\phi}} - k_\phi e_\phi)) \tag{4.20}$$

$$\dot{V}_\phi = e_\phi (e_{\dot{\phi}} - k_\phi e_\phi) + e_{\dot{\phi}} (\dot{\theta}\dot{\psi}(\frac{I_y - I_z}{I_x}) - \frac{J_r}{I_x}\dot{\theta}\Omega + \frac{dK_c(z_c)}{I_x} U_\phi - \ddot{\phi}_d + k_\phi (e_{\dot{\phi}} - k_\phi e_\phi)) \tag{4.21}$$

Now, in order to guarantee the stability, gains should be selected to guarantee that it is seminegative definite, then, the control input for roll attitude is given by:

$$U_\phi = \frac{I_x}{dK_c(z_c)} (\dot{\theta}\dot{\psi}(\frac{I_y - I_z}{I_x}) - \frac{J_r}{I_x}\dot{\theta}\Omega + (k_\phi^2 - 1)e_\phi - (k_\phi + k_{\dot{\phi}})e_{\dot{\phi}} \tag{4.22}$$

where k_ϕ and k_ϕ are positive constants. Therefore, using (4.22) in (4.21) results

$$\dot{V}_\phi = -k_\phi e_\phi^2 - k_{\dot{\phi}} e_{\dot{\phi}}^2 \leq 0 \tag{4.23}$$

As a result, a global asymptotic stability is guaranteed thanks to the positive definition of V_ϕ, the fact that $V_\phi < 0, \forall (e_\phi, e_{\dot{phi}} \neq 0$ and $\dot{V}_\phi(0) = 0$ and by applying LaSalle's theorem. Following the same steps, the control inputs for pitch and yaw are given by:

$$U_\theta = \frac{I_y}{dK_c(z_c)} (\dot{\phi}\dot{\psi}(\frac{I_x - I_z}{I_y}) - \frac{J_r}{I_y}\dot{\phi}\Omega + (k_\theta^2 - 1)e_\theta - (k_\theta + k_{\dot{\phi}})e_{\dot{\phi}} \tag{4.24}$$

$$U_\psi = I_z (\dot{\phi}\dot{\theta}(\frac{I_x - I_y}{I_z}) + (K_\phi^2 - 1)e_\psi - (k_\psi + k_{\dot{\psi}})e_{\dot{\psi}} \tag{4.25}$$

4.6.2 Nonlinear Altitude Controller

In the first step to design the proposed altitude controller, the tracking error and the speeds tracking error are defined as follows:

$$e_z = z - z_d \tag{4.26}$$

$$e_{\dot{z}} = \dot{z} - \dot{z}_d + k_z e_z \tag{4.27}$$

Where k_z is a positive constant. Thanks to the error definitions (4.26) and (4.27), it is possible to define a candidate Lyapunov function V_z to stabilize the altitude control system as follows:

$$V_z = \frac{1}{2}(e_z^2 + e_{\dot{z}}^2) \tag{4.28}$$

Then, deriving the equation (4.28), and using the equation (4.9) it gives:

$$\dot{V}_z = e_z\dot{e}_z + e_{\dot{z}}\dot{e}_{\dot{z}} = e_z(e_{\dot{z}} - k_z e_z) + e_{\dot{z}}\left(\frac{c\theta c\phi K_c(z_c)}{m}U_z - g\ddot{z}_d + k_z(e_{\dot{z}} - k_z e_z)\right) \tag{4.29}$$

Assuming that the ceiling effect function is positive (see Figure 4.8, $K_c(z_c) \geqslant 1, \forall z_c \in \mathbb{R}$, and $z_d \ddot{=} 0$, then, due to the error definitions and according to the Lyapunov's stability theorem, the control input, U_z, is defined as follows:

$$U_z = \frac{m}{c\theta c\phi K_z(z_c)}(g + (k_z^2 - 1)e_z - (k_z + k_{\dot{z}})e_{\dot{z}}) \tag{4.30}$$

Where k_z is a positive constant. Using the equation 4.30 in 4.29, the time derivative of the candidate Lyapunov function is rewritten as:

$$\dot{V}_z = -k_z e_z^2 - k_{\dot{z}} e_{\dot{z}}^2 \leq 0 \tag{4.31}$$

Equation (4.31) holds if and only if 4.30 exists. Then, both attitude angles, roll and pitch, should be bounded between $-\pi/2$ and $\pi/2$. Keeping this condition, $\dot{V}_z$ is seminegative definite and the altitude control is asymptotically stable. The proposed altitude control presents two advantages. The first one is to keep the altitude during a flight forward when $R/z_c > 1$ and therefore $K_c(z_c) \sim 1$. The second one is during a contact mission. In this case, the attitude angles, roll and pitch, should be small and when the multirotor is flying close to the ceiling, the function $K_c(z_c)$ should increase and the multirotor should be able to keep the altitude as well as reducing the thrust input and, therefore, minimising the energy consumption.

4.6.3 Nonlinear Position Controller

In underactuated systems, like quadrotors, the horizontal motion is achieved by tilting the quadrotor towards the desired direction. Thus, the position control is responsible for commanding the desired roll and pitch angles to the attitude controller. Following the steps of previous subsections, we could define the position tracking and speed tracking errors as:

$$\begin{aligned} e_x &= x - x_d \\ e_{\dot{x}} &= \dot{x} - \dot{x}_d + k_x e_x \\ e_y &= y - y_d \\ e_{\dot{y}} &= \dot{y} - \dot{y}_d + k_y e_y \end{aligned} \tag{4.32}$$

Then, the control laws are given by,

$$U_x = \frac{m}{U_z}((k_x^2 - 1)e_x - (k_x + k_{\dot{x}})e_{\dot{x}}) \tag{4.33}$$

$$U_y = \frac{m}{U_z}((k_y^2 - 1)e_y - (k_y + k_{\dot{y}})e_{\dot{y}}) \tag{4.34}$$

The generated position control signals are used to obtain the desired roll, ϕ_d, and pitch angles, θ_d.

4.7 Experimental Results

4.7.1 Hardware/Software Description

This section describes the system used in the experiments outdoors, which is shown in Figure 4.10.

Figure 4.10.a shows the platform used during the experiments, which is a cross layout quadrotor with the propulsive system and the avionics onboard covered in a full carbon fiber frame. The propulsive system consists of DJI 2312E rotors with 9 inches propellers DJI and 420Lite ESC and the onboard avionics consist of a custom autopilot code running in a Raspberry Pi 3 Model B connected to the Emlid's sensors

Figure 4.10: System overview. a) Aerial Platform. b) Reflector Prism. c) GCS. d) Robotic total station

shield Navio2. This hardware supports Wi-Fi technology that has been used to link the ground control station (Figure 4.10.c) with the aerial platform. In addition, the platform also mounts a range sensor SF11/C LIDAR connected through the I2C bus. Figure 4.10.d and Figure 4.10.b show the robotic total station (Leica Geosystem MS50) and the reflector prism (GRZ 360° mini-prism) used to accomplish the measurements during the inspection and to estimate the position of the aircraft during the flight in the position control loop. The accuracy of these measurements is about 1 cm in flight and it increases during the contact inspection to 0.1mm. The maximum frequency of the measures is 20 Hz. The hardware/software architecture is presented in Figure 4.11. This scheme shows that the autopilot is connected to the GCS through a Wi-Fi link. The robotic total station is also connected to the GCS through a serial port. The GCS receives the prism position and sends it to the aerial platform, acting as a bridge between the robotic total station and the aerial platform. However, the measurements of the total station are treated and filtered onboard for safety conditions.

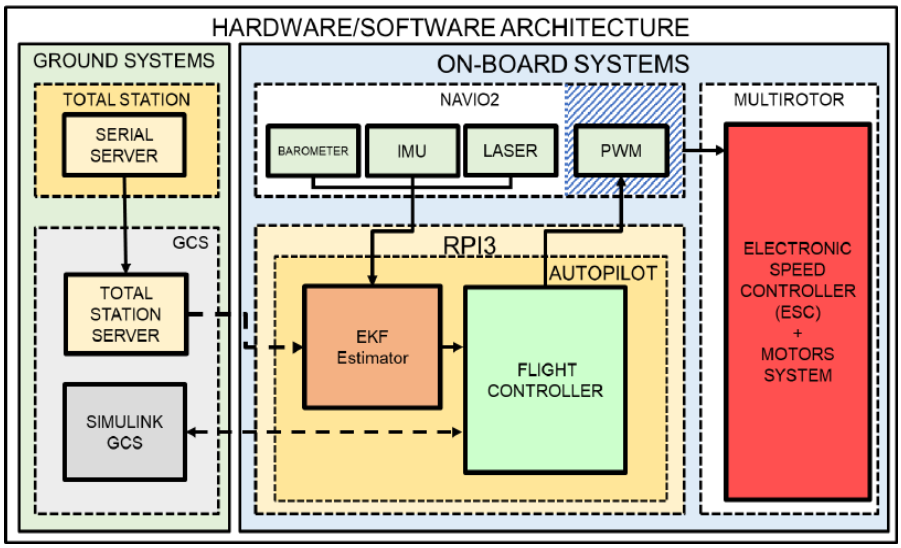

Figure 4.11: Hardware/software architecture. WiFi communication is represented by dashed arrows and wired communication by the bold arrows.

4.7.2 Experiments Overview

The system has been tested in different experiments in the "Navas bridge" in Algodonales, Cadiz, Spain (Figure 4.12). The experiments started with a piloted test, in which the human pilot approaches the multirotor the surface of the bridge in order to obtain a first result of the aircraft behavior in the proximity of the bridge. Next, the nonlinear controller was tested followed by a full autonomous mission which emulates the inspection procedure during a structural assessment task. Figure 4.12 also shows the aerial platform during a contact inspection.

Figure 4.12: Navas bridge and experiment overview

4.7.3 Manual Flight Results

The first experiments, which were carried out piloted by a human, show that the aircraft is very unstable at the end of the contact phase. The results in Figure 4.13 show that the pilot must significantly decrease the thrust signal, at least, up to a 40% less than the thrust hover to finish the contact task. This situation leads to conditions in which the aircraft critically loses its altitude and it could generate a dangerous flight condition. Then, it becomes it clear the need of implementing an automatic control strategy to fix this behavior. This is one of the main conclusions of this work.

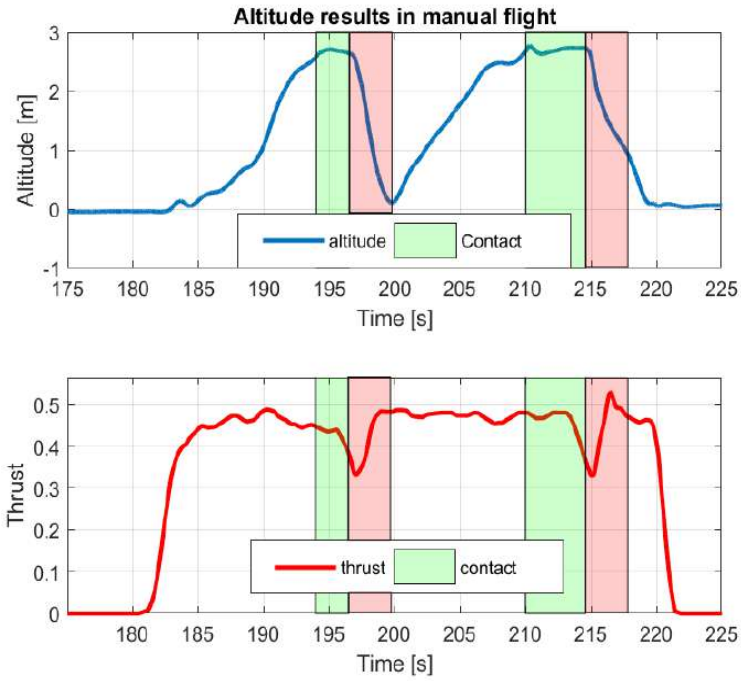

Figure 4.13: Altitude telemetry results during in manual flight. Red zone represents the dangerous area in which the aircraft critically loses its altitude and it could generate a dangerous flight condition

4.7.4 Nonlinear Controller Results

The next experiment was accomplished with the automatic control strategy proposed in Section 4.6. In this case, the results of Figure 4.14 and Figure 4.15 show the altitude controller result, as well as the values of the thrust, the aerodynamic ceiling effect estimation and the vertical velocity. These results reveal that the controller implemented allows the platform to fly in safe conditions when it approaches and moves away from the bridge surface. Moreover, Figure 4.14 also shows how the controller acts during the contact and the commanded thrust. It shows that, in spite of the oscillations due to the error in the state estimation, the mean value of thrust (represented with the red dashed line) decreases as a consequence of taking the ceiling effect in the nonlinear controller into consideration.

It is important to remark that the most important benefits of this nonlinear control appear in the z-position and z-velocity controller. The result in Figure 4.15 shows the z-velocity controller results, in which, it can be observed that the nonlinear controller is faster and the unstick command is followed in a more efficient way. For instance, this result clearly shows that the nonlinear controller easily follows the reference with a small delay (0.25 s), while a standard PID controller needs to integrate and accumulate too much error for following the reference (4 s) because this one does not take the aerodynamic ceiling effect into account. On the other hand, Figure 4.15 also presents the performance of the z-position controller. These results show that the linear controller is not only slower, but it is also less safe due to the overshooting presented in the dangerous zone (red background) which does not appear with the proposed nonlinear controller. Moreover, the reason why both controllers show a small delay is due to the limits of the sensors used to estimate the position of the vehicle. The robotic total station provides a very high positioning accuracy (~ 1 cm), but it has a delay and its updated rate is temporal changing and relatively low, limiting the performance of the nonlinear controller and causing a small delay in the response of the multirotor.

The next section shows a complete telemetry set of the multirotor flying in an inspection of the bridge, where it is possible to assess the result of the controller along the flight.

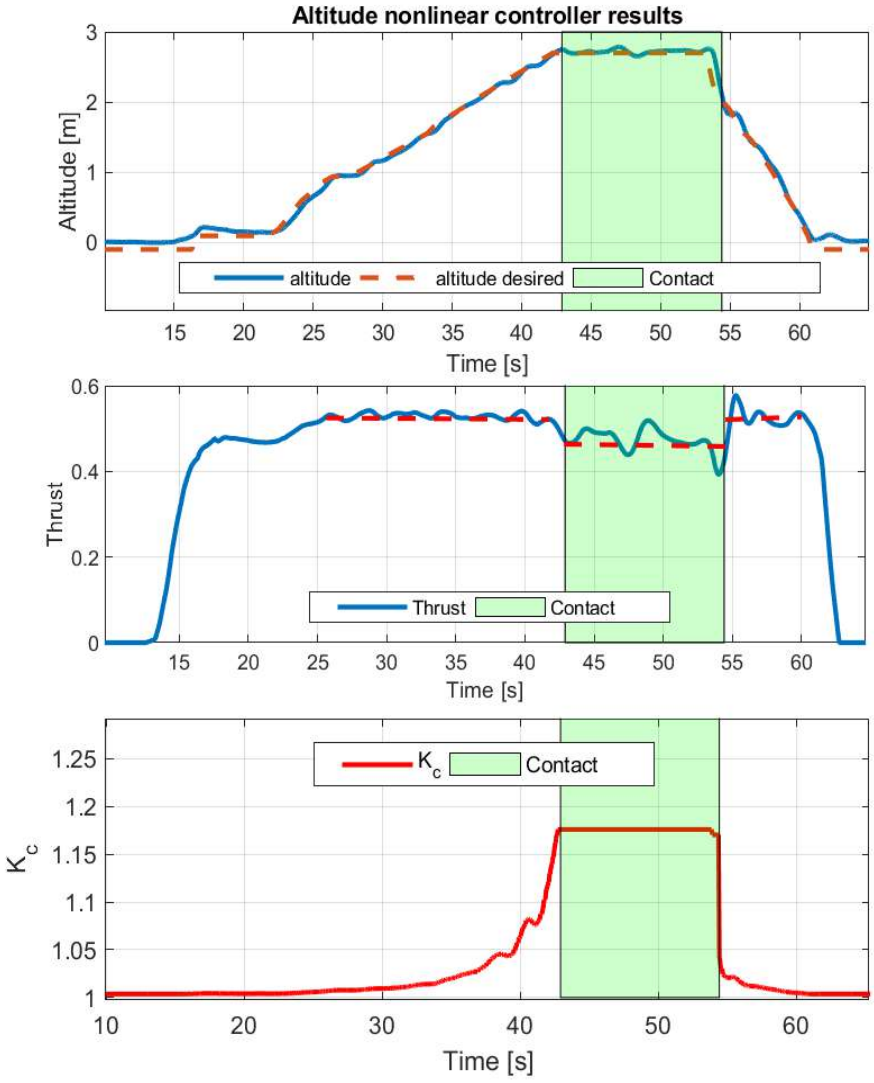

Figure 4.14: Altitude nonlinear controller results. Altitude vs altitude reference control, thrust and mean value during the flight and contact (red dashed), and estimation of the ceiling effect factor (K_c) during the flight

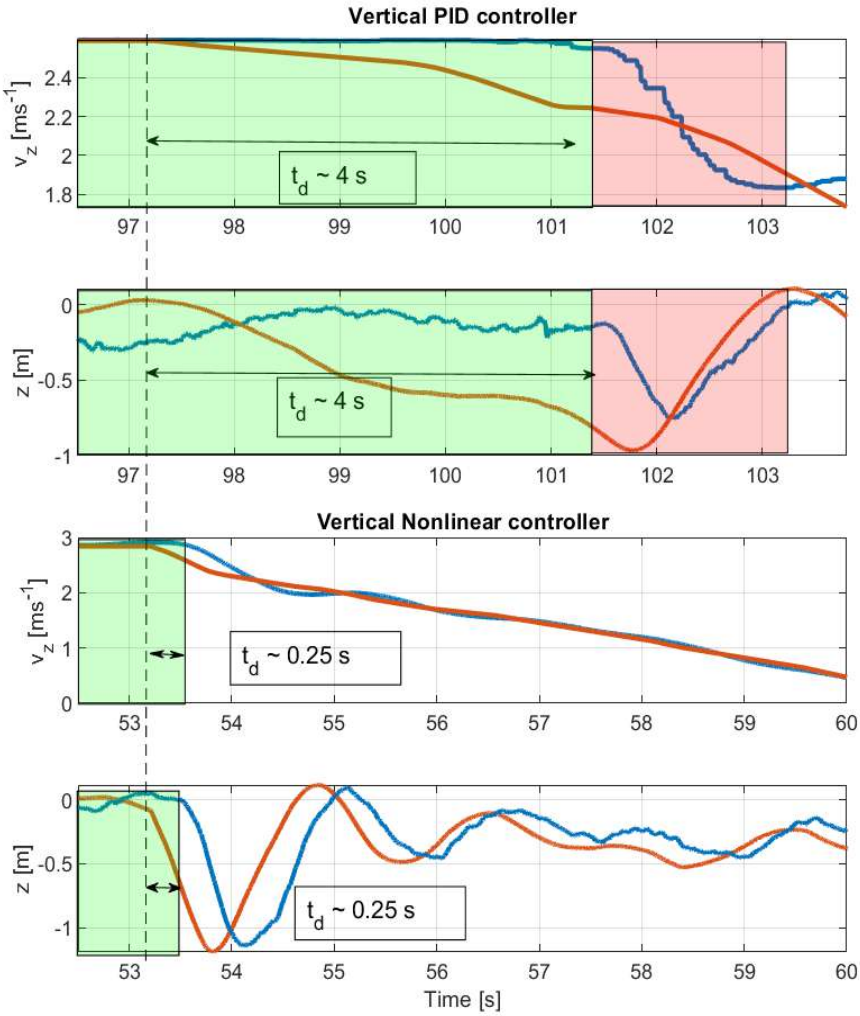

Figure 4.15: PID vs Nonlinear z-velocity and z-position controller comparison. Green backgrounds represent the contact condition; red background is the dangerous zone where it can be observed an overshooting. It is shown that the nonlinear controller is more than 4 times faster moving away from the ceiling.

4.7.5 Autonomous Inspection

The last experiments consisted of accomplishing a full inspection by contact in an autonomous mode. These results, which are presented in Figure 4.16 and Figure 4.17, show that the system is able to navigate between different contact points in safety conditions. In Figure 4.16, it can be seen that the proposed z-position controller allows the aircraft to move away from the ceiling without entering dangerous flight conditions or losing their altitude critically, as it happens in Figure 4.13 (see red area in Figure 4.16).

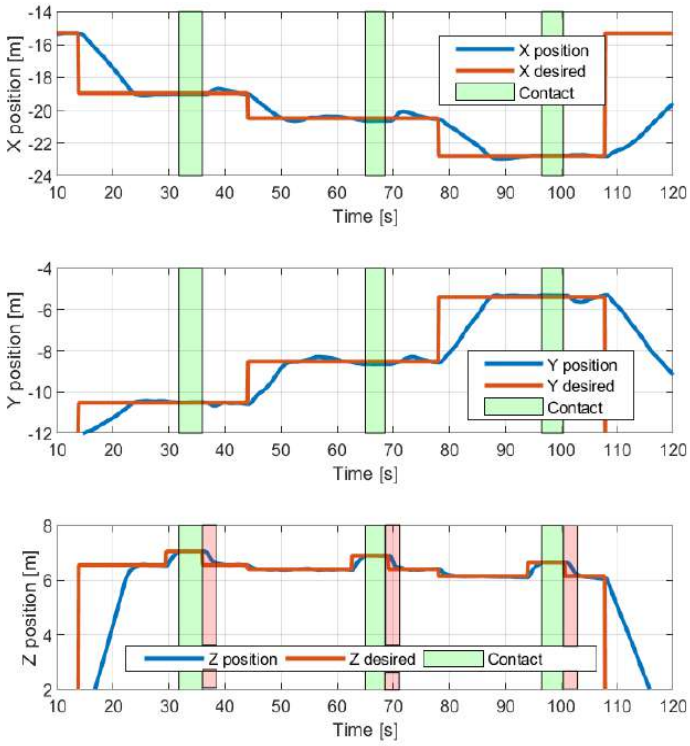

Figure 4.16: Position controller results during an autonomous mission

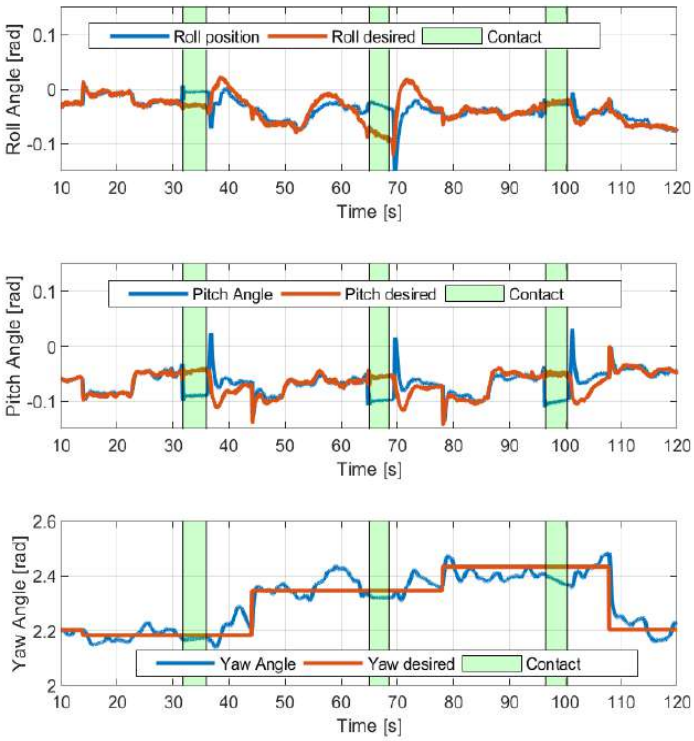

Figure 4.17: Attitude controller results during an autonomous mission

4.8 Conclusions

This chapter has presented the design, modeling and control of a multirotor which is able to fly very close to the ceiling surface and even establishes a full contact with it for carrying out the inspection of a bridge by contact.

The design of the aerial platform was based on a detailed aerodynamic study of the ceiling effect performed with CFD. Thus, the aircraft can exploit the ceiling effect in its favour and do the inspection operation in a more effective way. This ceiling effect was also modeled through the results of the CFD and it was included in the dynamic model of the quadrotor reformulating the classical approach of these equations. Moreover, the controller scheme used to accomplish the contact and to fly close to the surface of the bridge has been described and implemented in a real platform.

Lastly, the outdoor experiments in a real bridge have validated the proposed design, as well as the controller and the aerodynamic characterisation, even during a fully autonomous mission. The future work related to this research will be focused on the end user of this technology and the inspection application.

The aim of these works will be: increase the applicability of this technology, increase its technology readiness level (TRL), and, turn it into a competitive option in the commercial exploitation

Chapter 5

2D Aerodynamic Modelling:

From the 1D aerodynamic effect to the 2D aerodynamic maps

> Una de las virtudes de un verdadero ingeniero es la eficiencia.
>
> Guang Tse

5.1 Introduction

One of the most disruptive trends in UAV applications is the use of the previously presented aerial manipulator in tasks , such as contact inspection and sensor installation in inspection and maintenance (I&M) of infrastructures or industrial plants [103] [77].

These I&M tasks usually require that the aerial platform flies very close to different obstacles. For instance, the PILOTING [37] and HYFLIERS [34] projects are focused on aerial manipulation for outdoor applications in I&M in oil and gas plants. Both cases imply that the aerial platforms need to fly in the proximity or even maintain a contact with an infrastructure to carry out the I&M operations. Moreover, they need to do it without lacking accuracy or safety conditions during the operation. In those situations, which involve an UAV flying close to different structures, surfaces, or

obstacles in general, the changes the flow field surrounding the vehicle make changes in the forces and torques developed by the rotors due to the aerodynamic effects.

Furthermore, these aerodynamic effects are in the core of this thesis. However, although these previous results have been considered as a good starting point to model the aerodynamic effects flying close to obstacles, this chapter goes beyond trying to model not only the aerodynamic effect over or under an obstacle, but also how this effect starts to be significant as a rotor approaches them. This means that, this chapter is not only evaluating the aerodynamic effect as a function of the distance between the obstacle and the propeller plane, but it is also taking into account the 2D relative position between this obstacle and the rotor.

In addition to this, the current trend of the UAVs applications is aiming to accomplish fully autonomous navigation and operation in industrial environments that are complex and varied ,such as oil and gas plants. Taking the lessons learned from the previous Chapters of this work into account, it is clear that those aerodynamic effects are not only a disturbance that we need to compensate. For instance, exploiting the ceiling effect, it is possible to enhance the performance of the robot improving the maximum flight time and the stability while inspecting. Then, the next step in this advanced aerodynamic modelling chapter consists of translating these two dimensional aerodynamic effect characterisations of the environment to develop aerodynamic effects maps of an environment with multiple obstacles that could be used by an intelligent planning or by control methods that exploit these aerodynamic effects. In order to properly model the scenario of an oil and gas plant, this chapter models the behaviour of rotors working close to tubular obstacles, like pipes,in which, these two dimensional modelling approaches are essential.

This chapter is structured as follows: Section 5.2 summarises the aerodynamic effect problem previously analysed in this thesis and presents a brief compilation of the previous one dimensional aerodynamic effect results. Section 5.3 is focused on the experimental modelling of these two dimensional aerodynamic effects which have not been previously studied and can arise in the typical scenarios of the aerial manipulation. Section 5.4 introduces the assumptions that have been taken into

consideration, as well as the mapping results of a sample scenario. Lastly, Section 5.5 is about the conclusion and future works of this research.

The content of this chapter is based on the following publications:

- Caballero, A., Sanchez-Cuevas, P. J., Béjar, M., Heredia, G., & Ollero, A. An aerodynamic extension for motion planning with dynamics awareness in aerial long-reach manipulators. International Journal of Aerospace Engineering
- Sanchez-Cuevas, P. J., Martín, V., Heredia, G., & Ollero, A. (2019, November). Aerodynamic Effects in Multirotors Flying Close to Obstacles: Modelling and Mapping. In Iberian Robotics conference (pp. 63-74). Springer, Cham.

5.2 Previous aerodynamic effect results

This section briefly summarises some of the different aerodynamic effects which have been previously studied by the author and the literature in general. These experimental results show how the thrust of a rotor changes working close to a ground, a ceiling or a wall surface. On the one hand, in the figure T_{IGE}/T_{OGE} is the relation between the thrust "In Ground Effect" and "Out Ground Effect"; T_{ICE}/T_{OCE} is the same but in terms of ceiling effect and, finally, T_{IWE}/T_{OWE} aims to model the changes that appears in wall effect. On the other hand, z/R is the distance from the rotor to the obstacle dimensionless with the rotor radius.

Ground effect The ground effect, which was presented in Section 2.5.1, is the most known aerodynamic effect and it is also the widest studied in the literature. This effect arises when an aerial platform flies over a flat surface which acts as a ground. In aerial robots, the ground effect does not only appear in the take-off and landing maneuver, but also when the aerial platform needs to fly over a surface, for example, during an inspection or manipulation task.

Ceiling effect The ceiling effect (Section 2.5.2), which is shown in Figure 5.1.b, appears when an aerial platform flies under a surface but very close to it. The results

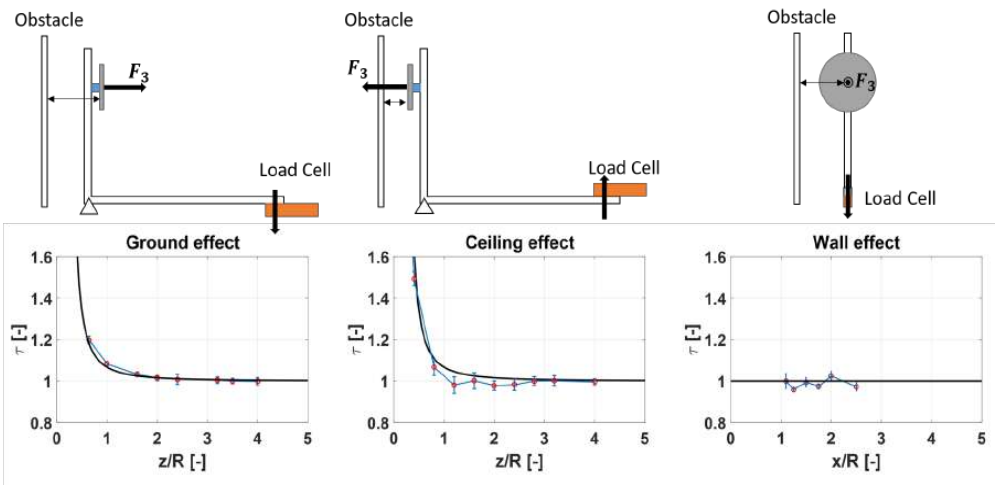

Figure 5.1: Characterisation of aerodynamic effects: ground, ceiling and wall effects. Experimental results (red dots and blue errorbars) and theoretical models (black curves).

of the Figure 5.1.b show that the behaviour of the ceiling effect is very abrupt and, unlike that of the ground effect which pushes the vehicle away from the obstacle, the ceiling effect pulls it towards it leading to an unsafe flight condition if it is not taken into account.

Wall effect Eventually, the experimental results of the 5.1.c show that the wall effect can be considered negligible following the assumption of the helicopters theory, which assumes that the flow is perpendicular to the rotor plane.

5.3 Two Dimensional Experimental Modelling

Due to the typical scenario in an oil and gas inspection, the application includes two different obstacles which are: flat surfaces, like grounds or ceilings and tubular obstacles, like pipes, which will be the ones taken into consideration in this work. Moreover, in contrast to the classical studies that only model the aerodynamic effect, like a rotor working under or over an obstacle, this chapter also models the transition

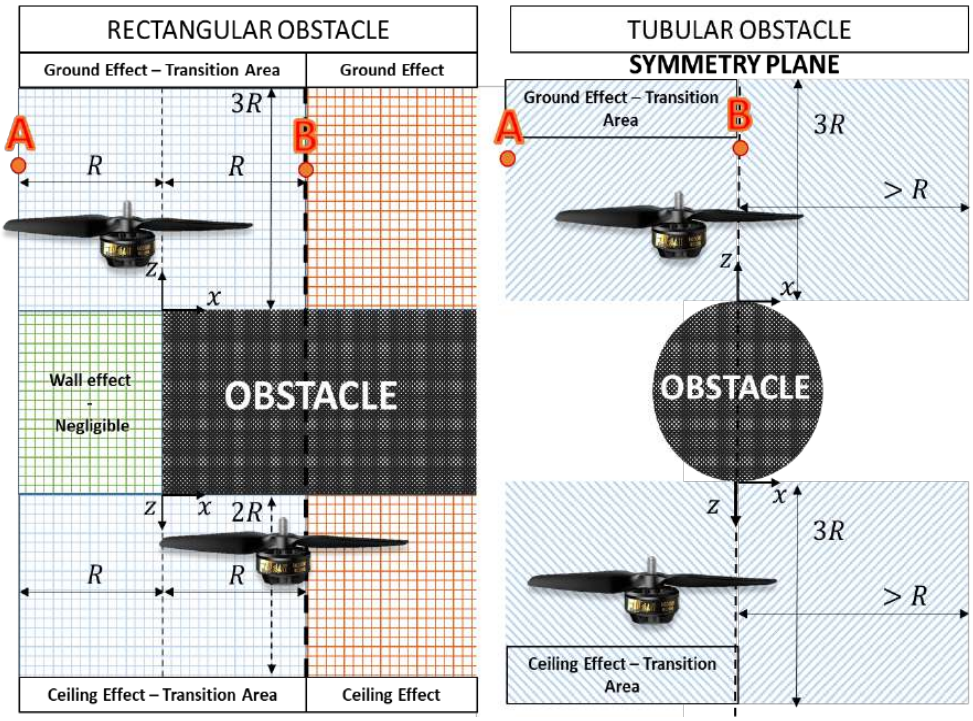

Figure 5.2: Test configuration and nomenclature

part when the rotor approaches the obstacle from the position where the the rotor is out of the effect to the one where it is fully affected by it. These results will be obtained through several experiments in a test stand, which is able to measure the thrust of the rotor. In the rectangular obstacle, the areas in which the different experiments are carried out are represented in the blue areas in Figure 5.2. This area starts when the center of the rotor placed at one radius of distance in the x axis of Figure 5.2 and the propeller are completely out of the obstacle (point A) and it finishes when the propeller is fully placed over the obstacle (point B). The experiments in the tubular obstacles are also accomplished in the blue areas taking the symmetry conditions of the problem into account.

5.3.1 Aerodynamic effect close to flat surfaces

Following the experimental procedure presented before, the ground and the ceiling effects have been studied taking the behaviour when the rotor approaches the obstacle into consideration. Since the results of these aerodynamic effects have been previously studied in the literature by the authors when the rotor is completely under the aerodynamic effect, it will be assumed that the effect follows the classical models because they have been validated previously. Thus, the theoretical model of the ground effect presented in [49] and the experimental one of [79] for the ceiling effect will be used to create the aerodynamic effect map. The expression of both models is presented as follows:

- Ground Effect: $\frac{T_{IGE}}{T_{OGE}} = \frac{1}{1-\frac{1}{16}(\frac{R}{z})^2}$
- Ceiling Effect: $\frac{T_{ICE}}{T_{OCE}} = \frac{1}{1-\frac{1}{a_1}(\frac{R}{a_2+z})^2}$

Where the acronyms ICE, OCE, IGE and OGE are "in/out ceiling/ground effect" respectively. R is the radius of the rotor and z is the distance betweeen the rotor plane to the obstacle as it is presented in Figure 5.1.In this case, we assume that the rotor is totally over the obstacle. The values of a_1 and a_2 were obtained through an experimental least square approach, in this case $a_1 = 6.924m^{-1}$ and $a_2 = 0.03782m$.

Lastly, the experimental results of Figure 5.3 show how the thrust changes when the rotor approaches the obstacle.

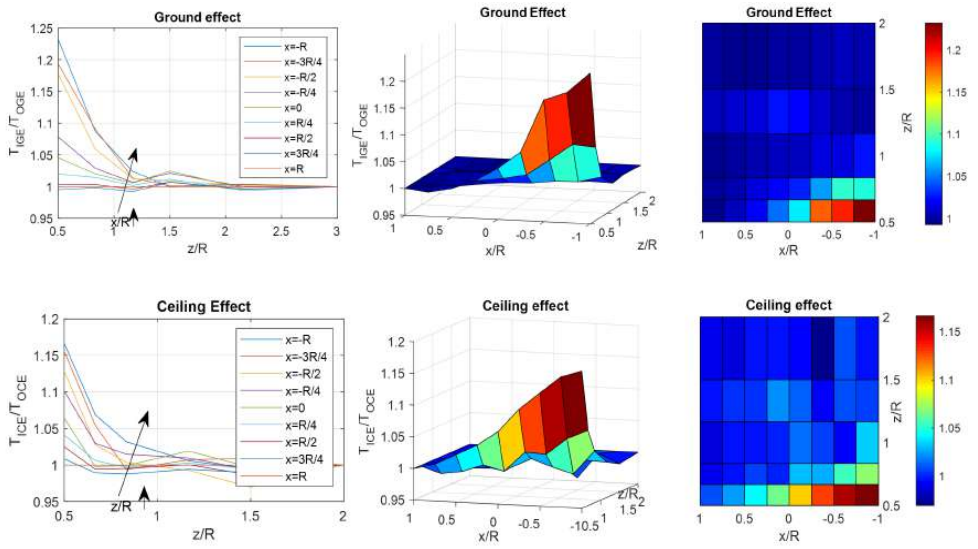

Figure 5.3: Ground and ceiling effect with a flat surface - experimental results

The results of Figure 5.3 show the differences in the aerodynamic effect when a rotor approaches ground or ceiling obstacles. These results show that, for the tested distances, the ground effect is stronger than the ceiling which is in line with the previous results of the literature ,as it is presented in Figure 5.1 in the previous section and in Chapter 2. This figure shows the evolution of the ground and the ceiling effect across the longitudinal coordinate but it also combines it with the vertical one.

5.4 Aerodynamic Mapping

Once the aerodynamic effects close to flat surfaces and tubes have been experimentally tested, the next step is to combine them in an aerodynamic map, which could be used in a future to improve the control strategies or the planning methods taking this aerodynamic effect map into account.

5.4.1 Assumptions

This section is focused on defining the limits of the flying area and on establishing the assumptions when the rotor is working close to different obstacles. These assumptions are established in terms of defining the flyable area during the operation and of working out how to solve the problem in the points which are under the influence of more than one obstacle.

Flyable area Figure 5.4 shows the flyable areas close to a flat/rectangular obstacle and a tubular one. This area establishes the limits of the map and envelopes the operation area of the aerial platform.

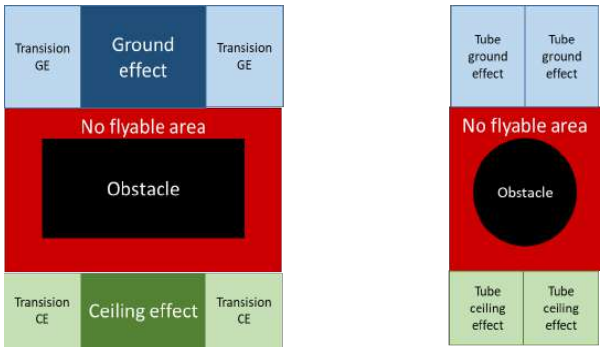

Figure 5.4: Flyable area detail and forbidden zones. Note that, in both cases we have symmetrical transition effects.

The map around these obstacles will be modelled as it is shown in Figure 5.5.

The flat surface where the value of the non-dimensional thrust is 0.95 is out of the flying area but it has been defined with this value to avoid infinite elements in the plot.

Obstacle overlapping The assumption to model the aerodynamic effect in the points of the map which are affected by more than one obstacle is that it is possible to apply the principle of superposition. However, it is assumed that the superposition method is no longer valid if one obstacle is in the shadow of another one. This is clearly explained in Figure 5.6, where the red area shows the influence area of the

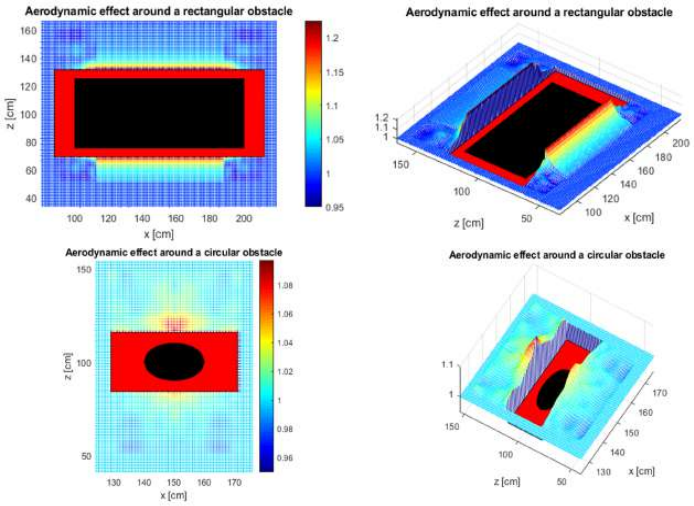

Figure 5.5: Sample of aerodynamic effect close to a rectangular obstacle (left) and a pipe (right)

obstacle (a) and the blue area shows the influence of the obstacle (b). In the section in purple, it is where the principle of superposition is applicable and the grey zone is a shadow area and it shows an area in which the aerodynamic effect of the obstacle (a) is considered blocked by the presence of the obstacle (b).

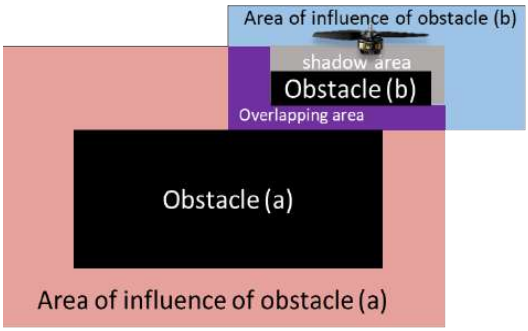

Figure 5.6: Obstacle overlapping and shadows conditions.

5.4.2 Results

Lastly, this section presents the results of different aerodynamic maps in which the changes of the thrust due to the influence of the obstacles are represented. Figures 5.7, 5.8 and 5.9 show the results in three different scenarios which can be used later to design different planning or control techniques.

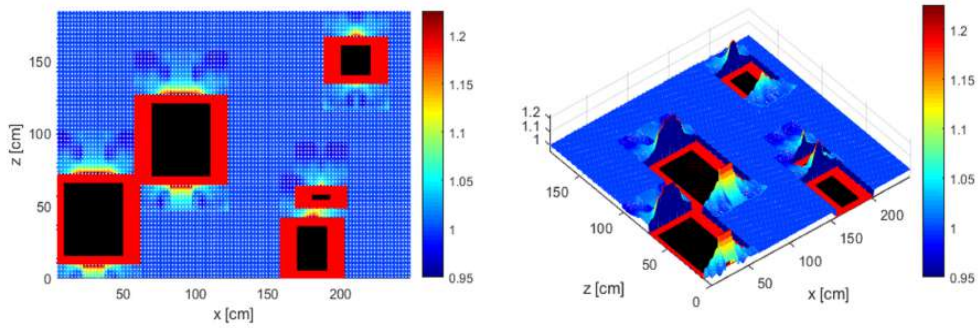

Figure 5.7: Aerodynamic effect map with rectangular obstacles

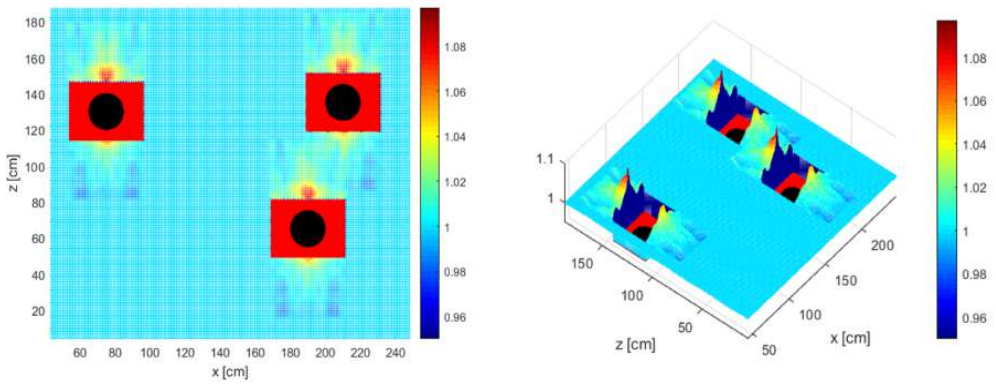

Figure 5.8: Aerodynamic effect map with tubular obstacles

These results evidence that this kind of aerodynamic map can open several research lines in which the aerodynamic disturbance does not take into account as a punctual problem but a environmental one. In this context, aerodynamic awareness planners or controllers could be used to navigate in a complex and narrow environment with

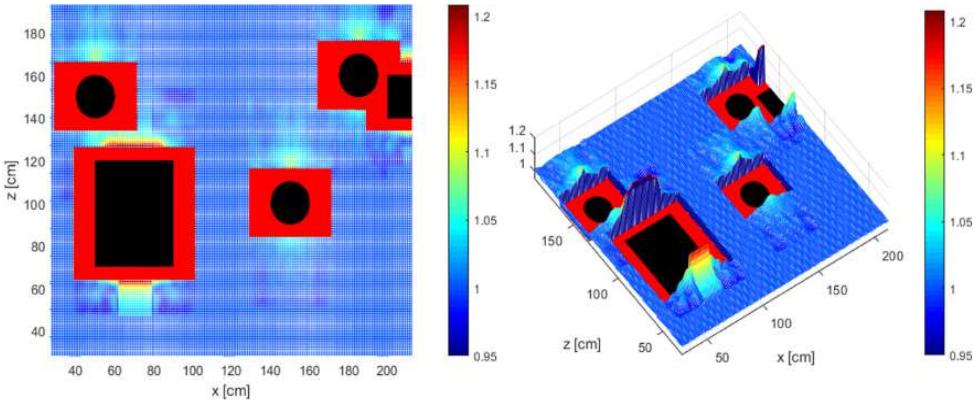

Figure 5.9: Aerodynamic effect map with rectangular and tubular obstacles

several obstacles. For instance, in some cases, it could be convenient to move along a constrained environment if this help the multirotor to lift their weight thanks to the aerodynamic effects. That is similar to the case of the bridge presented in Chapter 4, where we use the ceiling to stabilise the platform and increase their maximum flight time, but in a general way in which we can navigate through the environment to exploit the aerodynamic effect in our benefit.

5.5 Conclusions

This chapter has presented a new approach to the modelling of the aerodynamic effects that can arise during the operation of an UAV flying close to obstacles in oil and gas plants. This approach consists of creating an aerodynamic effects map which links the relative position of the vehicle with the aerodynamic effect that the environment produces in this point.

The different aerodynamic effects have been independently studied and the different assumptions about the areas under the influence of more than one obstacle are also presented.

The future work related to this research will be focused on the application of this map to design different control techniques or planning methods which take them into

account the aerodynamic effects on the aerial vehicle to improve its behavior or to optimise the use of resources, like the power or time consumption during the operation. This kind of map has a direct application in the direction of the actual application of the UAV in the Inspection and Maintenance of oil and gas industries.

Actually, the appendix C presents results of collaboration work with Álvaro Caballero, (PhD Student of the University of Seville) in which this kind of aerodynamic maps is included in an aerodynamic awareness planning method [84].

Chapter 6

Conclusions and Future Works

> Try not to become a man of success.
> Rather become a man of value.
>
> Albert Einstein

6.1 Conclusion

Aerodynamic effects take part in most of the applications of aerial manipulation which are ranging from grasping an object to inspect a surface through establishing a physical interaction. Those effects are higher as the robot is closer to different elements of the environment, where, the needs of maintaining a high accuracy and safe conditions are essential.

Those reasons motivated the work developed in this thesis. Throughout it, several studies about different aerodynamic effects have been presented, actually, different solutions to deal with it while flying have been proposed.

At the beginning of this work, the background about this aerodynamic phenomenon in aerial manipulator was not widely extended (Section 1.3). In this way, this research started to look into a field with small background compared to other topics that have been widely studied by the research community. The published contributions have helped then to improve the knowledge about this topic. To sum up, this thesis has presented an analysis of the aerodynamic effects that can arise in typical aerial

manipulation applications. In addition, it has thoroughly modelled the aerodynamic effect that appears in two cases of use in the framework of two European Projects, AEROARMS [73] and AEROBI [33]. In both cases, different control strategies have been presented and tested in real flights. After that, and following the research lines of new European Projects, like HYFLIERS, RESIST, AERIAL-CORE and PILOTING, the author intends to present a paradigm shift in terms of how to model those aerodynamic effects, changing the perspective of modelling those effects to a complexer one produced by the environment. In this way, it is possible now to generate aerodynamic maps which can be exploited in the controller or the planning (Appendix C) strategies to fly in a more efficient and safer way. Despite of the fact that the document has been specifically focused on the study of these aerodynamic effects, in this thesis, the author wants to remark the experimental part and the efforts dedicated to it.

To sum up, this thesis will concluded with the following key aspects:

- Aerodynamic effects affect significantly in those operations that require the robot flies very close to different obstacles.

- Although it is possible to develop a general model that approximate different aerodynamic effects, it is extremely difficult to solve the complete problem because the specific geometry of the robot takes part in the aerodynamic effect. That means that this kind of disturbances will affect each platform in a different way.

- Those effects can be use to improve the performance of an specific operation as Chapter 4 have shown with the ceiling effect.

- The knowledge of the aerodynamic effect could help to exploit aerial robot in difficult to access and small environments.

- This thesis has helped and contributed to advance and improve the knowledge about the aerodynamic effect in aerial manipulators.

6.2 Future Works

6.2.1 Complete aerodynamic awareness while operating

In the future, the main goal of the aerial manipulator working close to different obstacles will be the complete aerodynamic awareness while operating. For instance, a clear sample that has received less attention is the aerodynamic effects that can appear in the robotic arm by the presence of airflow developed by the propellers. However, this effect is not negligible, especially if the arm is compliant and is able to admit certain deformations while operating.

Our experience in aerial manipulation applications pushed us to look into this aerodynamic effect as the disturbance does not only arise in the aerial platform, but it also distorts the robotic arm. The first effect is caused by the arm which acts like an obstacle and obstructs the development of the propeller wake changing the aerodynamic flow field and, consequently, the force and torques developed by the rotor. The second one is due to the forces that the fluid exerts against the robotic arm ,which can produce two different effects depending on the characteristics of the arm joints and the geometrical design design of it. In rigid joints which do not protect the servo actuators against impacts and overloads, the drag that appears due to the movement of the propeller could force the servo beyond its range causing a complete failure of the joint. This is one of the most important drawbacks of using rigid joints in aerial manipulation. However, in terms of the aerodynamic effect, a compliant joint is also affected in an important way. Thus, although the flexible link partially protects the actuator and solves this problem, the aerodynamic forces will deflect these joints causing a deformation and losing accuracy in the manipulation.

In addition to this, it is important to remark that the geometrical design of the arm is relevant from the aerodynamic point of view. It is obvious that if the arm acts like a blunt body, the drag that it is going to support is much greater than being a streamlined body.

Figure 6.1 illustrates this effect from an schematic point of view. $F_{A_{arm}}$ and $T_{A_{arm}}$ are the forces and torques that the arm is suffering due to the presence of the airflow impacting on it. $F_{A_{rotor}}$ and $T_{A_{rotor}}$ are the forces and torques that appears in the

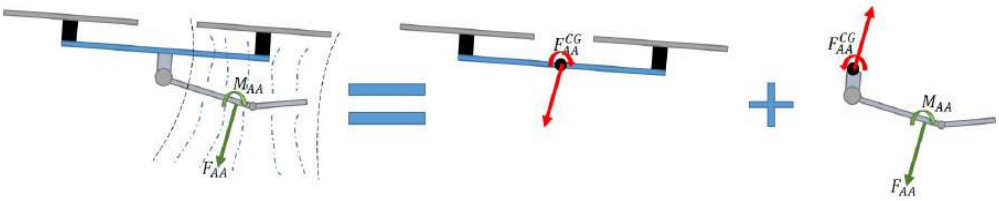

Figure 6.1: Aerodynamic effect in the robotic arm

rotors die to the disturbance produced by the arm. These forces and torques are usually considered negligible. However, the forces that act in the manipulator produce two important effects that must be taken into account to be able to carry out aerial manipulation operations with enough accuracy. Firstly, the position of the arm is going to depend on the airflow exerted by the rotors which ,in turn ,depend on the rotational velocity of the rotors ω, $F_{A_{arm}} = f(\omega)$ and $M_{A_{arm}} = f(\omega)$. Secondly, the force suffered by the arm will be transmitted to the multirotor, since they are in a common body, producing an undesirable disturbance.

This effect as well as those presented above are a challenge in aerial manipulation that must be deeply studied to be able to develop robust and reliable aerial manipulators which can be included in the industries of the future.

6.2.2 Aerodynamic effect in closed spaces

Several applications will require using multirotor in confined spaces, for instance, for inspecting vessels or tunnels among others. In those environment the aerodynamic effect could have an important impact in order to guarantee the stability of the robot while flying. Aerodynamic effects, then, are expected to be higher in those kind of scenarios where all the effect will be superimposed at the same time and additional aerodynamic effects due to the re-circulation, could accentuate the impact in the dynamic of the robot (see Figure 6.2).

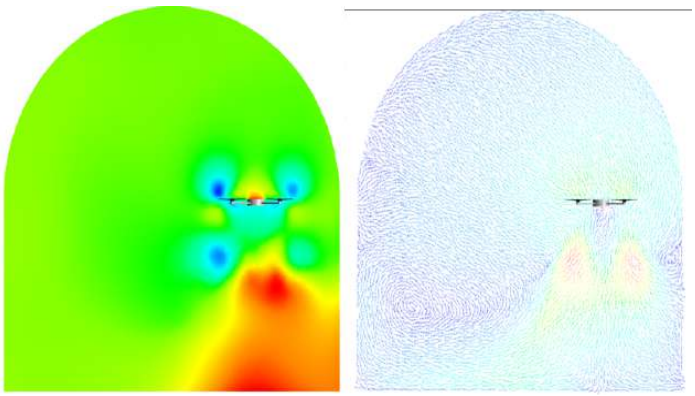

Figure 6.2: Aerodynamic effect inside of a tunnel

Appendix A

Classical dynamic model of an aerial manipulator

This appendix presents and details the typical approaches to derive the dynamic model of a body. These are the Lagrange-Euler method and the Newton-Euler formulation. Although these two solutions are equivalent, the procedure to follow differs in both methods and the resulting equations have different properties in terms of efficiency, computational cost and so on. In other words, while in the Lagrange-Euler formalism it is possible to obtain the whole dynamic model in a symbolic matrix form using the Newton-Euler recursive formulation, the resulting model is more computationally efficient.

A.1 Euler-Lagrange Formulation

Defining $\boldsymbol{\xi} = [\xi_1 \quad ... \quad \xi_N]^T \in \mathbf{R}^N$ as the set of generalised coordinates that describe the configuration of our aerial vehicle as $\boldsymbol{\xi} = [\boldsymbol{p} \quad \boldsymbol{q} \quad \boldsymbol{\gamma}]^T$. Where $\boldsymbol{p} = [x \quad y \quad z]^T$ represents the position of the robot; $\boldsymbol{q} = [\phi \quad \theta \quad \psi]^T$ is the attitude and; lastly, $\boldsymbol{\gamma} = [\gamma_1 \quad ...\gamma_N]$ represents the joints of the robotic arm of the aerial manipulator. Thus, the next step is to calculate the Lagrangian, $L(\xi, \dot{\xi})$, which is obtained as the difference between the kinetic $K(\boldsymbol{\xi}, \dot{\boldsymbol{\xi}})$ and potential energies $P(\boldsymbol{\xi})$ of the system.

$$L(\boldsymbol{\xi}, \dot{\boldsymbol{\xi}}) = K(\boldsymbol{\xi}, \dot{\boldsymbol{\xi}}) - P(\boldsymbol{\xi}) \tag{A.1}$$

Where, the kinematic energy, $K(\xi, \dot{\xi})$, is calculated as the sum of the kinetic energies of the body as follows:

$$K = \frac{1}{2} \sum_{i=1}^{N_n} (v_i^b) \boldsymbol{M_i} (v_i^b) \tag{A.2}$$

where M_i is the generalised matrix of inertia and v_i^b is the velocity of the body i, $v_i^b = \sum J_i^b \dot{\xi}_i$. Therefore,

$$\boldsymbol{M}(\boldsymbol{\xi}) = \sum_{i=1}^{N} \boldsymbol{J_i}^b \boldsymbol{M_i} \boldsymbol{J_i}^b \tag{A.3}$$

The total potential energy must be calculated to complete the derivation of the Lagrangian.

$$P(\xi) = \sum_{i=1}^{N} m_i g_i h_i(\xi) \tag{A.4}$$

Then, the equations of the motion are calculated by the Lagrange equations expressed in A.5 in which Γ_i is the external forces acting on the i generalised coordinate.

$$\frac{d}{dt} \frac{\partial L(\boldsymbol{\xi}, \dot{\boldsymbol{\xi}})}{\partial \dot{\xi}_i} - \frac{\partial L(\boldsymbol{\xi}, \dot{\boldsymbol{\xi}})}{\partial \xi_i} = \Gamma_i, \quad i = 1, ..., N \tag{A.5}$$

Substituting the previous equation into this one, the dynamic model of the system can be written as follows:

$$\boldsymbol{M}(\boldsymbol{\xi}) \ddot{\boldsymbol{\xi}} + \boldsymbol{C}(\boldsymbol{\xi}, \dot{\boldsymbol{\xi}}) \dot{\boldsymbol{\xi}} + \boldsymbol{G}(\boldsymbol{\xi}) = \boldsymbol{\Gamma} \tag{A.6}$$

where, $\boldsymbol{M}$ is the generalised inertia matrix which directly depends on the geometry and masses of the body, $\boldsymbol{C}$ represents the centrifugal and Coriolis terms, which can be derived through the inertia matrix, $C_{ij} = \frac{1}{2} \sum_{i=1}^{N} (\frac{\partial M_i j}{\partial \xi_i} + \frac{\partial M_i k}{\partial \xi_i} + \frac{\partial M_j k}{\partial \xi_i}) \dot{\xi}_i$, and last,

$\boldsymbol{G}$ is the gravity component, which can be directly obtained from the potential energy, $G_i = \frac{\partial P}{\partial \xi_i}$.

A.2 Newton-Euler Formulation

In the Lagrangian Formalism, the system dynamics is derived using the Lagrangian function of the whole system, which means calculating the difference between the kinetic and potential energy. In contrast, the Newton-Euler Formalism is based on the balance of forces and moments acting on a body of the system. This allows to obtain the system dynamics following two recursive steps. Firstly, the velocities and accelerations of each body are calculated through an outward recursion from the fixed frame to each system link. Then, the forces required to produce this acceleration are computed using the Newton-Euler equations. In each link of a kinematic tree, the velocity and acceleration are given by:

$$v_i = v_{i-1} + \boldsymbol{\Phi_i}\dot{\xi}_i \quad (v_0 = 0) a_i = a_{i-1} + \boldsymbol{\Phi_i}\ddot{\xi}_i + \dot{\boldsymbol{\Phi}}_{\boldsymbol{i}}\dot{\xi}_i \quad (a_0 = -a_g) \tag{A.7}$$

Then, calculating the forces required to generate these accelerations as:

$$f_i^a = I_i a_i + v_i \times I_i v_i - f_i^{ext} \tag{A.8}$$

The next step is the inward recursion, in which the force balance equation of each body is used to compute the spatial force across the joints from the forces/torques acting on the bodies. Then, iterating from NB to 1 we have

$$f_i = f_i^a - f_{ext} + \sum_{j \in c(i)} f_j \tau_i = \boldsymbol{\Phi}_i^T f_i \tag{A.9}$$

More details of the equations and the recursive algorithm can be found in [104], [105] and [106].

Appendix B

Linearized potential aerodynamics

In fluid dynamics, a potential flow is described by means of a velocity potential, $\hat{I}_{|}^{|}$, being a function of the space and time, $\Phi = \Phi(x, y, z, t)$. The flow velocity $\boldsymbol{v}$ is a vector field equal to the gradient, ∇, of the velocity potential, Φ.

$$\boldsymbol{v} = \nabla\Phi \tag{B.1}$$

Following this assumption, which is valid for the fluid in the outer region of boundary layer, the momentum equation (B.2) can be expressed as (B.3).

$$\frac{D\boldsymbol{v}}{Dt} = \frac{\partial \boldsymbol{v}}{\partial t + \nabla(\frac{\boldsymbol{v}^2}{2})} - \boldsymbol{v} \times \omega = -\frac{1}{\rho}\nabla p \tag{B.2}$$

$$\frac{\partial \nabla\phi}{\partial t} + \nabla(\frac{|\nabla\phi|^2}{2}) + \frac{1}{\rho}\nabla p = 0 \tag{B.3}$$

Taking into account that the enthalpy is defined as $h = e + p/\rho$, the equation can be expressed as:

$$\nabla[\frac{\partial\phi}{\partial t} + \frac{|\nabla\phi|^2}{2} + h] = 0 \tag{B.4}$$

Using the definition of the specific heat, $h = CpT = \frac{\gamma}{\gamma-1}\frac{p}{\rho}$ and using the definition of the speed of sound $a^2 = \frac{\partial p}{\rho}$, the momentum equation can be written as:

$$\frac{\partial \phi}{\partial t} + \frac{|\nabla \phi|^2}{2} + \frac{a^2}{\gamma - 1} = C(t) \tag{B.5}$$

Then, assuming that problem is stationary ($\partial/\partial t \equiv 0$) and following the continuity expression B.6 including that $v = \nabla\phi$, the following one is obtained:

$$v\frac{\nabla \rho}{\rho} + \nabla v = \nabla\phi\nabla[\ln \rho] + \nabla^2\phi = 0 \tag{B.6}$$

Moreover, since the movement is homentropic:

$$\frac{a^2}{a_{\text{inf}}^2} = \frac{p}{p_{\text{inf}}}\frac{\rho_{\text{inf}}}{\rho} = (\frac{\rho}{\rho_{\text{inf}}})^{(\gamma-1)} \tag{B.7}$$

Taking the logarithm of (B.7) and substituting in (B.6), it is obtained that:

$$\frac{\nabla\phi}{\gamma - 1}\frac{\nabla a^2}{a^2} + \nabla^2\phi = 0 \tag{B.8}$$

Expressing a as a function of ϕ through the Euler-Bernouilli expression.

$$\frac{a^2}{\gamma - 1} = C - \frac{|\nabla\phi|^2}{2} \Leftrightarrow \nabla(\frac{a^2}{\gamma - 1}) = \frac{\nabla a^2}{\gamma - 1} = \nabla[-\frac{|\nabla\phi|^2}{2}] \tag{B.9}$$

The equation that the potential of velocities must fulfill is:

$$-\frac{1}{a^2}\nabla\phi\nabla[\frac{|\nabla\phi|^2}{2}] + \nabla^2\phi = 0 \tag{B.10}$$

Then, assuming that:

$$O(\nabla^2\phi) \sim \frac{\nabla\phi}{c_0^2} \tag{B.11}$$

$$O(\frac{1}{a^2}v\nabla[\frac{v^2}{2}] \sim \frac{U_{inf}^2}{a^2}\frac{\Delta\phi}{c_0^2} \tag{B.12}$$

it is concluded that:

$$\frac{O(\frac{1}{a^2}v\nabla[\frac{v^2}{2}])}{O(\nabla^2\phi)} \sim \frac{U_{\text{inf}}^2}{a^2} \sim M^2 \tag{B.13}$$

where M is the Mach number, which is the relation between the ratio of flow velocity and the local speed of sound.

Then, in cases in which $M_{\text{inf}}^2 << 1$, we can conclude with relative errors of the same order of magnitude that the potential of velocities must address:

$$\nabla^2 \phi = 0 \tag{B.14}$$

It is clear now that the potential flow previously used in chapter 2 fulfills the assumptions of the linearised potential aerodynamics.

Appendix C

Aerodynamic awareness planning in aerial long-reach manipulators

This appendix is the result of a collaborative work between AÍvaro Caballero Goḿez (developer of the planning method) and the author of this thesis (contributing with the aerodynamic characterisation), in which the inclusion of aerodynamics awareness was proposed within the motion planning process. This is a brief description of this new aerodynamic planning approach using the results presented in Chapter 5. The complete version of this work has been published in the International Journal of Aerospace Engineering.

The planning problem in aerial manipulation or aerial inspection operations arise according to the complexity of the task to be carried out. In fact, numerous industrial applications usually require flying in cluttered environments below a line of sight, such as flying in a refinery or a chemical plant, in the middle of a wind field and close to big infrastructures, among others. In those situations, planning methods become essential in order to guarantee safe conditions during the operations.

There exists some contributions like [107] that usually assume a strong simplification by addressing the planning problem decoupled from the control techniques and other external effects. In contrast, Caballero et al. presented in [108], [109] and [110] a novel algorithm that considers the aerial platform and the manipulators jointly within the planning operation. This work intends to extend those contributions expanding

the planning method not only to consider the dynamics of the controlled system but also the influence of the aerodynamic effect which will arise when flying close to the different elements of the environment.

In this way, it was proposed the realistic application of a bridge inspection as a use case to evaluate the new proposed motion planner. With the means currently available for this, the application scenario of crack detection in reinforced concrete bridges requires visual inspection by qualified human operators.

C.1 The aerial long-reach manipulator for multidirectional inspection

The proposed Aerial Robotic System for Long-Reach (see Figure C.1) consists of a multirotor and a robotic long-reach arm whose special integration with the aerial platform enables 360° rotation within the vertical plane that coincides with the center of mass of the multirotor. In this way, it has multidirectional capabilities and a long reach to increase the safe conditions during the operation.

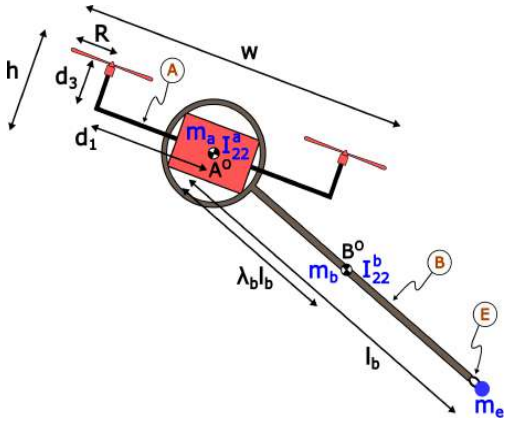

Figure C.1: Aerial Robotic System for Long-Reach Manipulation (ARS-LRM). Geometry and mass distribution.

Following the Kane's method and defining the variables selected as a system of generalised coordinates in which q_1 is the longitudinal and q_3 is the vertical positions

of the UAV center of mass A^O in the inertial reference frame N, the multirotor pitch angle q_5 and the joint angle of the robotic arm q_7.

$$\begin{bmatrix} \dot{q}_1 & \dot{q}_3 & \dot{q}_5 & \dot{q}_7 \end{bmatrix}^T = \begin{bmatrix} u_1 & u_3 & u_5 & u_7 \end{bmatrix}^T \tag{C.1}$$

$$\boldsymbol{A} = \begin{bmatrix} \dot{u}_1 & \dot{u}_2 & \dot{u}_3 & \dot{u}_4 \end{bmatrix}^T \boldsymbol{B} \tag{C.2}$$

Regarding the multirotor, the control scheme is inspired by [111] and consists of linearising the system through model inversion and applying PID control laws to the resultant dynamics as the one presented in Figure C.2 (left), where D_{13}^{-1}, K_5^{-1} and D_5^{-1} blocks represent, respectively, the inversions of the translational dynamics, rotational kinematics and rotational dynamics. The control strategy selected for the robotic arm is again based on the linearisation through model inversion and PID control, which yields a non-linear control law capable of commanding the joint position of the manipulator (see Figure C.2 (right)).

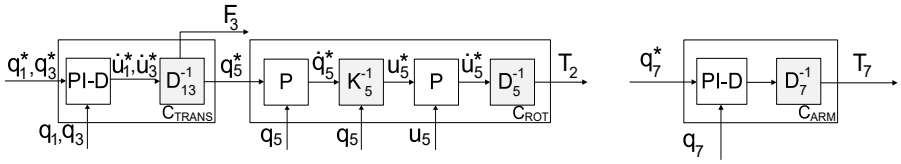

Figure C.2: Block diagrams of the UAV controller (left) and the arm controller (right).

C.2 Motion planner with dynamics and aerodynamics awareness

Similar to the dynamics awareness approach, the principle of operation of the aerodynamics awareness mechanism is based on ensuring collision-free trajectories through the closed-loop simulation of the controlled ARS-LRM system. However, in this new approach, not only the dynamics of the system has been considered for the expansion of the search tree, but also its aerodynamics. Figure C.3 (left) schematises the operation

basis of the enhanced algorithm (MP-ARM-ADA) in contrast with the MP-ARM and MP-ARM-DA versions. In this figure, the difference between the trajectories computed by MP-ARM-DA and MP-ARM-ADA is the additional safety distance with respect to the grey surface that aerodynamics awareness suggests. Otherwise, the controlled system would not be able to compensate for the ceiling effect and might provoke a collision. On the other hand, Figure C.3 (right) depicts the complete closed-loop scheme required to perform the simulations that give support to the aerodynamics awareness concept. As can be seen, the MP-ARM-ADA algorithm makes use of an aerodynamic model whose input is given by the control signals commanded by the controller ($F_{3,OAE}, T_{2,OAE}$) in terms of the corresponding PWM signals and whose output are the force and torque that actually govern the movement of the system as a consequence of aerodynamic effects ($F_{3,IAE}, T_{2,IAE}$).

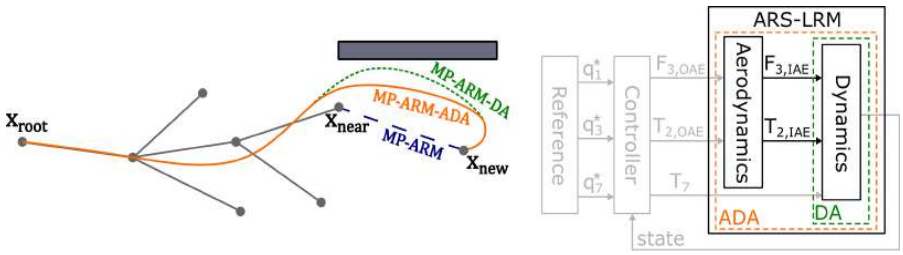

Figure C.3: Operation basis of the MP-ARM-ADA algorithm.

C.3 Application scenario

As it was stated before, the case of use proposed in this work is the bridge inspection. The scenario of the case of use is presented in Figure C.4 (left). In this scenario, the system has to perform a visual inspection of the junction point between the deck and one pillar of the bridge (marked with a red point in the figure). To this end, a visual camera will be integrated as end effector in the long-reach arm of the ARS-LRM system. The aerodynamic challenges of this scenario arise because the most efficient trajectories for the inspection task under consideration demand that the ARS-LRM system flies close to the bridge surfaces, where the aerodynamic effects

are significant. In order to characterise these effects, 3D map of aerodynamic effects was computed following the basis established in chapter 5 but particularized to the application scenario proposed in this section (see Figure C.5).

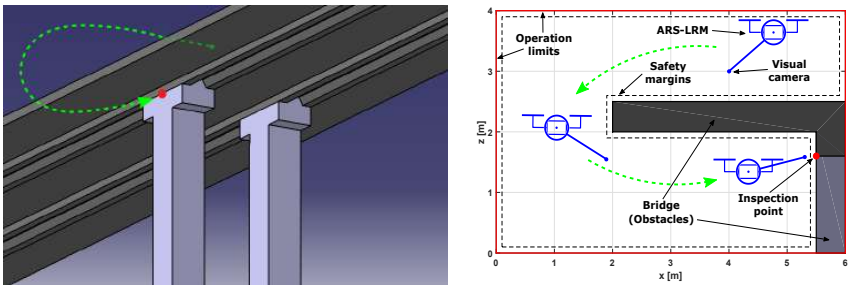

Figure C.4: Application scenario given by a bridge inspection task.

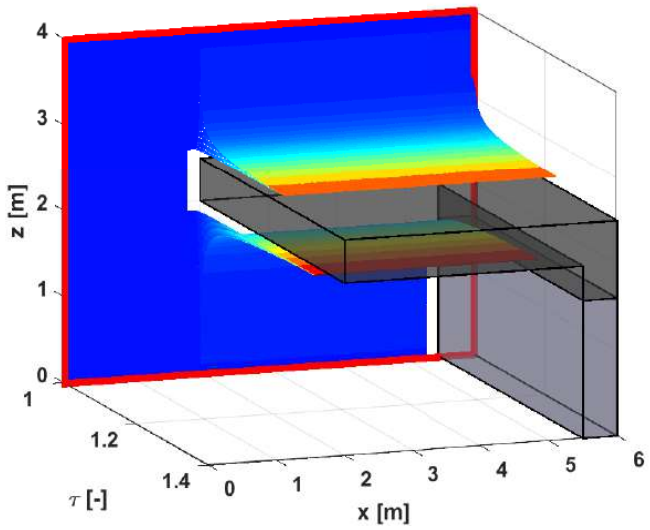

Figure C.5: 3D map of aerodynamic effects for the bridge scenario.

C.4 Simulation results

In this section, the planning method proposed is validated through simulating the behaviour in the selected environment.

These results are collected in Figures C.6 and C.7. Those results show how the aerodynamic awareness motion planner is able to prevent the collision with the environment at the same time that it takes advantage of the long-reach capabilities.

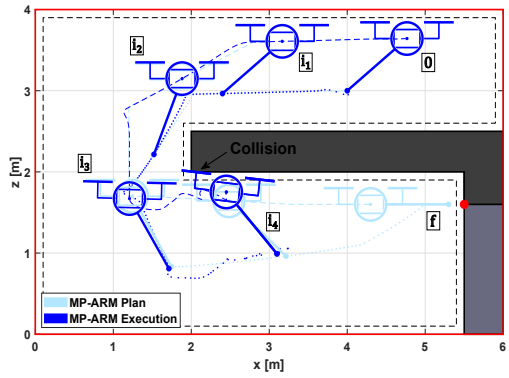

Figure C.6: Snapshot diagram corresponding to the closed-loop execution (dark blue) of the trajectory planned with the MP-ARM algorithm (light blue).

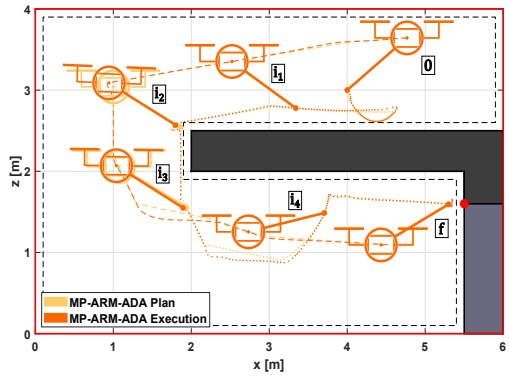

Figure C.7: Snapshot diagram corresponding to the closed-loop execution (dark orange) of the trajectory planned with the MP-ARM-ADA algorithm (light orange).

Bibliography

[1] Kimon P Valavanis and George J Vachtsevanos. *Handbook of unmanned aerial vehicles*. Springer, 2015.

[2] AMAZON. Amazon prime air. http://www.amazon.com/b?node=8037720011, 2016. Accessed: 2020-08-20.

[3] DHL. Dhl uav logistics. https://www.dhl.com/global-en/home/insights-and-innovation/thought-leadership/trend-reports/unmanned-aerial-vehicles.html, 2019. Accessed: 2020-08-20.

[4] DJI. Dji. https://www.dji.com/, 2006. Accessed: 2020-08-20.

[5] senseFly. sensefly. https://www.sensefly.com/, 2009. Accessed: 2020-08-20.

[6] WinterGreen. Drones market shares, strategies, and forecasts. https://www.wintergreenresearch.com/drones, 2006. Accessed: 2020-08-20.

[7] FORCETEC. Force technology's drone solution provides you with fast and thorough inspection of bridges, power lines, buildings and rooftops. https://forcetechnology.com/en/services/drone-inspection-of-power-lines-and-civil-infrastructure, 2018. Accessed: 2020-08-20.

[8] FORCETEC. Drone inspection makes it possible to access areas of oil and gas constructions that otherwise may pose health, safety and environmental risks in a fast and safe way. https://forcetechnology.com/en/

services/drone-inspection-offshore-oil-gas-constructions, 2019. Accessed: 2020-08-20.

[9] ATT. When cows fly: At&t sending lte signals from drones. http://about.att.com/innovationblog/cows_fly, 2017. Accessed: 2020-08-20.

[10] Walmart. Wal-mart testing drones in warehouses to manage inventory. https://apnews.com/ee9b77dba1a5460a91fef2842ccb8955/wal-mart-testing-drones-warehouses-manage-inventory, 2016. Accessed: 2020-08-20.

[11] GoldMan S. Drones, reporting for work. https://www.goldmansachs.com/insights/technology-driving-innovation/drones/, 2016. Accessed: 2020-08-20.

[12] Anibal Ollero and Bruno Siciliano. *Aerial Robotic Manipulation: Research, Development and Applications*, volume 129. Springer, 2019.

[13] Matko Orsag, Christopher Korpela, Paul Oh, Stjepan Bogdan, and Anibal Ollero. *Aerial Manipulation*. Springer, 2018.

[14] Fabio Ruggiero, Vincenzo Lippiello, and Anibal Ollero. Aerial manipulation: A literature review. *IEEE Robotics and Automation Letters*, 3(3):1957–1964, 2018.

[15] AE Jimenez-Cano, Jesús Martin, Guillermo Heredia, Aníbal Ollero, and R Cano. Control of an aerial robot with multi-link arm for assembly tasks. In *2013 IEEE International Conference on Robotics and Automation*, pages 4916–4921. IEEE, 2013.

[16] R Cano, C Pérez, F Pruano, A Ollero, and G Heredia. Mechanical design of a 6-dof aerial manipulator for assembling bar structures using uavs. In *2nd RED-UAS 2013 workshop on research, education and development of unmanned aerial systems*, volume 218, 2013.

[17] Carmine Dario Bellicoso, Luca Rosario Buonocore, Vincenzo Lippiello, and Bruno Siciliano. Design, modeling and control of a 5-dof light-weight robot arm

for aerial manipulation. In *2015 23rd Mediterranean Conference on Control and Automation (MED)*, pages 853–858. IEEE, 2015.

[18] Angel Santamaria-Navarro, Patrick Grosch, Vincenzo Lippiello, Joan Solà, and Juan Andrade-Cetto. Uncalibrated visual servo for unmanned aerial manipulation. accepted for publication in the ieee. *ASME Transactions on Mechatronics. To appear*, 2017.

[19] Mina Kamel, Kostas Alexis, and Roland Siegwart. Design and modeling of dexterous aerial manipulator. In *2016 IEEE/RSJ International Conference on Intelligent Robots and Systems (IROS)*, pages 4870–4876. IEEE, 2016.

[20] Alejandro Suarez, Antonio Enrique Jimenez-Cano, Victor Manuel Vega, Guillermo Heredia, Angel Rodriguez-Castaño, and Anibal Ollero. Design of a lightweight dual arm system for aerial manipulation. *Mechatronics*, 50:30–44, 2018.

[21] Matteo Fumagalli, Roberto Naldi, Alessandro Macchelli, Francesco Forte, Arvid QL Keemink, Stefano Stramigioli, Raffaella Carloni, and Lorenzo Marconi. Developing an aerial manipulator prototype: Physical interaction with the environment. *IEEE robotics & automation magazine*, 21(3):41–50, 2014.

[22] Kelly Steich, Mina Kamel, Paul Beardsley, Martin K Obrist, Roland Siegwart, and Thibault Lachat. Tree cavity inspection using aerial robots. In *2016 IEEE/RSJ International Conference on Intelligent Robots and Systems (IROS)*, pages 4856–4862. IEEE, 2016.

[23] Salua Hamaza, Ioannis Georgilas, Manuel J Fernandez, Pedro J Sanchez-Cuevas, Thomas Richardson, Guillermo Heredia, and Anibal Ollero. Sensor installation and retrieval operations using an unmanned aerial manipulator. *IEEE Robotics and Automation Letters*, 2019.

[24] T Bartelds, Alex Capra, Salua Hamaza, Stefano Stramigioli, and Matteo Fumagalli. Compliant aerial manipulators: Toward a new generation of aerial robotic workers. *IEEE Robotics and Automation Letters*, 1(1):477–483, 2016.

[25] Marco Tognon, Hermes A Tello Chávez, Enrico Gasparin, Quentin Sablé, Davide Bicego, Anthony Mallet, Marc Lany, Gilles Santi, Bernard Revaz, Juan Cortés, et al. A truly-redundant aerial manipulator system with application to push-and-slide inspection in industrial plants. *IEEE Robotics and Automation Letters*, 4(2):1846–1851, 2019.

[26] Marco Tognon and Antonio Franchi. Omnidirectional aerial vehicles with unidirectional thrusters: Theory, optimal design, and control. *IEEE Robotics and Automation Letters*, 3(3):2277–2282, 2018.

[27] Markus Ryll, Davide Bicego, and Antonio Franchi. Modeling and control of fast-hex: a fully-actuated by synchronized-tilting hexarotor. In *2016 IEEE/RSJ International Conference on Intelligent Robots and Systems (IROS)*, pages 1689–1694. IEEE, 2016.

[28] Dario Brescianini and Raffaello D'Andrea. Design, modeling and control of an omni-directional aerial vehicle. In *2016 IEEE international conference on robotics and automation (ICRA)*, pages 3261–3266. IEEE, 2016.

[29] Alejandro Suárez, P Sanchez-Cuevas, M Fernandez, M Perez, Guillermo Heredia, and Anibal Ollero. Lightweight and compliant long reach aerial manipulator for inspection operations. In *2018 IEEE/RSJ International Conference on Intelligent Robots and Systems (IROS)*, pages 6746–6752. IEEE, 2018.

[30] R. Bischoff and T. Guhl. The strategic research agenda for robotics in europe [industrial activities]. *IEEE Robotics Automation Magazine*, 17(1):15–16, March 2010.

[31] ARCAS. Aerial robotics cooperative assembly system (arcas project). `http://arcas-project.eu/project-overview/`, 2015. Accessed: 2020-08-20.

[32] A. Ollero, G. Heredia, A. Franchi, G. Antonelli, K. Kondak, A. Sanfeliu, A. Viguria, J. R. Martinez-de Dios, F. Pierri, J. Cortes, A. Santamaria-Navarro, M. A. Trujillo Soto, R. Balachandran, J. Andrade-Cetto, and A. Rodriguez. The

aeroarms project: Aerial robots with advanced manipulation capabilities for inspection and maintenance. *IEEE Robotics Automation Magazine*, 25(4):12–23, Dec 2018.

[33] AEROBI. Aerial robotic system for in-depth bridge inspection by contact (aerobi project). `http://www.aerobi.eu/`, 2018. Accessed: 2020-08-20.

[34] HYFLIERS. Hybrid flying-rolling with-snake-arm robot for contact inspection (hyfliers project). `https://www.oulu.fi/hyfliers/`, 2018. Accessed: 2020-08-20.

[35] RESIST. Resilient transport infrastructure to extreme events (resist project). `http://www.resistproject.eu/`, 2018. Accessed: 2020-08-20.

[36] AERIAL-CORE. Aerial cognitive integrated multi-task robotic system with extended operation range and safety (aerial-core project). `https://aerial-core.eu/`, 2019. Accessed: 2020-08-20.

[37] PILOTING. Pilots for robotic inspection and maintenance grounded on advanced intelligent platforms and prototype applications (piloting project). `https://piloting-project.eu/`, 2020. Accessed: 2020-08-20.

[38] TOTAL. Total global homepage. `https://www.total.com/en`, 2020. Accessed: 2020-08-20.

[39] CHEVRON. Chevron global homepage. `https://www.chevron.com/`, 2020. Accessed: 2020-08-20.

[40] EGNATIA. Egnatia odos s.a. global homepage. `http://www.egnatia.gr/page/default.asp?la=2/`, 2020. Accessed: 2020-08-20.

[41] FERROVIAL. Ferrovial global homepage. `http://www.ferrovial.com/`, 2020. Accessed: 2020-08-20.

[42] ENEL. Enel global homepage. `http://www.enel.com`, 2020. Accessed: 2020-08-20.

[43] Wayne Johnson. *Helicopter theory*. Courier Corporation, 2012.

[44] Gordon J Leishman. *Principles of helicopter aerodynamics with CD extra*. Cambridge university press, 2006.

[45] Richard Von Mises. *Theory of flight*. Courier Corporation, 1959.

[46] Carlos Rodríguez de Cos and José Ángel Acosta. Explicit aerodynamic model characterization of a multirotor unmanned aerial vehicle in quasi-steady flight. *Journal of Computational and Nonlinear Dynamics*, 15(8), 2020.

[47] MARCO C DeSimone, SERENA Russo, and ALESSANDRO Ruggiero. Influence of aerodynamics on quadrotor dynamics. *Recent Researches in Mechanical and Transportation Systems Influence*, pages 111–118, 2015.

[48] Daniele Sartori and Wenxian Yu. Experimental characterization of a propulsion system for multi-rotor uavs. *Journal of Intelligent & Robotic Systems*, 96(3-4):529–540, 2019.

[49] IC Cheeseman and WE Bennett. The effect of ground on a helicopter rotor in forward flight. 1955.

[50] Evan A Fradenburgh. The helicopter and the ground effect machine. *Journal of the American Helicopter Society*, 5(4):24–33, 1960.

[51] James S Hayden. The effect of the ground on helicopter hovering power required. In *Proc. AHS 32nd Annual Forum*, 1976.

[52] HC Curtiss, M Sun, WF Putman, and EJ Hanker. Rotor aerodynamics in ground effect at low advance ratios. *Journal of the American Helicopter Society*, 29(1):48–55, 1984.

[53] Timothy E Lee, J Gordon Leishman, and Manikandan Ramasamy. Fluid dynamics of interacting blade tip vortices with a ground plane. *Journal of the American Helicopter Society*, 55(2):22005–22005, 2010.

[54] Philip E Tanner, Austin D Overmeyer, Luther N Jenkins, Chung-Sheng Yao, and Scott M Bartram. Experimental investigation of rotorcraft outwash in ground effect. 2015.

[55] Kenichiro Nonaka and Hirokazu Sugizaki. Integral sliding mode altitude control for a small model helicopter with ground effect compensation. In *Proceedings of the 2011 american control conference*, pages 202–207. IEEE, 2011.

[56] Moses Bangura, Robert Mahony, et al. Nonlinear dynamic modeling for high performance control of a quadrotor. In *Australasian Conference on Robotics and Automation*, 2012.

[57] Dinuka Abeywardena, Zhan Wang, Gamini Dissanayake, Steven L Waslander, and Sarath Kodagoda. Model-aided state estimation for quadrotor micro air vehicles amidst wind disturbances. In *2014 IEEE/RSJ International Conference on Intelligent Robots and Systems*, pages 4813–4818. IEEE, 2014.

[58] Moses Bangura, Hyon Lim, H Jin Kim, and Robert Mahony. Aerodynamic power control for multirotor aerial vehicles. In *2014 IEEE International Conference on Robotics and Automation (ICRA)*, pages 529–536. IEEE, 2014.

[59] Christopher D McKinnon and Angela P Schoellig. Unscented external force and torque estimation for quadrotors. In *2016 IEEE/RSJ International Conference on Intelligent Robots and Systems (IROS)*, pages 5651–5657. IEEE, 2016.

[60] Teodor Tomić and Sami Haddadin. A unified framework for external wrench estimation, interaction control and collision reflexes for flying robots. In *2014 IEEE/RSJ International Conference on Intelligent Robots and Systems*, pages 4197–4204. IEEE, 2014.

[61] Fabio Ruggiero, Jonathan Cacace, Hamid Sadeghian, and Vincenzo Lippiello. Impedance control of vtol uavs with a momentum-based external generalized forces estimator. In *2014 IEEE International Conference on Robotics and Automation (ICRA)*, pages 2093–2099. IEEE, 2014.

[62] Burak Yüksel, Cristian Secchi, Heinrich H Bülthoff, and Antonio Franchi. A nonlinear force observer for quadrotors and application to physical interactive tasks. In *2014 IEEE/ASME International Conference on Advanced Intelligent Mechatronics*, pages 433–440. IEEE, 2014.

[63] Teodor Tomić and Sami Haddadin. Simultaneous estimation of aerodynamic and contact forces in flying robots: Applications to metric wind estimation and collision detection. In *2015 IEEE International Conference on Robotics and Automation (ICRA)*, pages 5290–5296. IEEE, 2015.

[64] Nicolas Guenard, Tarek Hamel, and Laurent Eck. Control laws for the tele operation of an unmanned aerial vehicle known as an x4-flyer. In *2006 IEEE/RSJ International Conference on Intelligent Robots and Systems*, pages 3249–3254. IEEE, 2006.

[65] Hadi Nobahari and AR Sharifi. Continuous ant colony filter applied to online estimation and compensation of ground effect in automatic landing of quadrotor. *Engineering Applications of Artificial Intelligence*, 32:100–111, 2014.

[66] Li Danjun, Zhou Yan, Shi Zongying, and Lu Geng. Autonomous landing of quadrotor based on ground effect modelling. In *2015 34th Chinese Control Conference (CCC)*, pages 5647–5652. IEEE, 2015.

[67] John Bartholomew, Andrew Calway, and Walterio Mayol-Cuevas. Learning to predict obstacle aerodynamics from depth images for micro air vehicles. In *2014 IEEE International Conference on Robotics and Automation (ICRA)*, pages 4967–4973. IEEE, 2014.

[68] Chin Gian Hooi, Francis D Lagor, and Derek A Paley. Flow sensing for height estimation and control of a rotor in ground effect: modeling and experimental results. In *Proceedings of the AHS 71st Annual Forum*, 2015.

[69] Caitlin Powers, Daniel Mellinger, Aleksandr Kushleyev, Bruce Kothmann, and Vijay Kumar. Influence of aerodynamics and proximity effects in quadrotor flight. In *Experimental robotics*, pages 289–302. Springer, 2013.

[70] I Sharf, M Nahon, A Harmat, W Khan, M Michini, N Speal, M Trentini, T Tsadok, and T Wang. Ground effect experiments and model validation with draganflyer x8 rotorcraft. In *2014 International Conference on Unmanned Aircraft Systems (ICUAS)*, pages 1158–1166. IEEE, 2014.

[71] AE Jimenez-Cano, J Braga, Guillermo Heredia, and Aníbal Ollero. Aerial manipulator for structure inspection by contact from the underside. In *2015 IEEE/RSJ international conference on intelligent robots and systems (IROS)*, pages 1879–1884. IEEE, 2015.

[72] AE Jimenez-Cano, G Heredia, and A Ollero. Aerial manipulator with a compliant arm for bridge inspection. In *2017 International Conference on Unmanned Aircraft Systems (ICUAS)*, pages 1217–1222. IEEE, 2017.

[73] AEROARMS. Aerial robotic system integrating multiple arms and advanced manipulation capabilities for inspection and maintenance (aeroarms project). `http://aeroarms-project.eu/`, 2018. Accessed: 2020-08-20.

[74] Daniel A Griffiths. A study of dual-rotor interference and ground effect using a free-vortex wake model. In *American Helicopter Society 58th Annual Forum, Montreal, Canada, June 11-13, 2002*, 2002.

[75] Davide Del Cont Bernard, Fabio Riccardi, MATTIA GIURATO, and Marco Lovera. A dynamic analysis of ground effect for a quadrotor platform. In *20th World Congress of the International Federation of Automatic Control (IFAC 2017)*, volume 50, pages 10311–10316, 2017.

[76] Pedro J Sanchez-Cuevas, Guillermo Heredia, and Anibal Ollero. Experimental approach to the aerodynamic effects produced in multirotors flying close to obstacles. In *Iberian Robotics Conference*, pages 742–752. Springer, 2017.

[77] Pedro J Sanchez-Cuevas, Pablo Ramon-Soria, Begoña Arrue, Anibal Ollero, and Guillermo Heredia. Robotic system for inspection by contact of bridge beams using uavs. *Sensors*, 19(2):305, 2019.

[78] PJ Sanchez-Cuevas, G Heredia, and A Ollero. Multirotor uas for bridge inspection by contact using the ceiling effect. In *2017 International Conference on Unmanned Aircraft Systems (ICUAS)*, pages 767–774. IEEE, 2017.

[79] Pedro Sanchez-Cuevas, Guillermo Heredia, and Anibal Ollero. Characterization of the aerodynamic ground effect and its influence in multirotor control. *International Journal of Aerospace Engineering*, 2017, 2017.

[80] Antonio E Jimenez-Cano, Pedro J Sanchez-Cuevas, Pedro Grau, Anibal Ollero, and Guillermo Heredia. Contact-based bridge inspection multirotors: Design, modeling, and control considering the ceiling effect. *IEEE Robotics and Automation Letters*, 4(4):3561–3568, 2019.

[81] Pedro Sanchez-Cuevas, Guillermo Heredia, and Anibal Ollero. Multirotor aerodynamic effects in aerial manipulation. In *Aerial Robotic Manipulation*, pages 67–82. Springer, 2019.

[82] PJ Sanchez-Cuevas, Victor Martín, Guillermo Heredia, and Aníbal Ollero. Aerodynamic effects in multirotors flying close to obstacles: Modelling and mapping. In *Iberian Robotics conference*, pages 63–74. Springer, 2019.

[83] Guillermo Heredia and Pedro Sanchez-Cuevas. *Control of Aerial Robotic Manipulators*, pages 1–10. Springer Berlin Heidelberg, Berlin, Heidelberg, 2020.

[84] Alvaro Caballero, Pedro J Sanchez-Cuevas, Manuel Bejar, Guillermo Heredia, Miguel A Trujillo, and Anibal Ollero. An aerodynamic extension for motion planning with dynamics awareness in aerial long-reach manipulators. *International Journal of Aerospace Engineering*, 2020, 2020.

[85] Agustin Ramos, Pedro Jesus Sanchez-Cuevas, Guillermo Heredia, and Anibal Ollero. Spherical fully covered uav with autonomous indoor localization. In *Iberian Robotics conference*, pages 355–367. Springer, 2019.

[86] Manuel Fernandez, Pedro Jesus Sanchez-Cuevas, Guillermo Heredia, and Anibal Ollero. Securing uav communications using ros with custom ecies-based method. In *RED-UAS*, 2019.

[87] Hideyuki Tsukagoshi, Masahiro Watanabe, Takahiro Hamada, Dameitry Ashlih, and Ryuma Iizuka. Aerial manipulator with perching and door-opening capability. In *2015 IEEE International Conference on Robotics and Automation (ICRA)*, pages 4663–4668. IEEE, 2015.

[88] Robert Mahony, Vijay Kumar, and Peter Corke. Multirotor aerial vehicles: Modeling, estimation, and control of quadrotor. *IEEE Robotics and Automation magazine*, 19(3):20–32, 2012.

[89] Vincenzo Lippiello and Fabio Ruggiero. Cartesian impedance control of a uav with a robotic arm. *IFAC Proceedings Volumes*, 45(22):704–709, 2012.

[90] J Zbrozek. Ground effect on the lifting rotor. *ARC RM 2347*, pages 1–8, 1950.

[91] Pedro Castillo Garcia, Rogelio Lozano, and Alejandro Enrique Dzul. *Modelling and control of mini-flying machines*. Springer Science & Business Media, 2006.

[92] Jin-Woo Seo, Byoung-Eon Lee, Beom-Soo Kang, Se-Jong Oh, and Kwan-Jung Yee. Experimental study on the small-scale rotor hover performance in partial ground conditions. *Journal of the Korean Society for Aeronautical & Space Sciences*, 38(1):12–21, 2010.

[93] Steven Bellens, Joris De Schutter, and Herman Bruyninckx. A hybrid pose/wrench control framework for quadrotor helicopters. In *2012 IEEE International Conference on Robotics and Automation*, pages 2269–2274. IEEE, 2012.

[94] Brodie Chan, Hong Guan, Jun Jo, and Michael Blumenstein. Towards uav-based bridge inspection systems: A review and an application perspective. *Structural Monitoring and Maintenance*, 2(3):283–300, 2015.

[95] Junwon Seo, Luis Duque, and Jim Wacker. Drone-enabled bridge inspection methodology and application. *Automation in Construction*, 94:112–126, 2018.

[96] Paul EI Pounds, Daniel R Bersak, and Aaron M Dollar. Stability of small-scale uav helicopters and quadrotors with added payload mass under pid control. *Autonomous Robots*, 33(1-2):129–142, 2012.

[97] Daniel Mellinger, Quentin Lindsey, Michael Shomin, and Vijay Kumar. Design, modeling, estimation and control for aerial grasping and manipulation. In *2011 IEEE/RSJ International Conference on Intelligent Robots and Systems*, pages 2668–2673. IEEE, 2011.

[98] Matko Orsag, Christopher Korpela, and Paul Oh. Modeling and control of mm-uav: Mobile manipulating unmanned aerial vehicle. *Journal of Intelligent & Robotic Systems*, 69(1-4):227–240, 2013.

[99] Teodor Tomić, Christian Ott, and Sami Haddadin. External wrench estimation, collision detection, and reflex reaction for flying robots. *IEEE Transactions on Robotics*, 33(6):1467–1482, 2017.

[100] Fabio Ruggiero, Jonathan Cacace, Hamid Sadeghian, and Vincenzo Lippiello. Passivity-based control of vtol uavs with a momentum-based estimator of external wrench and unmodeled dynamics. *Robotics and Autonomous Systems*, 72:139–151, 2015.

[101] Vernon J Rossow. Effect of ground and/or ceiling planes on thrust of rotors in hover. 1985.

[102] Samir Bouabdallah and Roland Siegwart. Full control of a quadrotor. In *2007 IEEE/RSJ International Conference on Intelligent Robots and Systems*, pages 153–158. Ieee, 2007.

[103] Miguel Ángel Trujillo, José Ramiro Martínez-de Dios, Carlos Martín, Antidio Viguria, and Aníbal Ollero. Novel aerial manipulator for accurate and robust industrial ndt contact inspection: A new tool for the oil and gas inspection industry. *Sensors*, 19(6):1305, 2019.

[104] MW Spong. Modeling and control of elastic joint robots. *Mathematical and Computer Modelling*, 12(7):912, 1989.

[105] Bruno Siciliano and Oussama Khatib. *Springer handbook of robotics*. Springer, 2016.

[106] Roy Featherstone. *Rigid body dynamics algorithms*. Springer, 2014.

[107] Ricardo Ragel, Iván Maza, Fernando Caballero, and Aníbal Ollero. Comparison of motion planning techniques for a multi-rotor UAS equipped with a multi-joint manipulator arm. In *Research, Education and Development of Unmanned Aerial Systems (RED-UAS), 2015 Workshop on*, pages 133–141. IEEE, 2015.

[108] A. Caballero, M. Bejar, and A. Ollero. On the use of velocity adaptation to outperform the motion planning with dynamics awareness in aerial long-reach manipulators with two arms. In *2018 International Conference on Unmanned Aircraft Systems (ICUAS)*, pages 1125–1133. IEEE, 2018.

[109] Alvaro Caballero, Manuel Bejar, Angel Rodriguez-Castaño, and Anibal Ollero. Motion planning with dynamics awareness for long reach manipulation in aerial robotic systems with two arms. *International Journal of Advanced Robotic Systems*, 15(3), 2018.

[110] A. Caballero, M. Bejar, A. Rodriguez-Castaño, and A. Ollero. Motion planning for long reach manipulation in aerial robotic systems with two arms. In *2017 European Conference on Mobile Robots (ECMR)*, pages 1–7, 2017.

[111] Konstantin Kondak, Markus Bernard, Nicolas Meyer, and Gunter Hommel. Autonomously flying VTOL-robots: Modeling and control. In *Robotics and Automation (ICRA), 2007 IEEE International Conference on*, pages 736–741. IEEE, 2007.